

3-9-2023

Surface Roughness Prediction in End Milling Processes Considering the Vibration of the Cutting Tool

Yubin Lee
Portland State University

Follow this and additional works at: https://pdxscholar.library.pdx.edu/open_access_etds



Part of the [Mechanical Engineering Commons](#)

Let us know how access to this document benefits you.

Recommended Citation

Lee, Yubin, "Surface Roughness Prediction in End Milling Processes Considering the Vibration of the Cutting Tool" (2023). *Dissertations and Theses*. Paper 6313.
<https://doi.org/10.15760/etd.8167>

This Dissertation is brought to you for free and open access. It has been accepted for inclusion in Dissertations and Theses by an authorized administrator of PDXScholar. Please contact us if we can make this document more accessible: pdxscholar@pdx.edu.

Surface Roughness Prediction in End Milling Processes Considering the Vibration of
the Cutting Tool

by

Yubin Lee

A dissertation submitted in partial fulfillment of the
requirements for the degree of

Doctor of Philosophy
in
Mechanical Engineering

Thesis Committee:
Chien Wern, Chair
Sung Yi
David Turcic
Lemmy Meekisho

Portland State University
2023

Abstract

Purpose

Machining is a manufacturing process for making the desired design with dimensional tolerance and surface roughness. Despite the development of engineering technology, predicting machined surface roughness is still challenging since there are various factors, such as material properties, tool material properties, the rigidity of the machine tool, and the use of coolant. In particular, tool vibration is the most critical factor since it makes it challenging to obtain the desired quality of the machined product by unintentionally making a tool move. Therefore, surface finish was explored in this study, considering cutting tool vibration under various axial depth-of-cuts and feed speeds.

Design/Methodology/Approach

This study investigated the relationship between milling tool vibrations and machining parameters by computing milling simulation through the Newmark integration method. Then, several surface roughness prediction models, considering tool vibrations, were compared.

Findings

In a correlation of milling parameters, cutting forces, and tool vibration, an increase in axial depth-of-cut and/or feed speed led to an increase in the magnitude of tool vibration. Also, an increase in axial depth-of-cut/or feed speed resulted in a high surface finish value.

Practical Implication

This study will help industries predict milling cutting forces, vibrations, cutter trajectory, and surface roughness. Also, when developing a new cutting tool, this study can be used to understand the relationship between cutting tool properties and metal cutting parameters.

Acknowledgements

I would like to express my sincere appreciation to my advisor, Dr. Chien Wern, a considerate and caring professor. His courteous support and guidance have motivated me throughout my graduate studies at Portland State University. His vast knowledge helped me during my research and throughout my entire journey. Throughout my journey, I was able to improve my professional experience since he provided opportunities to gain experience in various manufacturing fields through projects. It would not have been possible without his support and encouragement. Once again, I deeply appreciate his support.

I would also like to extend my deepest appreciation to Dr. Sung Yi, the department chair, and co-supervisor of my research, for continuously inspiring me and guiding my research. I could not have imagined that my entire journey would have been possible without his support and encouragement.

I would like to express my appreciation to Dr. Cheolhee Kim. His courteous support and guidance helped me in preparing for the milling experiment and building a relationship with a vendor.

I would like to thank the members of my dissertation committee, Dr. David Turcic and Dr. Lemmy Meekisho, for their valuable discussion and insightful comments.

I would like to thank my friends who supported me in moving forward. Lastly, and most importantly, I would like to thank my parents for their dedication, beliefs, sac-

rifice, and love. There are no words to express how thankful I am for them. Without their support and encouragement, I cannot imagine how this study could have been completed successfully.

Table of Contents

Abstract	i
Acknowledgements	iii
List of Tables	vii
List of Figures	ix
Chapter 1 Introduction	1
1.1 Objectives	1
1.2 Literature review	4
Chapter 2 Background Theory	18
2.1 Cutting force in milling process	18
2.2 Equation of mechanical motion in milling process	25
2.3 Modal analysis	27
2.4 Newmark method	29
2.5 Surface roughness prediction	39
Chapter 3 Experimental setup	49

Chapter 4 Results and Discussion	56
4.1 Modal analysis with finite element method	56
4.2 Milling process simulation with Newmark method	64
4.3 Surface roughness results from milling experiments	151
Chapter 5 Conclusions	165
Bibliography	167
Appendix A Chatter tendency according to workpiece materials	177
Appendix B CNC milling operation G-code	184
Appendix C Machined surface roughness	187
Appendix D Tooth passing frequency	198

List of Tables

Table 1.1	Summary of surface finish prediction reference for the milling process [Wang, 2019].	14
Table 2.1	Newmark parameters ([Newmark, 1959])	31
Table 2.2	Example case presented in [Inspurger, 2016]	33
Table 2.3	Summary of Figure 2.4	37
Table 3.1	Specifications of the tool assembly.	51
Table 3.2	Specifications of the milling insert.	52
Table 3.3	Milling parameters for experiments	53
Table 4.1	Material properties for cutting tool presented by [Liu and Liu, 2013]	57
Table 4.2	Modal mass results from the finite element analysis	57
Table 4.3	Natural frequency and participation factor results obtained by modal analysis	58
Table 4.4	Computed mechanical properties of cutting tool	63
Table 4.5	Simulation parameters used in this study are taken from Wang et al. [[Wang, 2019], [Omar, 2007], [Schmitz, 2019],[Tsai et al., 2016]], and Table 4.4.	65

Table 4.6	Simulated feed per tooth that was used in this study [Wang, 2019].	67
Table 4.7	Experiment surface roughness results at axial depth-of-cut of 0.15 mm.	151
Table 4.8	Experiment surface roughness results at axial depth-of-cut of 1 mm.	152
Table 4.9	Surface roughness experiment results at axial depth-of-cut of 5 mm.	153
Table 4.10	Average surface roughness estimation by arithmetic surface roughness Eq (1.11).	154
Table 4.11	Surface roughness estimation by mathematical surface roughness Eq (2.54).	156
Table 4.12	Surface roughness estimation by geometrical surface roughness Eq (2.49).	159
Table 4.13	Surface roughness prediction comparison of geometrical surface roughness with the experimental result.	161
Table 4.14	Average surface roughness comparison of geometrical surface roughness with the experimental result.	163

List of Figures

Figure 1.1 Diagram with the parameters that affect surface roughness [Benardos, 2003].	3
Figure 1.2 Schematic of roughness and waviness in a surface [Raja et al., 2002].	4
Figure 1.3 Schematic of arithmetic surface roughness [Gu et al., 2001].	5
Figure 1.4 Example stability lobe diagram [Naterwalla, 2020].	10
Figure 2.1 Schematic of tangential and normal cutting forces acting on the cutting tool [Schmitz, 2019].	18
Figure 2.2 Schematic of cutting tool angle [Schmitz, 2019].	19
Figure 2.3 Schematic mechanical model of a cutting tool [Schmitz, 2019]. . .	25
Figure 2.4 Newmark integration time step of 3.13×10^{-5} (sec).	34
Figure 2.5 Newmark integration time step of 1.88×10^{-5} (sec).	35
Figure 2.6 Newmark integration time step of 9.4×10^{-6} (sec).	35
Figure 2.7 Newmark integration time step of 3.8×10^{-6} (sec).	36
Figure 2.8 Newmark integration time step of 1.3×10^{-6} (sec).	36
Figure 2.9 Newmark integration time step of 9.4×10^{-7} (sec).	37
Figure 2.10 Schematic of surface roughness after milling with square insert [Munoz-Escalona and Maropoulos, 2015].	39

Figure 2.11 Schematic of surface roughness considering tool vibrations [Munoz-Escalona and Maropoulos, 2015].	43
Figure 2.12 A mathematical surface profile consisting of elliptical arcs [Qu, 2003].	46
Figure 2.13 Effect of vibration on feed per tooth.	48
Figure 3.1 CNC milling machine.	49
Figure 3.2 Dimensions of the workpiece (mm).	50
Figure 3.3 DAEGUTECH, indexable milling cutter, SCRM75SP-6100-32R-12B.	50
Figure 3.4 Dimensions and critical parameters of the indexable tool assembly.	51
Figure 3.5 DAEGUTECH, milling insert, SPKT-1204-EDTR-HP.	52
Figure 3.6 Milling experiment schemetic.	52
Figure 4.1 Meshing of the milling tool assembly.	57
Figure 4.2 2nd mode shape of the cutting tool.	61
Figure 4.3 1st mode shape of the cutting tool.	61
Figure 4.4 11th mode shape of the cutting tool.	62
Figure 4.5 Cutting force in the x -direction at feed: 0.0254 (mm/tooth) and axial depth-of-cut: 0.15 (mm).	68
Figure 4.6 Cutting force in the x -direction at feed: 0.127 (mm/tooth) and axial depth-of-cut: 0.15 (mm).	69
Figure 4.7 Cutting force in the x -direction at feed: 0.203 (mm/tooth) and axial depth-of-cut: 0.15 (mm).	69

Figure 4.8	Cutting force in the x -direction at feed: 0.305 (mm/tooth) and axial depth-of-cut: 0.15 (mm).	70
Figure 4.9	Cutting force in the x -direction at feed: 0.406 (mm/tooth) and axial depth-of-cut: 0.15 (mm).	70
Figure 4.10	Cutting force in the x -direction at feed: 0.508 (mm/tooth) and axial depth-of-cut: 0.15 (mm).	71
Figure 4.11	Cutting force in the x -direction at feed: 0.559 (mm/tooth) and axial depth-of-cut: 0.15 (mm).	71
Figure 4.12	Cutting force in the x -direction at feed: 0.635 (mm/tooth) and axial depth-of-cut: 0.15 (mm).	72
Figure 4.13	Cutting force in the y -direction at feed: 0.0254 (mm/tooth) and axial depth-of-cut: 0.15 (mm).	72
Figure 4.14	Cutting force in the y -direction at feed: 0.127 (mm/tooth) and axial depth-of-cut: 0.15 (mm).	73
Figure 4.15	Cutting force in the y -direction at feed: 0.203 (mm/tooth) and axial depth-of-cut: 0.15 (mm).	73
Figure 4.16	Cutting force in the y -direction at feed: 0.305 (mm/tooth) and axial depth-of-cut: 0.15 (mm).	74
Figure 4.17	Cutting force in the y -direction at feed: 0.406 (mm/tooth) and axial depth-of-cut: 0.15 (mm).	74

Figure 4.18 Cutting force in the y -direction at feed: 0.508 (mm/tooth) and axial depth-of-cut: 0.15 (mm).	75
Figure 4.19 Cutting force in the y -direction at feed: 0.559 (mm/tooth) and axial depth-of-cut: 0.15 (mm).	75
Figure 4.20 Cutting force in the y -direction at feed: 0.635 (mm/tooth) and axial depth-of-cut: 0.15 (mm).	76
Figure 4.21 Cutting force in the z -direction at feed: 0.0254 (mm/tooth) and axial depth-of-cut: 0.15 (mm).	76
Figure 4.22 Cutting force in the z -direction at feed: 0.127 (mm/tooth) and axial depth-of-cut: 0.15 (mm).	77
Figure 4.23 Cutting force in the z -direction at feed: 0.203 (mm/tooth) and axial depth-of-cut: 0.15 (mm).	77
Figure 4.24 Cutting force in the z -direction at feed: 0.305 (mm/tooth) and axial depth-of-cut: 0.15 (mm).	78
Figure 4.25 Cutting force in the z -direction at feed: 0.406 (mm/tooth) and axial depth-of-cut: 0.15 (mm).	78
Figure 4.26 Cutting force in the z -direction at feed: 0.508 (mm/tooth) and axial depth-of-cut: 0.15 (mm).	79
Figure 4.27 Cutting force in the z -direction at feed: 0.559 (mm/tooth) and axial depth-of-cut: 0.15 (mm).	79

Figure 4.28 Cutting force in the z -direction at feed: 0.635 (mm/tooth) and axial depth-of-cut: 0.15 (mm).	80
Figure 4.29 Cutting force in the x -direction at feed: 0.0254 (mm/tooth) and axial depth-of-cut: 1 (mm).	81
Figure 4.30 Cutting force in the x -direction at feed: 0.127 (mm/tooth) and axial depth-of-cut: 1 (mm).	81
Figure 4.31 Cutting force in the x -direction at feed: 0.203 (mm/tooth) and axial depth-of-cut: 1 (mm).	82
Figure 4.32 Cutting force in the x -direction at feed: 0.305 (mm/tooth) and axial depth-of-cut: 1 (mm).	82
Figure 4.33 Cutting force in the x -direction at feed: 0.406 (mm/tooth) and axial depth-of-cut: 1 (mm).	83
Figure 4.34 Cutting force in the x -direction at feed: 0.508 (mm/tooth) and axial depth-of-cut: 1 (mm).	83
Figure 4.35 Cutting force in the x -direction at feed: 0.559 (mm/tooth) and axial depth-of-cut: 1 (mm).	84
Figure 4.36 Cutting force in the x -direction at feed: 0.635 (mm/tooth) and axial depth-of-cut: 1 (mm).	84
Figure 4.37 Cutting force in the y -direction at feed: 0.0254 (mm/tooth) and axial depth-of-cut: 1 (mm).	85

Figure 4.38 Cutting force in the y -direction at feed: 0.127 (mm/tooth) and axial depth-of-cut: 1 (mm).	85
Figure 4.39 Cutting force in the y -direction at feed: 0.203 (mm/tooth) and axial depth-of-cut: 1 (mm).	86
Figure 4.40 Cutting force in the y -direction at feed: 0.305 (mm/tooth) and axial depth-of-cut: 1 (mm).	86
Figure 4.41 Cutting force in the y -direction at feed: 0.406 (mm/tooth) and axial depth-of-cut: 1 (mm).	87
Figure 4.42 Cutting force in the y -direction at feed: 0.508 (mm/tooth) and axial depth-of-cut: 1 (mm).	87
Figure 4.43 Cutting force in the y -direction at feed: 0.559 (mm/tooth) and axial depth-of-cut: 1 (mm).	88
Figure 4.44 Cutting force in the y -direction at feed: 0.635 (mm/tooth) and axial depth-of-cut: 1 (mm).	88
Figure 4.45 Cutting force in the z -direction at feed: 0.0254 (mm/tooth) and axial depth-of-cut: 1 (mm).	89
Figure 4.46 Cutting force in the z -direction at feed: 0.127 (mm/tooth) and axial depth-of-cut: 1 (mm).	89
Figure 4.47 Cutting force in the z -direction at feed: 0.203 (mm/tooth) and axial depth-of-cut: 1 (mm).	90

Figure 4.48 Cutting force in the z -direction at feed: 0.305 (mm/tooth) and axial depth-of-cut: 1 (mm).	90
Figure 4.49 Cutting force in the z -direction at feed: 0.406 (mm/tooth) and axial depth-of-cut: 1 (mm).	91
Figure 4.50 Cutting force in the z -direction at feed: 0.508 (mm/tooth) and axial depth-of-cut: 1 (mm).	91
Figure 4.51 Cutting force in the z -direction at feed: 0.559 (mm/tooth) and axial depth-of-cut: 1 (mm).	92
Figure 4.52 Cutting force in the z -direction at feed: 0.635 (mm/tooth) and axial depth-of-cut: 1 (mm).	92
Figure 4.53 Cutting force in the x -direction at feed: 0.0254 (mm/tooth) and axial depth-of-cut: 5 (mm).	94
Figure 4.54 Cutting force in the x -direction at feed: 0.127 (mm/tooth) and axial depth-of-cut: 5 (mm).	95
Figure 4.55 Cutting force in the x -direction at feed: 0.203 (mm/tooth) and axial depth-of-cut: 5 (mm).	95
Figure 4.56 Cutting force in the x -direction at feed: 0.305 (mm/tooth) and axial depth-of-cut: 5 (mm).	96
Figure 4.57 Cutting force in the x -direction at feed: 0.406 (mm/tooth) and axial depth-of-cut: 5 (mm).	96

Figure 4.58 Cutting force in the x -direction at feed: 0.508 (mm/tooth) and axial depth-of-cut: 5 (mm).	97
Figure 4.59 Cutting force in the x -direction at feed: 0.559 (mm/tooth) and axial depth-of-cut: 5 (mm).	97
Figure 4.60 Cutting force in the x -direction at feed: 0.635 (mm/tooth) and axial depth-of-cut: 5 (mm).	98
Figure 4.61 Cutting force in the y -direction at feed: 0.0254 (mm/tooth) and axial depth-of-cut: 5 (mm).	98
Figure 4.62 Cutting force in the y -direction at feed: 0.127 (mm/tooth) and axial depth-of-cut: 5 (mm).	99
Figure 4.63 Cutting force in the y -direction at feed: 0.203 (mm/tooth) and axial depth-of-cut: 5 (mm).	99
Figure 4.64 Cutting force in the y -direction at feed: 0.305 (mm/tooth) and axial depth-of-cut: 5 (mm).	100
Figure 4.65 Cutting force in the y -direction at feed: 0.406 (mm/tooth) and axial depth-of-cut: 5 (mm).	100
Figure 4.66 Cutting force in the y -direction at feed: 0.508 (mm/tooth) and axial depth-of-cut: 5 (mm).	101
Figure 4.67 Cutting force in the y -direction at feed: 0.559 (mm/tooth) and axial depth-of-cut: 5 (mm).	101

Figure 4.68 Cutting force in the y -direction at feed: 0.635 (mm/tooth) and axial depth-of-cut: 5 (mm).	102
Figure 4.69 Cutting force in the z -direction at feed: 0.0254 (mm/tooth) and axial depth-of-cut: 5 (mm).	102
Figure 4.70 Cutting force in the z -direction at feed: 0.127 (mm/tooth) and axial depth-of-cut: 5 (mm).	103
Figure 4.71 Cutting force in the z -direction at feed: 0.203 (mm/tooth) and axial depth-of-cut: 5 (mm).	103
Figure 4.72 Cutting force in the z -direction at feed: 0.305 (mm/tooth) and axial depth-of-cut: 5 (mm).	104
Figure 4.73 Cutting force in the z -direction at feed: 0.406 (mm/tooth) and axial depth-of-cut: 5 (mm).	104
Figure 4.74 Cutting force in the z -direction at feed: 0.508 (mm/tooth) and axial depth-of-cut: 5 (mm).	105
Figure 4.75 Cutting force in the z -direction at feed: 0.559 (mm/tooth) and axial depth-of-cut: 5 (mm).	105
Figure 4.76 Cutting force in the z -direction at feed: 0.635 (mm/tooth) and axial depth-of-cut: 5 (mm).	106
Figure 4.77 Computed maximum cutting forces in the y -direction with three axial depth-of-cuts.	107

Figure 4.78 Computed maximum cutting force in the x -direction with three axial depth-of-cuts.	108
Figure 4.79 Computed maximum cutting force in the z -direction with three axial depth-of-cuts.	109
Figure 4.80 Tool displacement in the x -direction at feed: 0.0254 (mm/tooth) and axial depth-of-cut: 0.15 (mm).	110
Figure 4.81 Tool displacement in the x -direction at feed: 0.127 (mm/tooth) and axial depth-of-cut: 0.15 (mm).	111
Figure 4.82 Tool displacement in the x -direction at feed: 0.203 (mm/tooth) and axial depth-of-cut: 0.15 (mm).	111
Figure 4.83 Tool displacement in the x -direction at feed: 0.305 (mm/tooth) and axial depth-of-cut: 0.15 (mm).	112
Figure 4.84 Tool displacement in the x -direction at feed: 0.406 (mm/tooth) and axial depth-of-cut: 0.15 (mm).	112
Figure 4.85 Tool displacement in the x -direction at feed: 0.508 (mm/tooth) and axial depth-of-cut: 0.15 (mm).	113
Figure 4.86 Tool displacement in the x -direction at feed: 0.559 (mm/tooth) and axial depth-of-cut: 0.15 (mm).	113
Figure 4.87 Tool displacement in the x -direction at feed: 0.635 (mm/tooth) and axial depth-of-cut: 0.15 (mm).	114

Figure 4.88 Tool displacement in the y -direction at feed: 0.0254 (mm/tooth) and axial depth-of-cut: 0.15 (mm).	114
Figure 4.89 Tool displacement in the y -direction at feed: 0.127 (mm/tooth) and axial depth-of-cut: 0.15 (mm).	115
Figure 4.90 Tool displacement in the y -direction at feed: 0.203 (mm/tooth) and axial depth-of-cut: 0.15 (mm).	115
Figure 4.91 Tool displacement in the y -direction at feed: 0.305 (mm/tooth) and axial depth-of-cut: 0.15 (mm).	116
Figure 4.92 Tool displacement in the y -direction at feed: 0.406 (mm/tooth) and axial depth-of-cut: 0.15 (mm).	116
Figure 4.93 Tool displacement in the y -direction at feed: 0.508 (mm/tooth) and axial depth-of-cut: 0.15 (mm).	117
Figure 4.94 Tool displacement in the y -direction at feed: 0.559 (mm/tooth) and axial depth-of-cut: 0.15 (mm).	117
Figure 4.95 Tool displacement in the y -direction at feed: 0.635 (mm/tooth) and axial depth-of-cut: 0.15 (mm).	118
Figure 4.96 Tool displacement in the z -direction at feed: 0.0254 (mm/tooth) and axial depth-of-cut: 0.15 (mm).	118
Figure 4.97 Tool displacement in the z -direction at feed: 0.127 (mm/tooth) and axial depth-of-cut: 0.15 (mm).	119

Figure 4.98 Tool displacement in the z -direction at feed: 0.203 (mm/tooth) and axial depth-of-cut: 0.15 (mm).	119
Figure 4.99 Tool displacement in the z -direction at feed: 0.305 (mm/tooth) and axial depth-of-cut: 0.15 (mm).	120
Figure 4.100 Tool displacement in the z -direction at feed: 0.406 (mm/tooth) and axial depth-of-cut: 0.15 (mm).	120
Figure 4.101 Tool displacement in the z -direction at feed: 0.508 (mm/tooth) and axial depth-of-cut: 0.15 (mm).	121
Figure 4.102 Tool displacement in the z -direction at feed: 0.559 (mm/tooth) and axial depth-of-cut: 0.15 (mm).	121
Figure 4.103 Tool displacement in the z -direction at feed: 0.635 (mm/tooth) and axial depth-of-cut: 0.15 (mm).	122
Figure 4.104 Tool displacement in the x -direction at feed: 0.0254 (mm/tooth) and axial depth-of-cut: 1 (mm).	123
Figure 4.105 Tool displacement in the x -direction at feed: 0.127 (mm/tooth) and axial depth-of-cut: 1 (mm).	124
Figure 4.106 Tool displacement in the x -direction at feed: 0.203 (mm/tooth) and axial depth-of-cut: 1 (mm).	124
Figure 4.107 Tool displacement in the x -direction at feed: 0.305 (mm/tooth) and axial depth-of-cut: 1 (mm).	125

Figure 4.108 Tool displacement in the x -direction at feed: 0.406 (mm/tooth) and axial depth-of-cut: 1 (mm).	125
Figure 4.109 Tool displacement in the x -direction at feed: 0.508 (mm/tooth) and axial depth-of-cut: 1 (mm).	126
Figure 4.110 Tool displacement in the x -direction at feed: 0.559 (mm/tooth) and axial depth-of-cut: 1 (mm).	126
Figure 4.111 Tool displacement in the x -direction at feed: 0.635 (mm/tooth) and axial depth-of-cut: 1 (mm).	127
Figure 4.112 Tool displacement in the y -direction at feed: 0.0254 (mm/tooth) and axial depth-of-cut: 1 (mm).	127
Figure 4.113 Tool displacement in the y -direction at feed: 0.127 (mm/tooth) and axial depth-of-cut: 1 (mm).	128
Figure 4.114 Tool displacement in the y -direction at feed: 0.203 (mm/tooth) and axial depth-of-cut: 1 (mm).	128
Figure 4.115 Tool displacement in the y -direction at feed: 0.305 (mm/tooth) and axial depth-of-cut: 1 (mm).	129
Figure 4.116 Tool displacement in the y -direction at feed: 0.406 (mm/tooth) and axial depth-of-cut: 1 (mm).	129
Figure 4.117 Tool displacement in the y -direction at feed: 0.508 (mm/tooth) and axial depth-of-cut: 1 (mm).	130

Figure 4.118	Tool displacement in the y -direction at feed: 0.559 (mm/tooth)	
	and axial depth-of-cut: 1 (mm).	130
Figure 4.119	Tool displacement in the y -direction at feed: 0.635 (mm/tooth)	
	and axial depth-of-cut: 1 (mm).	131
Figure 4.120	Tool displacement in the z -direction at feed: 0.0254 (mm/tooth)	
	and axial depth-of-cut: 1 (mm).	131
Figure 4.121	Tool displacement in the z -direction at feed: 0.127 (mm/tooth)	
	and axial depth-of-cut: 1 (mm).	132
Figure 4.122	Tool displacement in the z -direction at feed: 0.203 (mm/tooth)	
	and axial depth-of-cut: 1 (mm).	132
Figure 4.123	Tool displacement in the z -direction at feed: 0.305 (mm/tooth)	
	and axial depth-of-cut: 1 (mm).	133
Figure 4.124	Tool displacement in the z -direction at feed: 0.406 (mm/tooth)	
	and axial depth-of-cut: 1 (mm).	133
Figure 4.125	Tool displacement in the z -direction at feed: 0.508 (mm/tooth)	
	and axial depth-of-cut: 1 (mm).	134
Figure 4.126	Tool displacement in the z -direction at feed: 0.559 (mm/tooth)	
	and axial depth-of-cut: 1 (mm).	134
Figure 4.127	Tool displacement in the z -direction at feed: 0.635 (mm/tooth)	
	and axial depth-of-cut: 1 (mm).	135

Figure 4.128	Tool displacement in the x -direction at feed: 0.0254 (mm/tooth) and axial depth-of-cut: 5 (mm).	136
Figure 4.129	Tool displacement in the x -direction at feed: 0.127 (mm/tooth) and axial depth-of-cut: 5 (mm).	137
Figure 4.130	Tool displacement in the x -direction at feed: 0.203 (mm/tooth) and axial depth-of-cut: 5 (mm).	137
Figure 4.131	Tool displacement in the x -direction at feed: 0.305 (mm/tooth) and axial depth-of-cut: 5 (mm).	138
Figure 4.132	Tool displacement in the x -direction at feed: 0.406 (mm/tooth) and axial depth-of-cut: 5 (mm).	138
Figure 4.133	Tool displacement in the x -direction at feed: 0.508 (mm/tooth) and axial depth-of-cut: 5 (mm).	139
Figure 4.134	Tool displacement in the x -direction at feed: 0.559 (mm/tooth) and axial depth-of-cut: 5 (mm).	139
Figure 4.135	Tool displacement in the x -direction at feed: 0.635 (mm/tooth) and axial depth-of-cut: 5 (mm).	140
Figure 4.136	Tool displacement in the y -direction at feed: 0.0254 (mm/tooth) and axial depth-of-cut: 5 (mm).	140
Figure 4.137	Tool displacement in the y -direction at feed: 0.127 (mm/tooth) and axial depth-of-cut: 5 (mm).	141

Figure 4.138	Tool displacement in the y -direction at feed: 0.203 (mm/tooth)	
	and axial depth-of-cut: 5 (mm).	141
Figure 4.139	Tool displacement in the y -direction at feed: 0.305 (mm/tooth)	
	and axial depth-of-cut: 5 (mm).	142
Figure 4.140	Tool displacement in the y -direction at feed: 0.406 (mm/tooth)	
	and axial depth-of-cut: 5 (mm).	142
Figure 4.141	Tool displacement in the y -direction at feed: 0.508 (mm/tooth)	
	and axial depth-of-cut: 5 (mm).	143
Figure 4.142	Tool displacement in the y -direction at feed: 0.559 (mm/tooth)	
	and axial depth-of-cut: 5 (mm).	143
Figure 4.143	Tool displacement in the y -direction at feed: 0.635 (mm/tooth)	
	and axial depth-of-cut: 5 (mm).	144
Figure 4.144	Tool displacement in the z -direction at feed: 0.0254 (mm/tooth)	
	and axial depth-of-cut: 5 (mm).	144
Figure 4.145	Tool displacement in the z -direction at feed: 0.127 (mm/tooth)	
	and axial depth-of-cut: 5 (mm).	145
Figure 4.146	Tool displacement in the z -direction at feed: 0.203 (mm/tooth)	
	and axial depth-of-cut: 5 (mm).	145
Figure 4.147	Tool displacement in the z -direction at feed: 0.305 (mm/tooth)	
	and axial depth-of-cut: 5 (mm).	146

Figure 4.148	Tool displacement in the z -direction at feed: 0.406 (mm/tooth) and axial depth-of-cut: 5 (mm).	146
Figure 4.149	Tool displacement in the z -direction at feed: 0.508 (mm/tooth) and axial depth-of-cut: 5 (mm).	147
Figure 4.150	Tool displacement in the z -direction at feed: 0.559 (mm/tooth) and axial depth-of-cut: 5 (mm).	147
Figure 4.151	Tool displacement in the z -direction at feed: 0.635 (mm/tooth) and axial depth-of-cut: 5 (mm).	148
Figure 4.152	Computed maximum tool displacement in the x -direction with three axial depth-of-cuts.	148
Figure 4.153	Computed maximum tool displacement in the y -direction with three axial depth-of-cuts.	149
Figure 4.154	Computed maximum tool displacement in the z -direction with three axial depth-of-cuts.	150

Chapter 1

Introduction

1.1 Objectives

Metal cutting is an indispensable manufacturing process to make the desired geometry with a precise dimension of a product. Among various metal cutting processes, milling is the most universal and complicated machining method to produce flat or contoured surfaces, slots, grooves, recesses, threads, and other configurations. The milling process can be depicted by a rotating cutter and a workpiece that is translating into the cutter. Although the process has more variations in machining preparation, such as workpiece movements and tooling, than any other primary machining method, it is still highly recommended [Altintas, 2012]. The milling process's advantages are that it is capable of producing high stock removal rates and relatively smooth surface finishes and shapes any complex product design through a wide variety of cutting tools [Drozda and Wick]. Therefore, we selected the milling process to explore since it is a versatile and practical machining process.

There are several machinability indicators, such as cutting force, tool life, power

consumption, etc [Drozda and Wick]. Among the various indicators reflecting cutting performance, surface quality is a critical indicator, as it reflects the product's appearance, function, reliability, and the geometrical features of the surface that determine the fatigue life and corrosion life [Kadirgama et al., 2009]. Additionally, a rough surface roughness can result in high levels of surface tensile residual stress, which can lead to mechanical failures such as corrosion and fatigue cracks, as the surface layers are exposed to the highest load and environmental effects [Javidi et al., 2008]. Furthermore, the machined surface finish can indicate workpiece material non-homogeneity, progressive tool wear, and cutting tool chatter, which affect the stability of the milling process [Hayajneh et al., 2007].

In Figure 1.1, Benardos and Vosniakos [Benardos, 2003] defined several factors that affect the surface quality of a workpiece in the milling process. These factors comprise machining parameters, cutting tool properties, workpiece properties, and cutting phenomena. Machining parameters comprises the superposition of a theoretical profile, cooling fluid, step-over, depth-of-cut, insert angle, feed rate, and cutting speed. Cutting tool properties include the tool material, runout errors, nose radius, tool shape, diameter, tool length, and the number of teeth. Cutting phenomena consist of accelerations, chip formation, vibrations, friction in the cutting zone, and variation in cutting force. Lastly, workpiece properties include hardness, toughness, stiffness, and specific cutting energy of the material.

In particular, tool vibration is a critical parameter since that affects the quality of

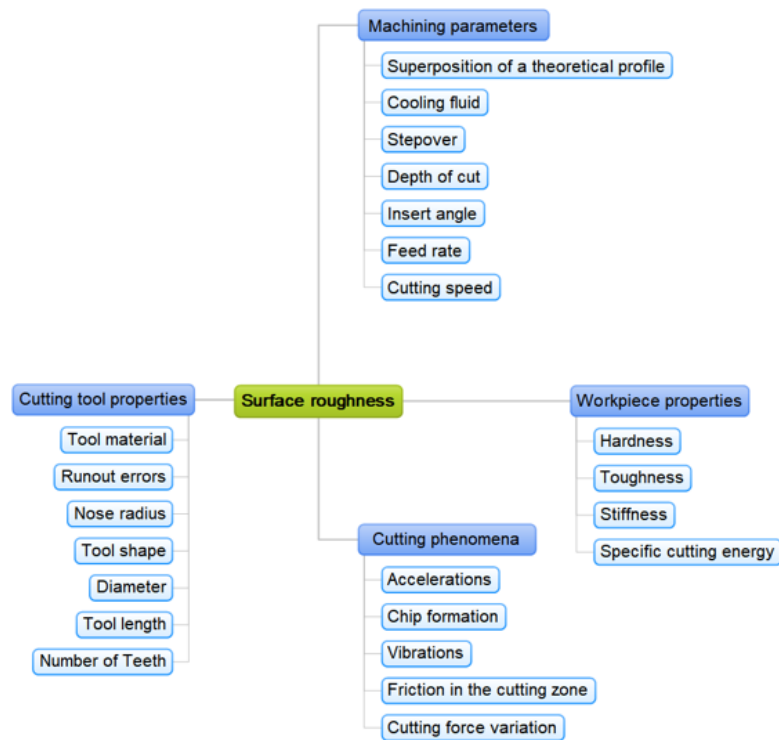


Figure 1.1: Diagram with the parameters that affect surface roughness [Benardos, 2003].

the machined surface and tool life [Bhogal et al., 2015]. Furthermore, tool vibrations are the most challenging factor in making a tool move unpredictably [Ostasevicius, 2019].

This research explored the effect of cutting tool properties, cutting phenomena, workpiece properties, and machining parameters on cutting forces and tool vibrations by performing numerical simulations for the milling process. Then, the geometrical surface roughness method predicted a machined surface finish incorporating a geometrical interpretation of tool nose and milling tool vibrations obtained by numerical simulation.

1.2 Literature review

Arithmetic surface roughness

Since the machined surface is composed of roughness, waviness, lay, flaws, and feed marks, the surface finish is a criterion to determine the general quality of a workpiece surface [Drozda and Wick].

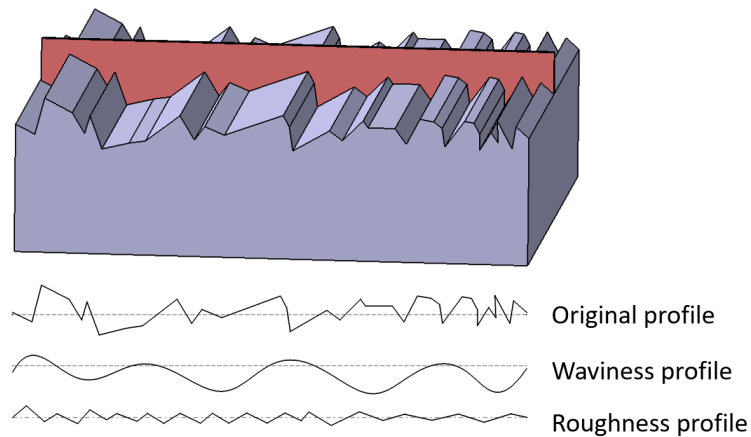


Figure 1.2: Schematic of roughness and waviness in a surface [Raja et al., 2002].

Although the original profile shown in Figure 1.2 contains significant forms such as radius, separating surface profile data into meaningful wavelength regimes is essential to analyze the engineering surface properly. Thus, the high frequency or short wavelength is considered roughness, the medium frequencies as waviness, and the low frequency as form [Raja et al., 2002]. Then, surface topography can be characterized by several amplitude parameters, such as average arithmetic height, root means square roughness, ten-point height, the maximum height of peaks, etc. The arith-

metric surface roughness is considered a typical wavelength band, and it is obtained by the average absolute deviation of the roughness from the mean line over one sampling length [Gadelmawla et al., 2002].

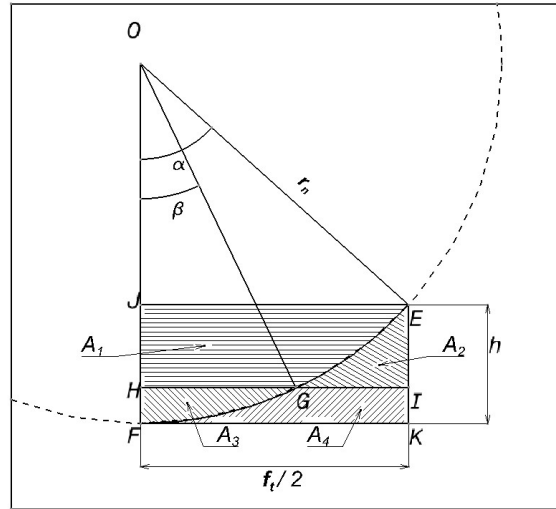


Figure 1.3: Schematic of arithmetic surface roughness [Gu et al., 2001].

Figure 1.3 shows the trailing half of a feed mark generated by the tool nose r_n after one pass is finished in the milling operation. The surface roughness is computed geometrically by separating half of the trailing area into A_1 , A_2 , A_3 , and A_4 . In the figure, points at E and F represent the peak and bottom of the feed mark, and the arithmetic roughness Ra is defined by:

$$Ra = \frac{A_3 + A_4}{f_t/2} \quad (1.1)$$

where f_t is the feed per tooth (mm/tooth). And the area of $JFKE$ is defined by:

$$h \frac{f_t}{2} = A_1 + A_2 + A_3 + A_4 \quad (1.2)$$

where h is the height of a feed mark (mm). In accordance with the assumption of A_2 is equal to A_3 , the area of $JFKE$ can be transformed to:

$$h \frac{f_t}{2} = A_1 + 2A_3 + A_4 = (A_1 + A_3) + (A_3 + A_4) \quad (1.3)$$

The area of $A_1 + A_3$ and $A_3 + A_4$ are defined as:

$$A_1 + A_3 = \frac{1}{2} \alpha r_n^2 - \frac{1}{2} r_n \sin \alpha \cdot r_n \cos \alpha \quad (1.4)$$

$$A_3 + A_4 = \frac{f_t}{2} r_n (1 - \cos \beta) \quad (1.5)$$

When substituting equations (1.4) and (1.5) into equation (1.3), equation (1.3) is transformed to:

$$hf = \alpha r_n^2 - r_n^2 \sin \alpha \cos \alpha + f_t r_n (1 - \cos \beta) \quad (1.6)$$

when

$$\sin \alpha = \frac{f_t}{2r_n} \quad (1.7)$$

$$\cos \alpha = \sqrt{1 - \sin^2 \alpha} = \sqrt{1 - \frac{f_t^2}{4r_n^2}} \quad (1.8)$$

$$h = r_n - r_n \cos \alpha = r_n - r_n \sqrt{1 - \frac{f_t^2}{4r_n^2}} \quad (1.9)$$

Substituting equations (1.7), (1.8), and (1.9) into equation (1.6), β is obtained by:

$$\beta = \arccos \left(\frac{r_n}{f_t} \arcsin \frac{f_t}{2r_n} + \frac{1}{2} \sqrt{1 - \frac{f_t^2}{4r_n^2}} \right) \quad (1.10)$$

Then the arithmetic surface roughness Ra is obtained by substituting β , Equation

(1.10) into:

$$Ra = \frac{2r_n^2}{f_t}(\beta - \sin\beta\cos\beta) \quad (1.11)$$

The schematic of arithmetic surface roughness is widely used in industry to predict the surface finish of the machined product.

Regenerative vibration (chatter)

For the metal cutting process, the chatter phenomenon occurs when the machining frequency is close to the natural frequency of the cutter, spindle, and tool holder assembly. In particular, chatter is considered a critical issue in production quality since it generates a wavy surface on a machined workpiece [Hahn, 1952].

In 1945, Arnold [Hahn, 1952] presented an initial study of tool vibration at a meeting of the Institution of Mechanical Engineers in London by implementing chatter vibration through a lathe tool with an excessive overhang.

Numerous studies have attempted to predict the chatter phenomenon for the milling process. In 1980, Machinability Data center [Handbook, 1980] insisted that the chatter occurs when the cutting severity is equal to or greater than the structural vibration resistance, and they presented a way to predict the chatter by empirical study:

$$QL_c \geq CK_{dm} \quad (1.12)$$

where Q , L_c , C , and K_{dm} represent the workpiece material tendency concerning chatter listed in Table A.1, the length of engaged cutting edge, the factor of cutting speed in the resonant frequency, and minimum dynamic stiffness at the highest resonance peak, respectively. These findings further support the idea of acoustic-based chatter

detection. Naterwalla [Naterwalla, 2020] explained three methods to detect chatter between a tool and a workpiece. The first method uses acoustic sound to detect chatter. The chattering sound is collected using a unidirectional microphone for a cutting process then a level of cutting stability is investigated based on collecting the relative magnitude of sound.

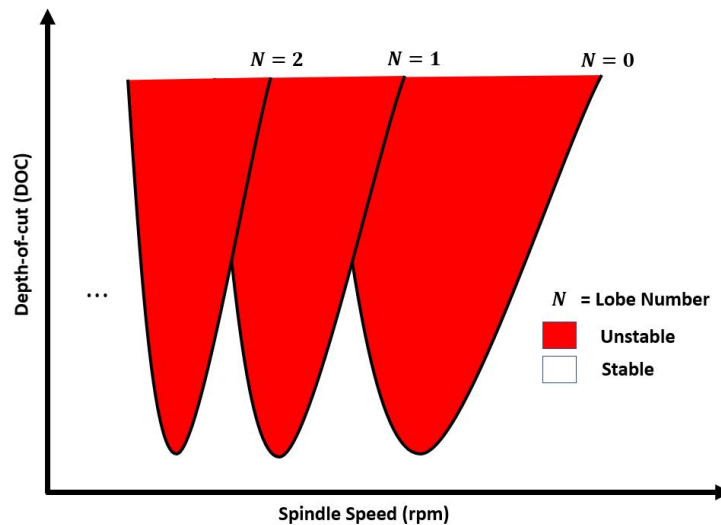


Figure 1.4: Example stability lobe diagram [Naterwalla, 2020].

The second method is the tap test. As shown in Figure 1.4, the stability lobe diagram is defined by the spindle speed (RPM) and depth-of-cut. The regions inside the lobes (red) mean unstable machining operations (chatter), and a sensor-based system is utilized to generate the stability diagram. An accelerometer is positioned at the tip of the cutting edge on a cutting tool assembly to collect vibration data. The last method is a computer-based simulation using finite element analysis. Finite element

analysis characterizes the vibration dynamics of a tool when designing a prototype tool.

Fu et al. [Yang Fu., 2016] proposed the online chatter detection method based on the Hilbert-Huang spectrum (HHS) to recognize chatter in the end milling process. To explore online chatter detection, they conducted dry end milling experiments on the workpiece of Al-F by using uncoated M2Al cutting tools with three teeth. They collected vibration data through accelerometers mounted on the spindle housing and performed experiments with varying the spindle speeds and the axial depth-of-cuts. They insisted that energy distribution based on the Hilbert-Huang transform is more suitable to detect milling chatter. In addition, they insisted that the time-frequency spectrum based on the Hilbert-Huang transform method can detect chatter at the beginning of chatter.

Vibration and surface finish

Several studies have found that tool vibrations caused by cutting force can affect the machined surface finish. These researchers present a variety of approaches to predict/qualify surface roughness.

Wojciechowski et al. [Wojciechowski, 2019] presented a new approach to surface roughness parameters estimation during cylindrical end milling. In this work, they predicted the instantaneous tool displacements by using an analytical model incorporating tool dynamic deflections and static errors of the machine. Their presented model is in good agreement with measured values.

Denkena et al. [Denkena, 2012] invented a reconstruction method for surface topographies in terms of peripheral milled surfaces based on measured cutting forces, and the presented model incorporated a dynamic tool model and material removal model to reconstruct the accurate shape and roughness of machined surfaces, and they insisted the developed model can be used for the online monitoring of milling process.

Arizmendi et al. [Arizmendi, 2009] presented a model to estimate surface topography during peripheral milling operations. The developed model incorporated the effect of tool vibrations concerning cutting-edge paths and equivalent polynomial equations. They stated that the developed model could be used to predict the roughness values and the form errors of the milled surface.

Liu and Rouch [Liu, 1991] proposed a design concept for an optimal passive dynamic absorber in the milling process. In this reference, they investigated a violent relative vibration between the workpiece and the cutting tool. Then they used a theoretical approach for predicting a machine tool chatter on a two-degree-of-freedom structural model simulation to improve the threshold of stability of the milling process. They found that the optimal passive dynamic absorber is better than the theoretical approach when predicting a machine tool chatter.

Seguy et al. [Seguy, 1991] investigated the effects of spindle speed on vibrations. In particular, a workpiece was flexible along the feed direction, whereas the tool was rigid in the high-speed domain. They found that the amplitude of vibration significantly impacts the stability of the milling process more than the frequency of vibration.

Rivière-Lorphèvre et al. [Rivière-Lorphèvre, 2019] incorporated a mechanistic model of the cutting force, a numerical model for the machine tool's dynamic response, and a geometrical model for predicting the shape of the cutting part, then conducted a dynamic simulation to obtain the cutting forces and vibrations with varying time steps. As a result, Rivière-Lorphèvre et al. [Rivière-Lorphèvre, 2019] found that a time step size in the iterative algorithm has little effect on results from two integration methods with single-pass and iterative algorithms. Otherwise, the results obtained by the iterative algorithm varied depending on the time step. Thus, they concluded that the iterative algorithm could obtain a more precise result with a given time step

and CPU time.

Wang et al. [Wang, 2019] invented a mathematical model to predict surface roughness for face milling process. They suggested three equations for surface roughness according to feed speed. They tested the geometrical models by machining 6061 aluminum alloy with a Grade K313 carbide tool with a nose radius of 0.397 (mm), and the accuracy of the geometrical model is listed in Table 1.1.

Table 1.1: Summary of surface finish prediction reference for the milling process [Wang, 2019].

Reference	Workpiece	Spindle speed (rpm)	Feed (mm/tooth)	Accuracy (%)
			0.0254	68.24
			0.127	45.79
			0.203	19.36
Wang et al.	Al6061	300	0.305	15.59
[Wang, 2019]			0.406	22.26
			0.508	16.04
			0.559	10.30
			0.635	7.52

Lu et al. [Lu, 2017] tried to predict the surface topography of the peripheral milling process using tool displacements and tool center point methodology. They incorporated tool deflection and recorded high-frequency tool vibrations to obtain the surface topography in 3D. Then, they computed the surface topography along the edges of the tool path by analyzing the recorded data. They insisted that the developed model has an error range of 11 to 23 (%) after comparing three cases of the simulated and experimental results. Similarly, Jiang et al. [Jiang, 2008] computed surface profiles by using a similar tool center point-based methodology, and the developed model has a 6 (%) Ra error on average from experimental values.

Omar et al. [Omar, 2007] investigated the 3D surface topography during the side-end milling operation. They presented a model based on a static cutting force model considering the cutter axis tilt, cutter runout, tool deflection, and the effect of clearance face wear. They insisted that the model could predict the conventional cutting forces and surface topography.

Kalidass et al. [Kalidass, 2014] studied the effect of helix angle and cutting conditions on machining performance, particularly surface roughness. They proved that helix angle significantly reduces surface roughness, and a smooth surface was obtained when a helix angle was between 35 to 40 degrees. In addition, with increasing spindle speed, smooth surface roughness was obtained.

Franco et al. [Franco, 2004a] proposed a numerical model to predict the surface profile and surface roughness by incorporating a random values generation algorithm,

and they insisted the numerical model can predict the surface profile and surface finish according to values of radial and axial runouts. Furthermore, they conducted milling experiments to check the validity of the numerical model. They found discrepancies because of undeformed chip thickness, tearing the workpiece material, and forming a build-up edge. Similarly, they investigated the effects of round insert cutting tools and radial and axial runouts on surface profiles. Exploring the numerical and experimental results, they found variations caused by undeformed chip thickness along the surface profile [Franco, 2004b].

Felho et al. [Felhó, 2015] introduced a method and a modeling software based on the theoretical model. Their model determined the surface roughness concerning the tool reference plane by calculating the kinematic relations of the cutting process. They argued that the proposed software had a good approximation with experimental results.

Pimenov et al. [Pimenov, 2019] investigated the influence of the relative position of the tool and workpiece on the milling performance. With varying radial immersions, they collected experimental cutting force and surface roughness data regarding the relative position of the face mill and workpiece. They insisted that the dynamic contact between the tooth and workpiece would cause forced vibrations and confirmed the increasing acceleration trend of vibration.

Lyu et al. [Lyu, 2021] developed a dynamometer based on a strain gauge structure since there is no high accuracy dynamometer for measuring cutting forces in the

machining process. When they compared experimental results between the developed dynamometer and a Kistler dynamometer, they found that the invented dynamometer is reliable for measuring high-frequency dynamic forces.

Vara et al. [Vara Prasad, 2020] proposed a mechanistic model to estimate machining characteristics regarding the chip geometry, such as cutting forces, tool vibration, and power consumption. They conducted milling experiments and finite element method-based numerical simulations to verify the model. As a result, they found a good correlation between the mechanistic model, experiments, and finite element method. They insisted that the accuracy of the mechanistic models is validated.

Maher et al. [Maher, 2014] conducted correlation analysis using adaptive neuro-fuzzy inference system (ANFIS) modeling to estimate the association between cutting parameters, cutting force, and surface roughness. They found that the ANFIS model can estimate surface roughness using a cutting force signal, and the average prediction accuracy is 96.65 (%).

This literature search concludes that there is no previous milling simulation model used to investigate the geometrical surface roughness concerning the effect of tool vibration using the Newmark method. In this paper, we introduced the geometrical surface finish prediction method concerning the effect of tool vibrations generated in the feed direction.

Chapter 2

Background Theory

2.1 Cutting force in milling process

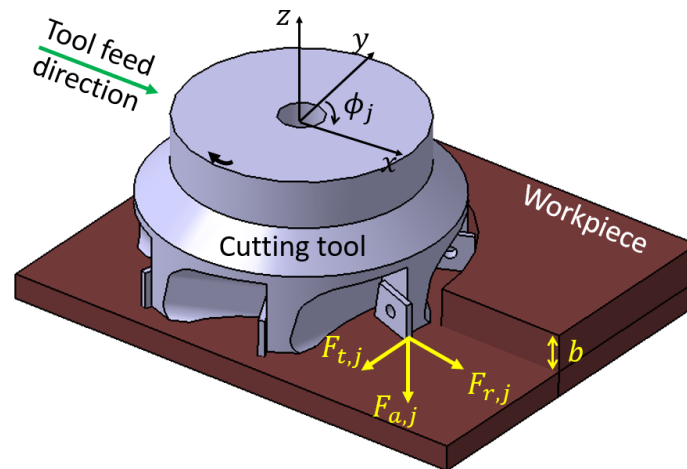


Figure 2.1: Schematic of tangential and normal cutting forces acting on the cutting tool [Schmitz, 2019].

Milling cutting forces are parameters to evaluate the performance of a milling process. Forces in the milling operation can be divided into three components, namely tangential, radial, and axial cutting forces. As illustrated in Figure 2.1, the tangential, radial, and axial cutting forces acting on a tooth are denoted as $F_{t,j}$, $F_{r,j}$, and $F_{a,j}$, respectively. While cutting forces in the x and y directions are derived from the forces

in the radial and tangential directions, the cutting force in the z direction is equal to the cutting force in the axial direction. However, all cutting forces are based on the chip cross-sectional area, where b is the axial depth-of-cut.

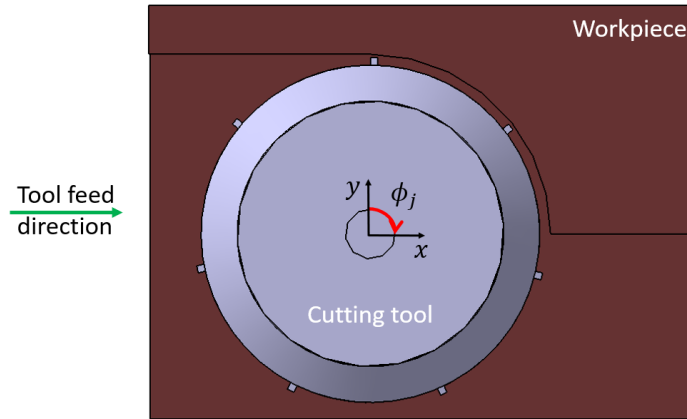


Figure 2.2: Schematic of cutting tool angle [Schmitz, 2019].

As shown in Figure 2.2, the tool angle, ϕ_j , is measured clockwise from the positive y -axis, and it can be seen that the tool will cut the workpiece from the angle of 0 to 90 degrees.

Many authors have studied the forces in milling operation and found that the tangential cutting force, acting on a tooth, is dependent on the chip cross-sectional area and tangential cutting force coefficient. Similarly, the radial or axial cutting force, acting on a cutting edge, are calculated by multiplying the chip cross-sectional area by the radial or axial cutting force coefficients [Kim, 1993]. A cutting force coefficient is a constant used to predict a cutting force, and it depends on the tool's geometry and the material properties of a workpiece. Moreover, it is not affected

by milling process parameters and is predicted by the orthogonal database [Altintas, 2012].

In the milling force models used by Schmitz and Smith [Schmitz, 2019], Chen et al. [Chen, 2019], and Insperger et al. [Insperger, 2004], the instantaneous chip thickness, $h(\phi_j)$, is obtained by using the current and previous tool vibrations as well as the projected path of the tool. Then, the instantaneous chip thickness is used to predict the cutting forces. The instantaneous chip thickness equation for the j th tooth, $h(\phi_j)$, is delivered to arrive at the time-dependent cutting force equations, and the instantaneous chip thickness equation becomes [Schmitz, 2019]:

$$h(\phi_j) = [\Delta x \sin(\phi_j) + \Delta y \cos(\phi_j)]g(\phi_j) \quad (2.1)$$

where Δx and Δy is the sum of vibration from the previous tooth and the current tooth for the x and y directions and the projected tool engagement on the workpiece in both x and y directions. ϕ_s , ϕ_e , and $g(\phi_j)$ represent the cut start angle, exit angle, and the switching function, respectively, and the switching function can be defined by [Schmitz, 2019] and [Shaik, 2016a]:

$$g(\phi_j) = \begin{cases} 1, & \text{if } \phi_s \leq \phi_j \leq \phi_e \\ 0, & \text{if } \phi_j < \phi_s, \phi_j > \phi_e \end{cases} \quad (2.2)$$

When it comes to milling cutter trajectory, Li et al. [Li, 2018] presented that the milling tool trajectory is comprised of the tool's rotation and rectilinear motion along the feed direction. In the Cartesian coordinate system, a tool trajectory at an initial polar point can be defined by Eq. (2.3) and (2.4):

$$x_0 = \frac{d}{2} \cos(\phi_j) \quad (2.3)$$

$$y_0 = \frac{d}{2} \sin(\phi_j) \quad (2.4)$$

where d and ϕ_j are the tool diameter and tool rotation angle, respectively. When it comes to the tool trajectory at j -th tooth considering vibrations, that can be defined by Eq. (2.5) and (2.6):

$$x_j = \left[\left(\frac{f_t \cdot N_t}{2\pi} \cdot \cos(\phi_j) + \sqrt{\left(\frac{d}{2}\right)^2 - \left(\frac{f_t \cdot N_t \cdot \sin(\phi_j)}{2\pi}\right)^2} \right) \cdot \cos(\phi_j) \right] + \Delta x(\phi_j) \quad (2.5)$$

$$y_j = \left[\left(\frac{f_t \cdot N_t}{2\pi} \cdot \cos(\phi_j) + \sqrt{\left(\frac{d}{2}\right)^2 - \left(\frac{f_t \cdot N_t \cdot \sin(\phi_j)}{2\pi}\right)^2} \right) \cdot \sin(\phi_j) \right] + \Delta y(\phi_j) \quad (2.6)$$

where $f_t, N_t, \phi_j, \Delta x(\phi_j)$, and $\Delta y(\phi_j)$ are feed per tooth, total number of teeth, the rotation angle of j -th tooth, and tool vibrations in the x and y directions, respectively.

The forces acting on the cutting edge, namely tangential cutting force, $F_{t,j}$, and radial cutting force, $F_{r,j}$, can be written as a function of the chip thickness [Schmitz, 2019] and [Shaik, 2016a]:

$$F_{t,j}(\phi_j) = K_{tc}bh(\phi_j) \quad (2.7)$$

$$F_{r,j}(\phi_j) = K_{rc}bh(\phi_j) \quad (2.8)$$

$$F_{a,j}(\phi_j) = K_{ac}bh(\phi_j) \quad (2.9)$$

where K_{tc}, K_{rc}, K_{ac} and b are tangential cutting force coefficient, radial cutting force coefficient, axial cutting force coefficient, and axial depth-of-cut. The tangential, radial cutting, and axial force coefficients are empirically determined according to the properties of the workpiece material. If cutting forces are expressed in the Cartesian coordinate system, the x and y direction force expression can be written as [Schmitz, 2019]:

$$F_{x,j}(\phi_j) = bh(\phi_j) \left[-K_{tc}\cos(\phi_j) - K_{rc}\sin(\phi_j) \right] \quad (2.10)$$

$$F_{y,j}(\phi_j) = bh(\phi_j) \left[K_{tc} \sin(\phi_j) - K_{rc} \cos(\phi_j) \right] \quad (2.11)$$

$$F_{z,j}(\phi_j) = -K_{ac}bh(\phi_j) \quad (2.12)$$

If a cutter has multiple teeth, the cutting force of all teeth can be written as [Schmitz, 2019]:

$$\begin{pmatrix} F_x(\phi_j) \\ F_y(\phi_j) \\ F_z(\phi_j) \end{pmatrix} = b \begin{bmatrix} a_{xx} & a_{xy} & 0 \\ a_{yx} & a_{yy} & 0 \\ a_{xz} & a_{yz} & 0 \end{bmatrix} \begin{pmatrix} \Delta x \\ \Delta y \\ 0 \end{pmatrix} \quad (2.13)$$

where the directional dynamic force coefficients are [Schmitz, 2019]:

$$a_{xx} = \sum_{j=1}^{N_t} g(\phi_j) \left[-K_{tc} \cos(\phi_j) \sin(\phi_j) - K_{rc} \sin^2(\phi_j) \right] \quad (2.14)$$

$$a_{xy} = \sum_{j=1}^{N_t} g(\phi_j) \left[-K_{tc} \cos^2(\phi_j) - K_{rc} \sin(\phi_j) \cos(\phi_j) \right] \quad (2.15)$$

$$a_{yx} = \sum_{j=1}^{N_t} g(\phi_j) \left[K_{tc} \sin^2(\phi_j) - K_{rc} \cos(\phi_j) \sin(\phi_j) \right] \quad (2.16)$$

$$a_{yy} = \sum_{j=1}^{N_t} g(\phi_j) \left[K_{tc} \sin(\phi_j) \cos(\phi_j) - K_{rc} \cos^2(\phi_j) \right] \quad (2.17)$$

$$a_{xz} = \sum_{j=1}^{N_t} g(\phi_j) \left[-K_{ac} \sin(\phi_j) \right] \quad (2.18)$$

$$a_{yz} = \sum_{j=1}^{N_t} g(\phi_j) \left[-K_{ac} \cos(\phi_j) \right] \quad (2.19)$$

The cutting forces, obtained by Equations (2.10) to (2.12), are used to predict the tool vibration by substituting into the mechanical motion of the equation.

2.2 Equation of mechanical motion in milling process

Single-degree of freedom of the system

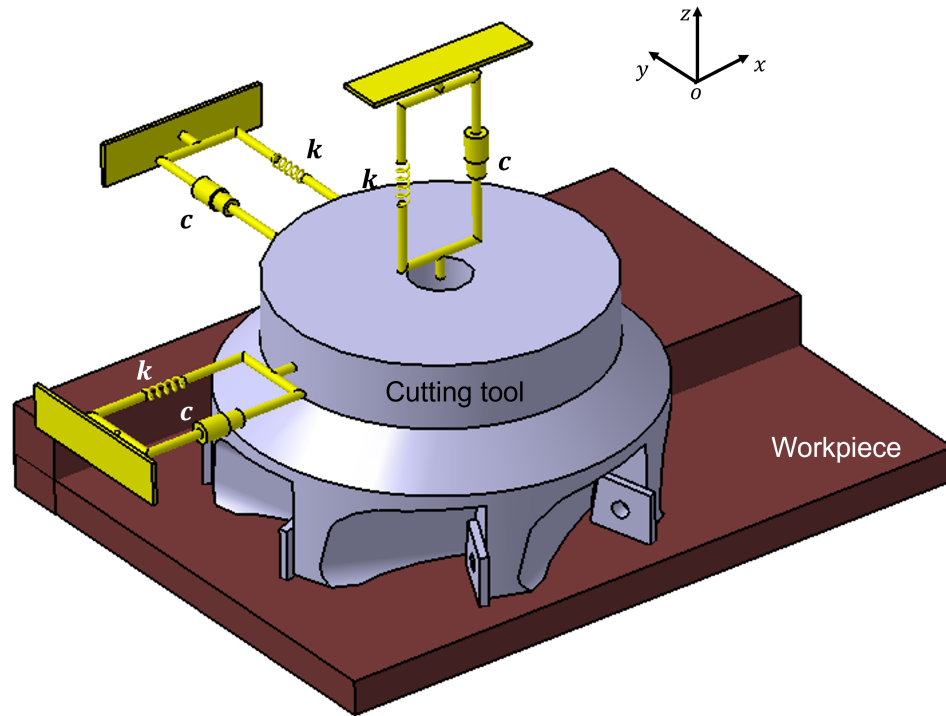


Figure 2.3: Schematic mechanical model of a cutting tool [Schmitz, 2019].

As shown in Fig 2.3 and Eq.(2.20), Schmitz and Smith [Schmitz, 2019] used a single degree-of-freedom model in the Cartesian coordinate system to predict the vibration caused by cutting forces in milling processes, and they solved this model using the Euler integration method. In this study, the mechanical motion of the equation is defined by [Schmitz, 2019]:

$$\begin{aligned}
& \begin{bmatrix} m & 0 & 0 \\ 0 & m & 0 \\ 0 & 0 & m \end{bmatrix} \begin{bmatrix} \ddot{x}(t) \\ \ddot{y}(t) \\ \ddot{z}(t) \end{bmatrix} + \begin{bmatrix} c & 0 & 0 \\ 0 & c & 0 \\ 0 & 0 & c \end{bmatrix} \begin{bmatrix} \dot{x}(t) \\ \dot{y}(t) \\ \dot{z}(t) \end{bmatrix} + \dots \\
& \dots + \begin{bmatrix} k & 0 & 0 \\ 0 & k & 0 \\ 0 & 0 & k \end{bmatrix} \begin{bmatrix} x(t) \\ y(t) \\ z(t) \end{bmatrix} = \begin{bmatrix} F_x(t) \\ F_y(t) \\ F_z(t) \end{bmatrix}
\end{aligned} \tag{2.20}$$

where m , c , and k are the modal mass, damping, and stiffness, respectively in the Cartesian coordinate system. The tool was assumed to be flexible with single degree-of-freedom, and the workpiece was rigid. The displacements are $x(t)$, $y(t)$, and $z(t)$, and milling forces are $F_x(t)$, $F_y(t)$, and $F_z(t)$.

2.3 Modal analysis

Modal analysis is widely used to determine the characterization of a system, such as natural frequency, damping, stiffness, etc. Vibration analysis is generally used in the classical approach to finding synthesized motions of a multi-degree-of-freedom system. To find natural frequencies and mode shapes of a system, the general equation of dynamics is defined by Eq.(2.21) where the structural system is considered to be no damping and no external load with finite degrees of freedom [Yu et al., 2019].

$$\mathbf{M} \times \ddot{\mathbf{U}} + \mathbf{K} \times \mathbf{U} = \mathbf{0} \quad (2.21)$$

In Eq.(2.21), \mathbf{M} , \mathbf{K} , \mathbf{U} , and $\ddot{\mathbf{U}}$ represent system mass matrix, system stiffness matrix, node displacement matrix, and the second derivative of node displacement matrix with respect to time, respectively. Solutions to Eq.(2.21) have the form as:

$$\mathbf{U} = \boldsymbol{\phi} \times \sin \boldsymbol{\omega} t \quad (2.22)$$

where $\boldsymbol{\phi}$, $\boldsymbol{\omega}$, and t represent modal shape of n th order, natural frequency, and time variable matrices, respectively. By substituting Eq.(2.22) into Eq.(2.21), the characteristic equation can be expressed by:

$$\mathbf{K} - \boldsymbol{\omega}^2 \times \mathbf{M} \times \boldsymbol{\phi} = 0 \quad (2.23)$$

When there is a non-zero solution, a solution to Eq. (2.23) is defined by:

$$\det (\mathbf{K} - \boldsymbol{\omega}^2 \times \mathbf{M} \times \boldsymbol{\phi}) = 0 \quad (2.24)$$

When the elastic continuum is discretized into i groups, Eq. (2.23) is transformed to:

$$(\mathbf{K} - \omega_i^2 \mathbf{M}) \times \phi_i = 0, \text{ where } i = 1, 2, 3, \dots, n \quad (2.25)$$

where n , \mathbf{K} , ω_i , and ϕ_i represent n th order, dimension of the stiffness matrix, i th natural frequency corresponding to the eigenvalue, and i th modal shape corresponding to the eigenvalue, respectively. Thus, in this study, the finite element method was used in Abaqus software to find the cutting tool's natural frequency and mechanical properties. Then the obtained mechanical properties of the tool were utilized in the numerical integration method to compute the tool's displacement change generated by cutting forces.

2.4 Newmark method

When a system is subjected to any type of nonperiodic force, the response of the system can be determined by analytical and numerical methods. Generally, convolution integral and Laplace transform methods are used to find an analytical solution. However, if a system is complex or impossible to find an analytical solution, a numerical method is a proper way to predict the system's behavior. Moreover, when a system is generated with the numerical method in the computer program language, it is fast and convenient to determine its behavior with various system parameters [Rao and Griffin, 2018].

In this study, the Newmark method was employed to evaluate the velocities and displacements for a single-degree of freedom system since the Newmark method has better accuracy than the Euler method. Moreover, the Newmark method has high accuracy when predicting the nonlinear dynamics of elasticity [Huang, 2019]. The Newmark method is a time integration method, which approximates the movement of the system, such as the displacement, velocity, and acceleration, and they are based on the data of the previous time step [Bo, 2014]. The Newmark method is a single-step integration method that is well suited for the time integration of a second-order differential equation of structural dynamics [Michel, 2015]. Time-domain numerical methods can be used to compute the true kinematics of the milling process due to their powerful ability. Furthermore, they can be used to solve the nonlinear problem

[Sallese, 2016]. Although nothing is known about the situation at time t_{n+1} , that can be assumed by the Newmark method given the displacement, velocity, and acceleration at time t_n . The Newmark integration scheme assumes the acceleration varies linearly between two instants of time. The resulting expressions for the displacement (u_{t+1}) and velocity (\dot{u}_{t+1}) are written as in Eq. (2.26) and (2.27) [Newmark, 1959]:

$$u_{t+1} = u_t + \Delta t \dot{u}_t + \frac{\Delta t^2}{2} \left[(1 - 2\beta)\ddot{u}_t + 2\beta\ddot{u}_{t+1} \right] \quad (2.26)$$

$$\dot{u}_{t+1} = \dot{u}_t + \Delta t \left[(1 - \gamma)\ddot{u}_t + \gamma\ddot{u}_{t+1} \right] \quad (2.27)$$

where β and γ are the Newmark parameters, they are used to determine how much the acceleration of the interval engages the velocity and displacement equation at the end of the interval, Δt . The integration interval (Δt) can be defined by [Schmitz, 2019]:

$$\Delta t = \frac{\phi \cdot 60}{\Omega \cdot 360} (s) \quad (2.28)$$

where ϕ and Ω represent tooth angle and spindle speed, respectively. Newmark [Newmark, 1959] found that when the quantity γ is not $1/2$, it results in incorrect damping.

If γ is less than $1/2$, it results in negative damping, which contains a self-excited vibration during the numerical procedure. Last, if γ is greater than $1/2$, positive damping is obtained, which results in the reduction of the magnitude of the response even without real damping in the problem [Newmark, 1959]. Therefore, γ is usually set as $1/2$. In addition, Newmark [Newmark, 1959] found that a small quantity of β makes the Newmark integration converge rapidly, and he defined two acceleration methods, as listed in Table 2.1, depending on a uniform value of acceleration during the time interval. We tried both the linear acceleration method and constant acceleration method with varying integration time step through convergence study by comparing homogeneous solution with simulation and arrived at better prediction results with the average acceleration method, hence we decided to use the average acceleration parameters to simplify computation.

Table 2.1: Newmark parameters ([Newmark, 1959])

	Linear acceleration method	Average acceleration method
β	$1/6$	$1/4$
γ	$1/2$	$1/2$

Integration time step

The development of computer technology allows us that the machining operations can be simulated with numerical methods. To simulate machining operations, Ozel et al. [E, 2015] used the finite element method, and Movahheddy [M, 2000] utilized the arbitrary Lagrangian-Eulerian finite element method, and Limido, et al [Limido, 2007] used meshless methods. Riviere-Lorphèvre et al. [Rivière-Lorphèvre, 2019] argued that the finite element method is too complex to simulate academic examples with a reasonable computing time. Generally, a time step, in the numerical method, is determined based on two constraints. One of the constraints for determining the time step is presented by Ming et al [Ming, 2016]. To simulate the high-frequency response of milling operations, the time step should be small enough. Classically, one-tenth of the smallest period of the system is proper. The other constraints for selecting a time step are mentioned by Peigne [Peigne, 2003], who argued that a time step should be small enough for simulating machined surface accurately, and generally, at least 30-time steps between the entry and exit of the cutting tool within the workpiece are proper. Dominantly, 30-time steps between the start and end of engagement of the cutter within the workpiece are considered [Rivière-Lorphèvre, 2019]. To observe the effect of time step on the Newmark integration method, one of the numerical examples is presented by [Insperger, 2016] and is listed in Table 2.2.

Table 2.2: Example case presented in [Insperger, 2016]

Parameter	Value
Cutting tool	Cylindrical end mill
Milling type	Up milling
Workpiece	7075-T6 aluminium alloy
Revolution	300
K_{tc} , tangential force coefficient (N/m ²)	550×10^6
K_{rc} , radial force coefficient (N/m ²)	200×10^6
m_x , modal mass in the x -direction (kg)	2.573
c_x , modal damping in the x -direction (N·s/m)	0.0032
k_x , modal stiffness in the the x -direction (N/m)	2.1801×10^6
ω_{nx} , tool's natural frequency in the x-direction (Hz)	146.5
d , tool diameter (mm)	19
Radial depth-of-cut (mm)	9.5
b , axial depth-of-cut (mm)	2
Ω , spindle speed (rpm)	16,000
f_t , feed (mm/tooth)	0.05
r_n , tool nose radius (mm)	0.397
N_t , tool teeth number	1
$x(0)$, initial displacement in the x -direction (m)	0
$\dot{x}(0)$, initial velocity in the x -direction (m/s)	0

To assess the effect of time step on simulated results of milling operations, two indicators are introduced in Smith [Smith, 1993]. One is the dominant frequency of the displacement signal that is the main chatter frequency. The other is the peak-to-peak (ptp) amplitude of the displacement signal. Response displacements for this

study were simulated in the time domain. Then Fast Fourier Transform (FFT) was used, with MATLAB software, to transform the time domain displacement to the frequency domain to determine peak-to-peak (ptp) amplitude and dominant frequency. In Equation 2.29, the Fourier series is expressed in discretized form [Avitabile, 2018].

$$S_x(m\Delta f) \approx \Delta t \sum_{n=0}^{N-1} x(n\Delta t) e^{-j2\pi(m\Delta f)(n\Delta t)} \quad (2.29)$$

Where m , Δt , N , and Δf are a discrete point, sample interval, number of data points, and frequency resolution, respectively.

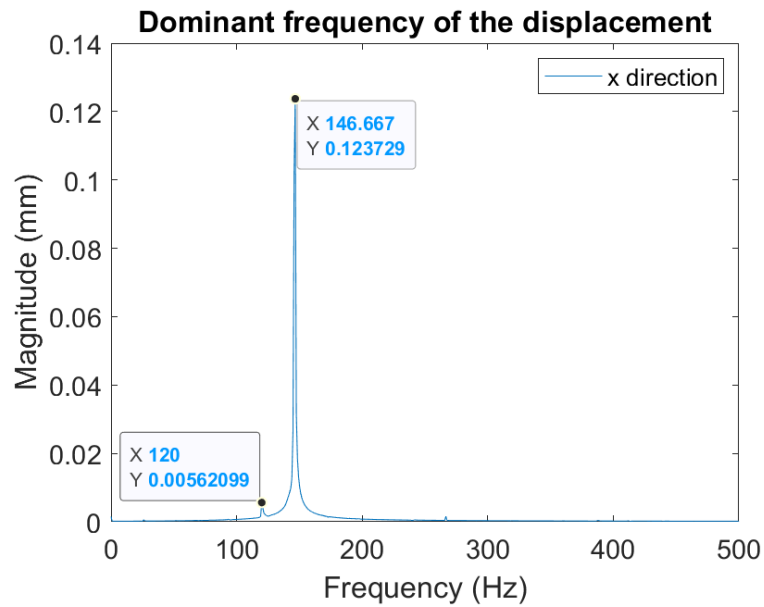


Figure 2.4: Newmark integration time step of 3.13×10^{-5} (sec).

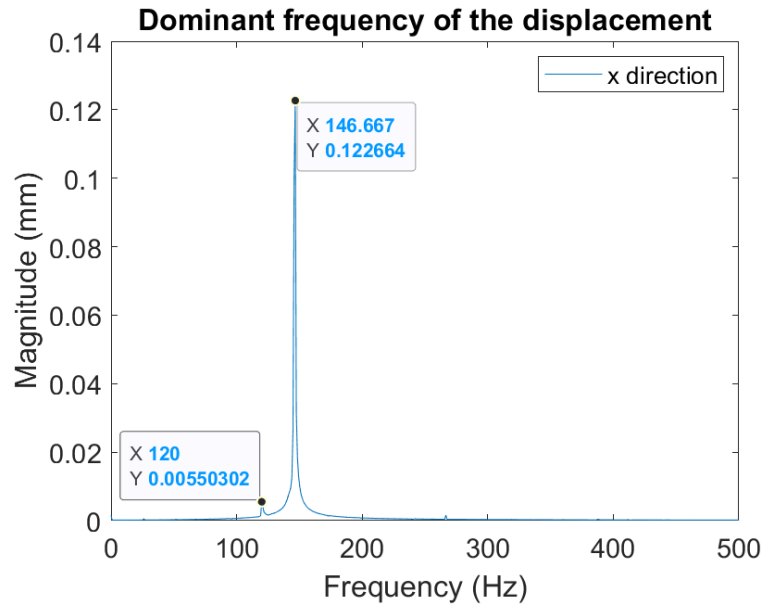


Figure 2.5: Newmark integration time step of 1.88×10^{-5} (sec).

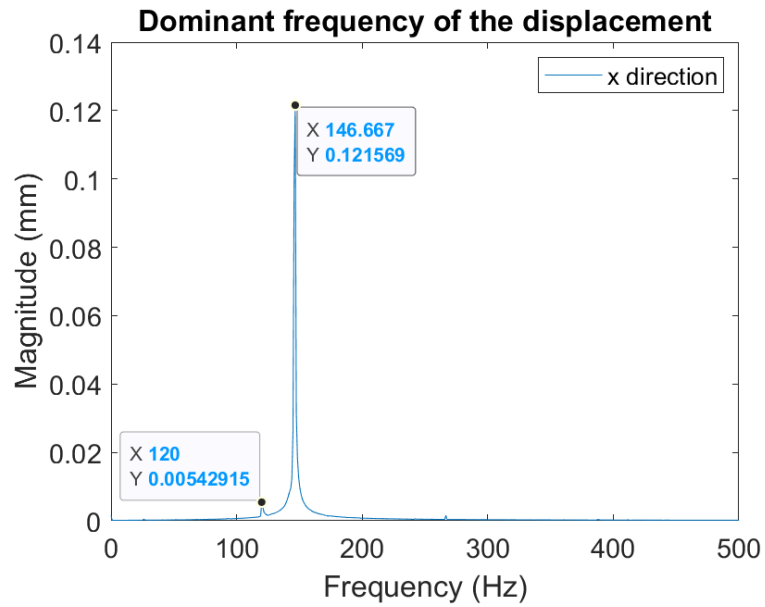


Figure 2.6: Newmark integration time step of 9.4×10^{-6} (sec).

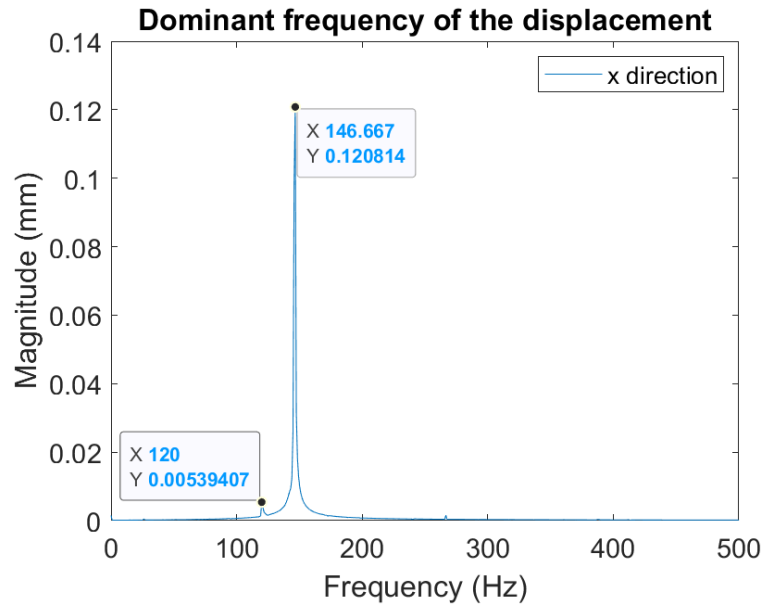


Figure 2.7: Newmark integration time step of 3.8×10^{-6} (sec).

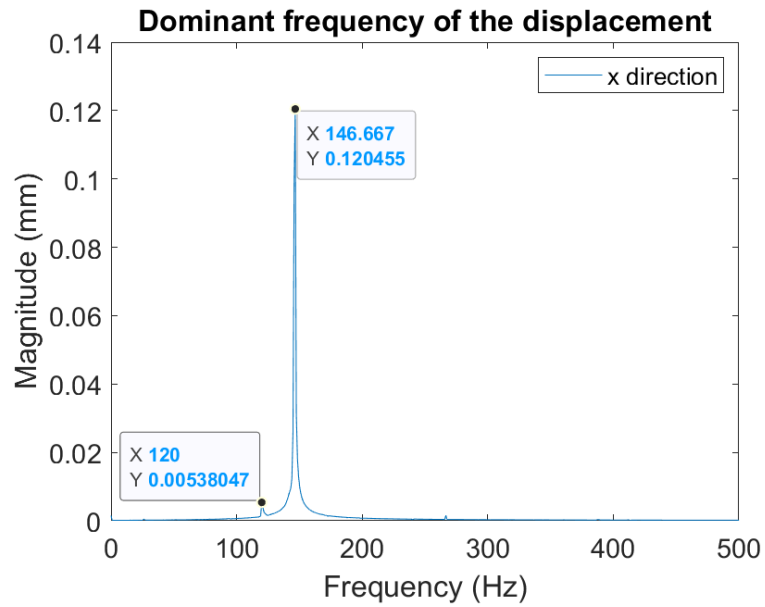


Figure 2.8: Newmark integration time step of 1.3×10^{-6} (sec).

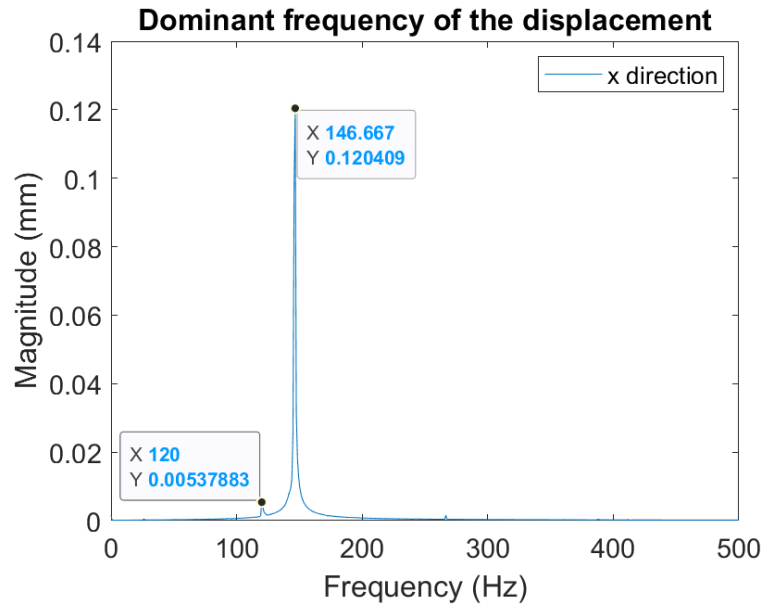


Figure 2.9: Newmark integration time step of 9.4×10^{-7} (sec).

In Figures 2.4 through 2.9, the vibrations are expressed in the frequency domain with varying time step of the Newmark method, and their peak to peak frequency and CPU run-time are summarized in Table 2.3.

Table 2.3: Summary of Figure 2.4

Time step (sec)	Total data point	Peak to Peak (mm)	$f_{chatter}$ (Hz)	CPU time (sec)
3.13×10^{-5}	36,000	0.118	146.67	4.68
1.88×10^{-5}	60,000	0.117	146.67	5.52
9.38×10^{-6}	120,000	0.116	146.67	7.28
3.75×10^{-6}	300,000	0.115	146.67	91.45
1.25×10^{-6}	900,000	0.115	146.67	817.29
9.38×10^{-7}	1,200,000	0.115	146.67	1485.19

As listed in Table 2.3, the time step of 1.25×10^{-6} was selected to perform the milling simulation using the Newmark method since the integration time step is an important factor affecting the numerical simulation result.

2.5 Surface roughness prediction

Geometrical surface roughness prediction for square insert

Munoz-Escalona and Maropoulos [Munoz-Escalona and Maropoulos, 2015] presented a geometrical model for surface roughness prediction. As shown in Figure 2.10, the tool nose section and the wipe edge of the square geometry are incorporated to predict the surface finish.

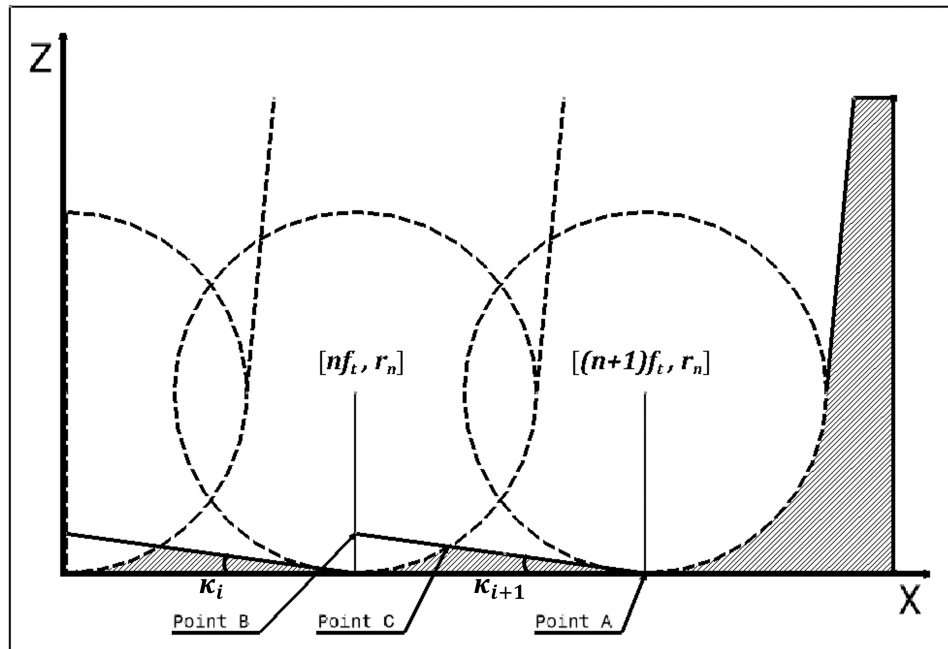


Figure 2.10: Schematic of surface roughness after milling with square insert [Munoz-Escalona and Maropoulos, 2015].

When the coordinates of the center of a circle are X_n and Z_n , equation (2.30) expresses the negative section of the square root of the circle equation.

$$Z = Z_n - \sqrt{r_n^2 - (X - X_n)^2} \quad (2.30)$$

According to the feed and tool nose radius, the coordinates of the circle center can be defined as:

$$X_n = n \cdot f_t \quad (2.31)$$

$$Z_n = r_n \quad (2.32)$$

where n , f_t , and r_n are n th feed marks, feed speed (mm/tooth), and tool nose radius.

Thus, the center of the circle at the $(n + 1)$ th feed mark is expressed by:

$$X_{n+1} = (n + 1) \cdot f_t \quad (2.33)$$

$$Z_{n+1} = r_n \quad (2.34)$$

In similar, the coordinates at point A are:

$$X_a = (n + 1) \cdot f_t \quad (2.35)$$

$$Z_a = 0 \quad (2.36)$$

The equation of the line between points A and B are:

$$Z = mX + Z_b \quad (2.37)$$

where the slope m is $-\tan(\kappa_{i+1})$, substituting equations (2.35) and (2.36) into equation (2.37), it becomes:

$$Z_b = [(n + 1) \cdot f_t] \cdot \tan(\kappa_{i+1}) \quad (2.38)$$

Then substituting equation (2.38) into equation (2.37), it becomes:

$$Z = -\tan(\kappa_{i+1}) \cdot [X - (n + 1)f_t] \quad (2.39)$$

Utilizing the relation of equations of the line and circle, the coordinates at the inter-

section (point C) are derived by:

$$\begin{aligned}
 X_c &= \frac{-m \cdot (Z_b - Z_n) - X_n}{m^2 + 1} + \dots \\
 \dots + &\frac{\sqrt{[m \cdot (Z_b - Z_n) - X_n]^2 - (m^2 + 1) \cdot [(Z_b - Z_n)^2 + X_n^2 - r_n^2]}}{m^2 + 1}
 \end{aligned} \tag{2.40}$$

$$Z_c = -\tan(\kappa_{i+1}) \cdot [X_c - (n + 1)f_t] \tag{2.41}$$

Finally, the height at point C is considered to be Z_c , and it corresponds to the surface roughness value. Furthermore, in this study, tool vibrations that were computed by the Newmark method were considered in the schematic of surface roughness after the milling operation with a square insert since relative tool vibration is also one of the important factors affecting surface roughness values.

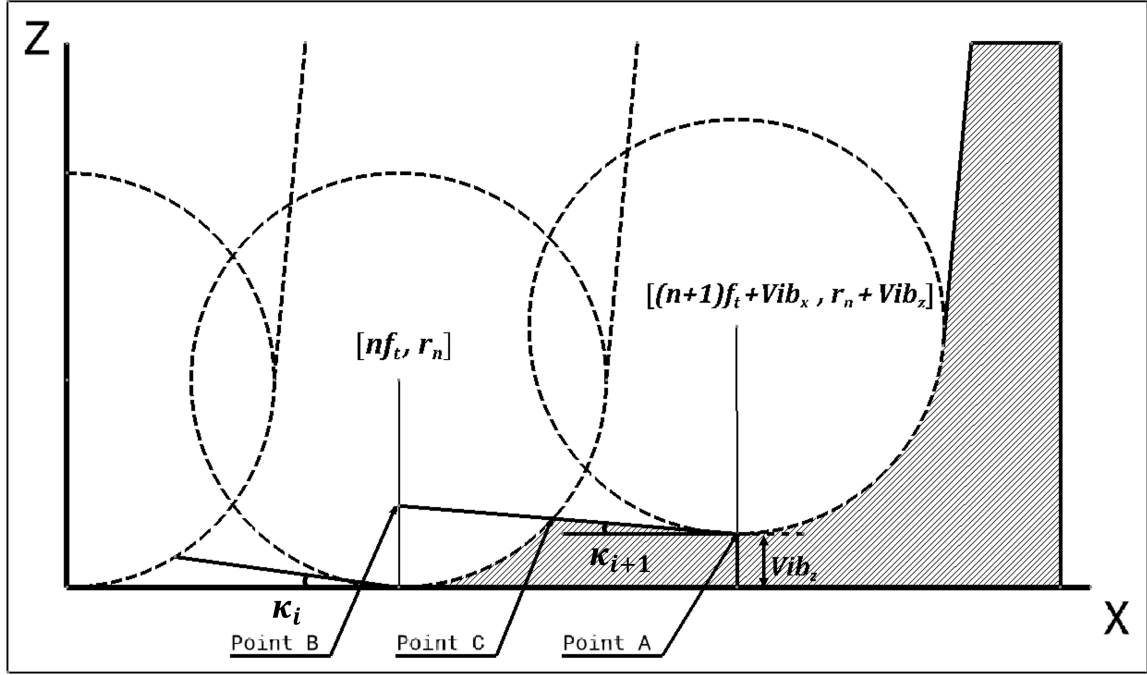


Figure 2.11: Schematic of surface roughness considering tool vibrations [Munoz-Escalona and Maropoulos, 2015].

As shown in Figure 2.11, when the tool moves along the feed length, tool vibrations generated by cutting forces will change surface roughness values by making the tool moves unintended way. Therefore, the maximum and minimum magnitude of tool vibrations with respect to the feed (x) and axial (z) directions were used to predict the surface roughness value.

When considering tool vibrations, the center of the circle at the $(n + 1)$ th feed mark, equations (2.33) and (2.34) are transformed to:

$$X_{n+1} = (n + 1) \cdot f_t + \text{Vib}_x \quad (2.42)$$

$$Z_{n+1} = r_n + \text{Vib}_z \quad (2.43)$$

where Vib_x is the tool vibration in the x -direction. Also the coordinates at Point A become:

$$X_a = (n + 1) \cdot f_t + \text{Vib}_x \quad (2.44)$$

$$Z_a = \text{Vib}_z \quad (2.45)$$

where Vib_z is the tool vibration in the z -direction. In similar, substituting equations (2.44) and (2.45) into equation (2.37), the height at Point B is:

$$Z_b = \left((n + 1) \cdot (f_t + \text{Vib}_x) \right) \cdot \tan(\kappa_{i+1}) + \text{Vib}_z \quad (2.46)$$

Then substituting equation (2.46) into equation (2.39), the equation of line AC can be defined by:

$$Z = -\tan(\kappa_{i+1}) \cdot \left[X - \left((n+1) \cdot (f_t + \text{Vib}_x) \right) \right] + \text{Vib}_z \quad (2.47)$$

According to the relation of equations of the line and circle, the coordinates at point C can be defined by:

$$\begin{aligned} X_c &= \frac{-m \cdot (Z_b - Z_n) - X_n}{m^2 + 1} + \dots \\ \dots + &\frac{\sqrt{[m \cdot (Z_b - Z_n) - X_n]^2 - (m^2 + 1) \cdot [(Z_b - Z_n)^2 + X_n^2 - r_n^2]}}{m^2 + 1} \end{aligned} \quad (2.48)$$

$$Z_c = -\tan(\kappa_{i+1}) \cdot \left[X_c - \left((n+1) \cdot (f_t + \text{Vib}_x) \right) \right] + \text{Vib}_z \quad (2.49)$$

Mathematical surface roughness prediction

In similar, Qu et al. [Qu, 2003] presented a mathematical surface profile to predict the machined surface roughness. As shown in Figure 2.12, it is composed of elliptical arcs that is formed by the shape of the tool. This model assumes only a single tooth is used to generate the surface profile as shown in Figure 2.12.

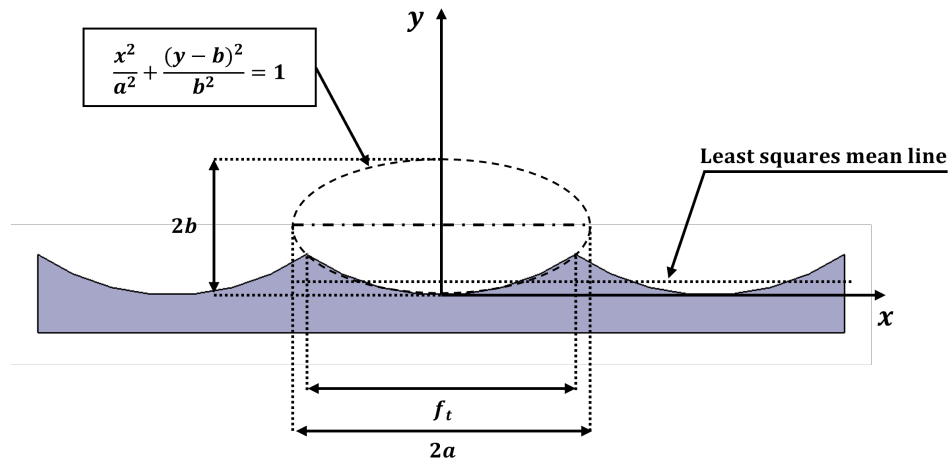


Figure 2.12: A mathematical surface profile consisting of elliptical arcs [Qu, 2003].

$$Ra = \frac{1}{f_t} \int_{-f_t/2}^{f_t/2} |y - \bar{y}| dx \quad (2.50)$$

where f_t and \bar{y} are feed (mm/tooth) and least-squares mean line of the mathematical profile indicated in Figure 2.12, respectively. Using feed and height of parabolic curves, the elliptical arcs can be assumed by [Qu, 2003]:

$$Ra \cong \frac{4}{9\sqrt{3}} \left(b - \frac{b}{a} \sqrt{a^2 - \frac{f_t}{4}} \right) \quad (2.51)$$

where $f_t^2 \ll ab$, Eq. (2.51) can be simplified to [Qu, 2003]:

$$Ra = 0.032 \frac{f_t^2 b}{a^2} \quad (2.52)$$

When the cutting tool nose is round, we can substitute the tool radius, r_n into a and b , the mathematical surface roughness equation becomes [Qu, 2003]:

$$Ra = 0.032 \frac{f_t^2}{r_n} \quad (2.53)$$

The position of a tool's edge is associated with the vibrations, and the relative motion between the cutter and workpiece impacts the uncut chip thickness variation [Montgomery, 1991]. As shown in Figure 2.13, vibration in the cutting tool is assumed to cause the tool to deviate from the prescribed feed, f_t . Therefore, the maximum (VA_{max}) and minimum (VA_{min}) magnitude of tool vibrations are changing the feed to have a possible range of surface roughness.

Eq. (2.53) is transformed to Eq. (2.54) where VA_{min} and VA_{max} are the minimum and maximum magnitude of the tool vibrations in the x (feed) direction, respectively.

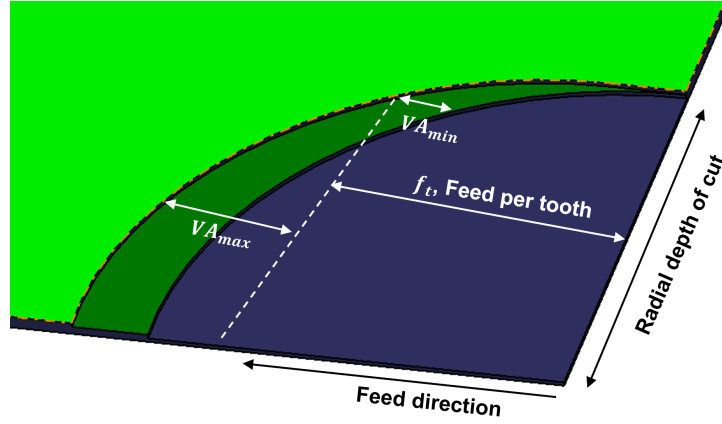


Figure 2.13: Effect of vibration on feed per tooth.

If the range of predicted surface roughness is large, it can be assumed that the surface finish will not be close to the mathematical value.

$$0.032 \frac{(f_t - VA_{min})^2}{r_n} \leq Ra \leq 0.032 \frac{(f_t + VA_{max})^2}{r_n} \quad (2.54)$$

As shown in Eq. (2.54), the minimum and maximum magnitude of vibration along the x -direction, obtained by solving Equation (2.20) with the Newmark method, are applied to the mathematical surface roughness equation. The minimum vibration takes place in the opposite direction of feed, which makes a tool move less than the given feed per tooth. On the other end, the maximum vibration will make a tool move more than the given feed per tooth. As a result, a range of machined surface roughness, considering the effect of vibration, will be predicted by Equation (2.54).

Chapter 3

Experimental setup

To validate the surface roughness prediction, milling tests were conducted using Doosan Mynx 6500/40, shown in Figure 3.1. The milling experiments were carried out under similar conditions to the simulation to investigate the surface roughness.



Figure 3.1: CNC milling machine.

The milling experiments were performed on Al6061-T651, which has a dimension of

60 x 100 x 30 (mm) as shown in Figure 3.2. The coolant used in this study is TRIM E860KS with a concentration of eight percent.

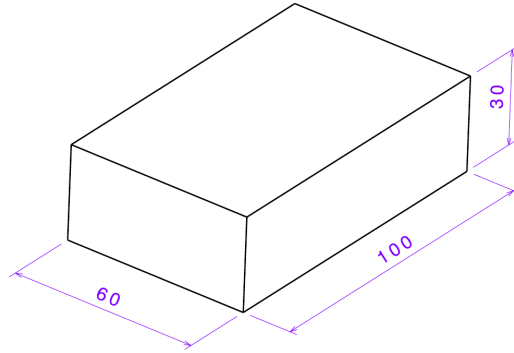


Figure 3.2: Dimensions of the workpiece (mm).

In this experiment, the DAEGUTECH indexable milling cutter and the DAEGUTECH milling insert shown in Figures 3.3 and 3.5 were utilized, and the MISUMI BT40-FMA31-75-45 arbor was used.

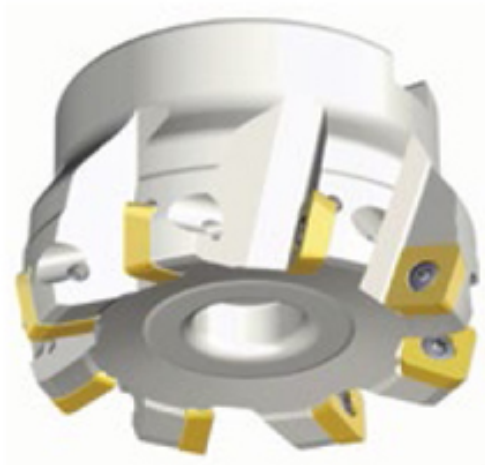


Figure 3.3: DAEGUTECH, indexable milling cutter, SCRM75SP-6100-32R-12B.

The indexable milling cutter is capable of mounting six tooth inserts, and the specification of the tool including dimensions and critical parameters, is shown in Fig. 3.4 and listed in Table 3.1.

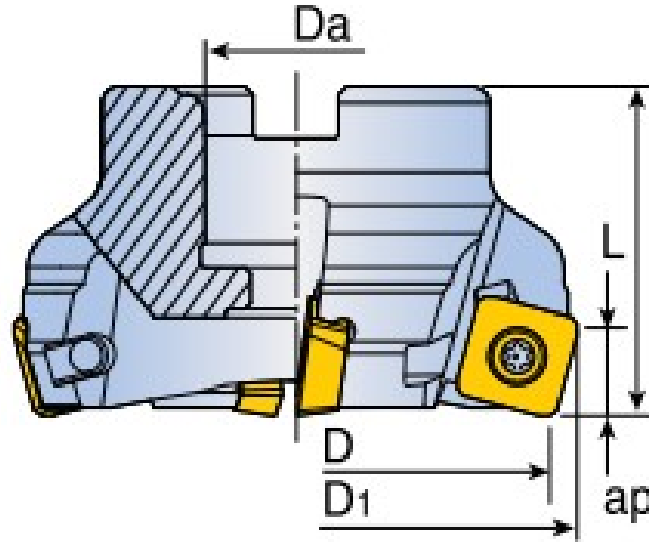


Figure 3.4: Dimensions and critical parameters of the indexable tool assembly.

Table 3.1: Specifications of the tool assembly.

D (mm)	D ₁ (mm)	L (mm)	ap (mm)	Da (mm)
100	105.4	50	8	32

The specification of the insert including dimensions and critical parameters is shown in Fig. 3.5 and listed in Table 3.2.

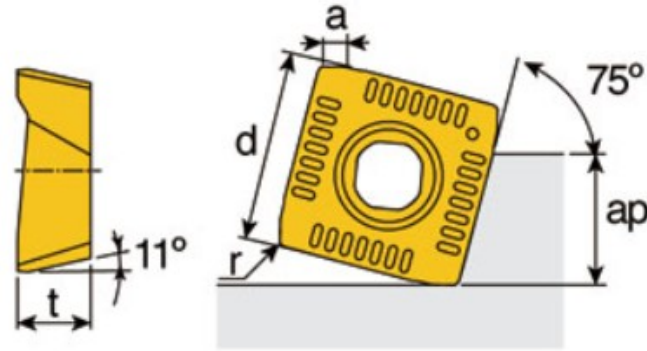


Figure 3.5: DAEGUTECH, milling insert, SPKT-1204-EDTR-HP.

Table 3.2: Specifications of the milling insert.

d (mm)	t (mm)	ap (mm)	a (mm)	r (mm)
12.7-12.86	4.66-5.56	8	1.4-2.2	0.4-0.8

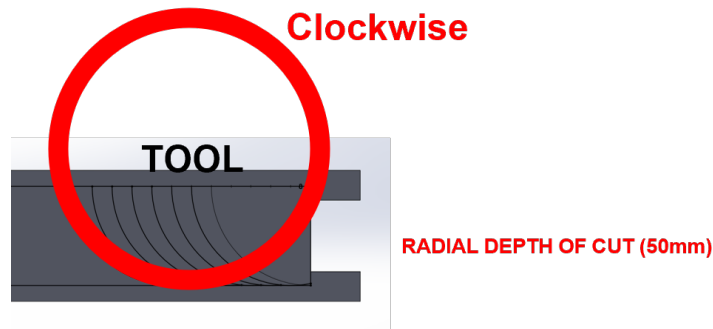


Figure 3.6: Milling experiment schematic.

In the experiment, a milling insert was mounted to the indexable milling cutter, and the milling tool was rotated in the clockwise direction shown in Figure 3.6. In Table 3.3, milling parameters were listed, and a total of 24 experiments were carried out according to three types of axial depth of cuts with varying feed speeds. For all milling

experiments, the radial depth-of-cut of 50 mm was utilized, and the G-code for the CNC milling operations is listed in Appendix B.

Table 3.3: Milling parameters for experiments

Test number	Spindle (rev/min)	Feed (mm/min)	Feed per tooth (mm/tooth)	Axial depth of cut (mm)
1	300	7.62	0.0254	0.15
2	300	38.1	0.127	0.15
3	300	60.9	0.203	0.15
4	300	91.5	0.305	0.15
5	300	121.8	0.406	0.15
6	300	152.4	0.508	0.15
7	300	167.7	0.559	0.15
8	300	190.5	0.635	0.15
9	300	7.62	0.0254	1
10	300	38.1	0.127	1
11	300	60.9	0.203	1
12	300	91.5	0.305	1
13	300	121.8	0.406	1

Continued on next page

Table 3.3 – Continued from previous page

Test number	Spindle (rev/min)	Feed (mm/min)	Feed per tooth (mm/tooth)	Axial depth of cut (mm)
14	300	152.4	0.508	1
15	300	167.7	0.559	1
16	300	190.5	0.635	1
17	300	7.62	0.0254	5
18	300	38.1	0.127	5
19	300	60.9	0.203	5
20	300	91.5	0.305	5
21	300	121.8	0.406	5
22	300	152.4	0.508	5
23	300	167.7	0.559	5
24	300	190.5	0.635	5

Marsurf PS10 was used to measure the machined surface roughness. The machined blocks were set on their sides so that the machined surface was horizontal. The roughness measurement was performed nine times along the horizontal line of the workpiece. After dividing the machined surface into six areas, each area was measured

three times. Thus a total of 27 readings were performed on each machined surface.

A profilometer probe was set at 15.24 mm for each surface roughness measurement.

Chapter 4

Results and Discussion

4.1 Modal analysis with finite element method

In this study, the finite element method was used to find mode shapes, natural frequencies, and mechanical properties of the cutting tool. When the eigenvalues are obtained by solving the characteristic equation, the natural frequencies are simply the square root of the eigenvalues. Therefore, if a system has n active degree of freedom, n natural frequencies will be obtained. Prior to exploring vibration analysis through the finite element analysis, the milling tool was designed by Catia V5 based on Figures 3.4 and 3.5. As shown in Figure 4.1, the cutting tool was broken into 47,528 elements using 10-node tetrahedron elements since they have high accuracy when complex model's designs. The material properties presented in Table 4.1 are from [Liu and Liu, 2013] and were used for the modal analysis. In this study, Abaqus software was used to conduct the vibration analysis of the cutting tool, and the results are listed in Table 4.1. An Intel Core i7 10th generation computer with 12 GB RAM was used for the Abaqus software, and the program runtime was 61.8 seconds with a

time step is 10^{-36} seconds.

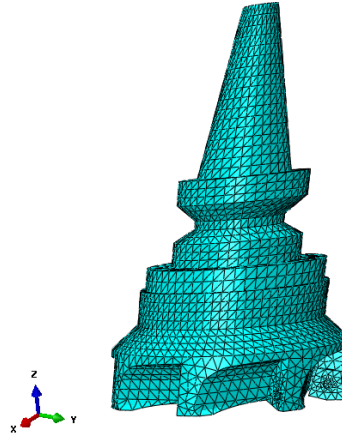


Figure 4.1: Meshing of the milling tool assembly.

Table 4.1: Material properties for cutting tool presented by [Liu and Liu, 2013]

Parameter	Value
Young's Modulus (GPa)	211
Poisson's ratio	0.277
Density (kg/m^3)	7870

Table 4.2: Modal mass results from the finite element analysis

x -component	y -component	z -component
(kg)	(kg)	(kg)
1.6452	1.6449	1.6847

When the modal effective mass represents the amount of mass moving in a particular direction, the mode is considered significant when the ratio of effective mass to the total mass is close to 1, since a high magnitude of the participation factor means that the system is the most easily excited by an excitation in the direction. Table 4.1 lists the modal mass obtained by the finite element analysis. The system mode at the 2nd, 1st, and 11th modes were considered In order of x , y , and z directions to decide the mechanical properties of the tool.

Table 4.3: Natural frequency and participation factor results obtained by modal analysis

Mode number	Frequency (rad/sec)	Participation factors		
		x-component	y-component	z-component
1	2123.50	-0.24	1.72	0.01
2	2126.50	1.62	0.22	0.00
3	2585.50	-0.02	0.00	0.00
4	3031.40	0.00	-0.04	0.02
5	3049.20	0.00	0.00	0.00
6	4037.20	0.00	-0.04	1.48
7	4559.90	-0.02	-1.61	-0.08
8	4579.10	-1.40	0.02	0.00

Continued on next page

Table 4.3 – Continued from previous page

Mode number	Frequency (rad/sec)	Participation factors		
		x-component	y-component	z-component
9	4917.90	0.03	0.18	-0.25
10	4972.30	0.00	0.00	0.00
11	5435.30	0.02	0.01	-2.10
12	5962.20	-0.77	-0.26	-0.42
13	6047.90	0.19	-0.42	-0.05
14	6126.90	0.07	0.03	-0.03
15	6153.10	0.02	0.00	-0.01
16	6669.30	-0.49	-0.39	0.00
17	6673.60	0.30	-0.41	0.02
18	6997.60	0.59	0.11	-0.38
19	7318.70	-0.01	0.11	0.10
20	7338.40	0.00	0.02	0.03
21	7347.10	0.01	0.01	0.01
22	7786.40	0.00	0.04	0.67
23	7964.70	0.00	-0.06	0.24
24	7999.60	0.02	0.00	-0.01

Continued on next page

Table 4.3 – Continued from previous page

Mode number	Frequency (rad/sec)	Participation factors		
		x-component	y-component	z-component
25	8423.30	0.17	0.15	-0.70
26	8440.60	1.51	0.41	0.57
27	8465.30	-0.54	1.65	0.11
28	8757.50	-0.02	0.05	0.01
29	8778.40	0.02	0.03	0.09
30	8877.40	0.01	0.01	0.03

Table 4.3 represents the participation factors and natural frequencies at their respective mode. Figures 4.2 through 4.4 show the cutting tool's mode shapes at the 2nd, 1st, and 11th modes.

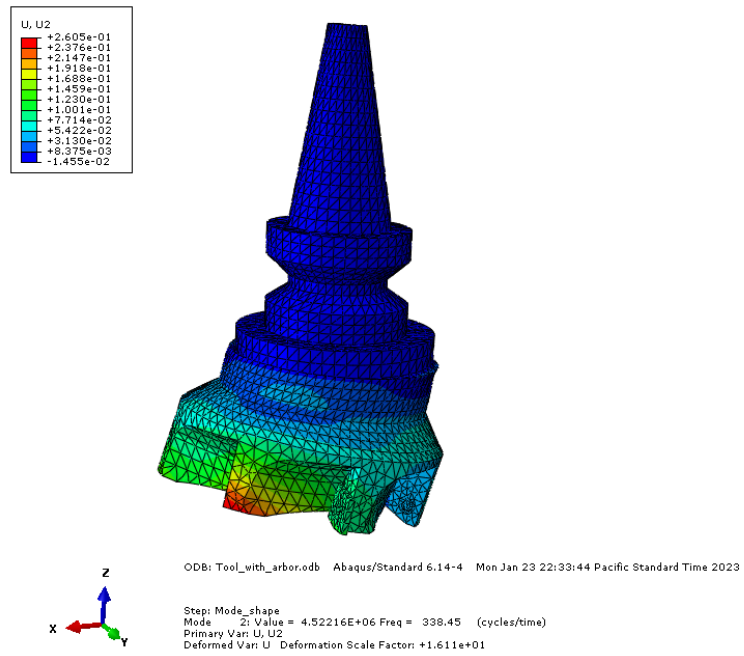


Figure 4.2: 2nd mode shape of the cutting tool.

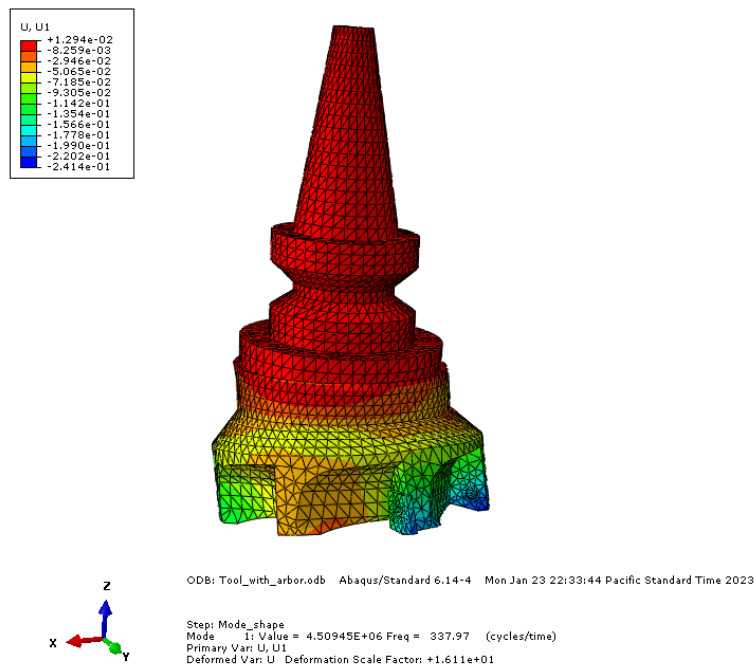


Figure 4.3: 1st mode shape of the cutting tool.

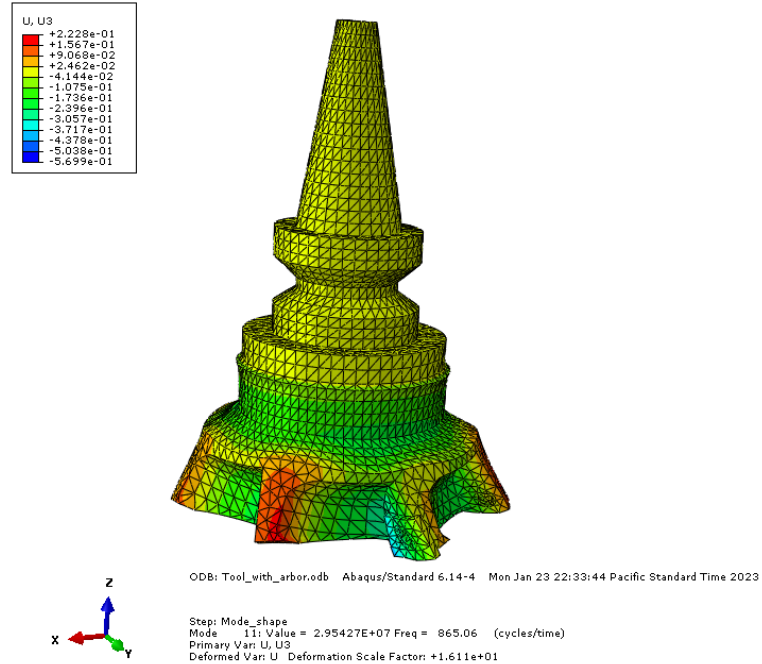


Figure 4.4: 11th mode shape of the cutting tool.

When the given system's damping ratio (ζ) is not known, it can be assumed by Rayleigh damping. Rayleigh damping is defined as [Shaik, 2016b]:

$$c = \alpha m + \beta k \quad (4.1)$$

where α , β , m , c , and k represent the mass damping factor, stiffness damping factor, mass, damping, and stiffness. Shaik and Srinivas [Shaik, 2020] suggested the mass damping and stiffness factors are 17.32 and 3.67×10^{-6} when the damping ratio for the entire integrated spindle tool unit is 1%.

Table 4.4: Computed mechanical properties of cutting tool

Direction	Natural frequency (rad/sec)	Mass (kg)	Stiffness (N/m)	Damping (N· s/m)
x	2126.5	1.6452	7.44×10^6	55.80
y	2123.5	1.6449	7.42×10^6	55.71
z	5435.3	1.6847	4.98×10^7	211.84

According to the modal analysis and Rayleigh damping method, the mechanical properties of the cutting tool were computed and listed in Table 4.4, and the mechanical properties of the cutting tool were used for the milling process simulation with Newmark method.

4.2 Milling process simulation with Newmark method

Although the finite element method is commonly used to analyze the dynamic behavior of structures, the Newmark integration method was selected to compute cutting forces and tool vibrations in the end milling process because a complex modeling process would not only be required to perform FEA simulation but could also result in incorrect assumptions leading to inaccurate results. Moreover, performing multiple simulations using the finite element method can be challenging when a system is complex. Therefore, in this study, the Newmark integration method was used to compute the cutting forces and tool vibrations during the milling process, and the proposed simulation model was developed using MATLAB R2021a. The input data to the program included the tool properties (number of teeth, tool nose radius, modal mass, damping, stiffness), feed, spindle speed, workpiece properties, axial and radial depth-of-cuts, cutting force coefficients. The cutting conditions used in this study were identical to the conditions listed in Table 4.5 and 4.6, which allowed us to predict cutting forces and tool vibrations through the Newmark method. In particular, the modal mass, damping, and stiffness properties of the tool were derived from the modal analysis with the finite element method. We used an Intel Core i7 10th generation computer with 12 GB of RAM, and the program run time was about 25 sec.

Table 4.5: Simulation parameters used in this study are taken from Wang et al. [[Wang, 2019], [Omar, 2007], [Schmitz, 2019],[Tsai et al., 2016]], and Table 4.4.

Parameter	Value
Tool insert specification	SPKT-1204-EDTR-HP
d , tool diameter (mm)	105.4
Radial depth-of-cut (mm)	50
b , axial depth-of-cut (mm)	0.15, 1, and 5
Revolution of the tool	10
Spindle speed (rpm)	300
r_n , tool nose radius (mm)	0.8
N_t , tool teeth number	1
β , Force angle (degree)	75
K_{tc} , tangential force coefficient (N/m ²)	745.1×10^6
K_{rc} , radial force coefficient (N/m ²)	360.98×10^6
K_{ac} , axial force coefficient (N/m ²)	182.85×10^6
m_x , mass in the x -direction (kg)	1.6452
m_y , mass in the y -direction (kg)	1.6449
m_z , mass in the z -direction (kg)	1.6847
c_x , damping in the x -direction (N·s/m)	55.80
c_y , damping in the y -direction (N·s/m)	55.71

c_z , damping in the z -direction (N· s/m)	211.84
k_x , stiffness in the x -direction (N/m)	7.44×10^6
k_y , stiffness in the y -direction (N/m)	7.42×10^6
k_z , stiffness in the z -direction (N/m)	4.98×10^7
$x(0)$, initial displacement in the x -direction (m)	0
$\dot{x}(0)$, initial velocity in the x -direction (m/s)	0
$y(0)$, initial displacement in the y -direction (m)	0
$\dot{y}(0)$, initial velocity in the y -direction (m/s)	0
$z(0)$, initial displacement in the z -direction (m)	0
$\dot{z}(0)$, initial velocity in the z -direction (m/s)	0
ω_{nx} , tool's natural frequency in the x -direction (rad/s)	2126.5
ω_{ny} , tool's natural frequency in the y -direction (rad/s)	2123.5
ω_{nz} , tool's natural frequency in the z -direction (rad/s)	5435.3
Workpiece material	6061 Aluminum alloy

In addition, various feed per tooth, as listed in Table 4.6, are suggested by Wang et al. [Wang, 2019] for finishing cut. In this study, the feed rates were also varied to inspect the correlation between cutting forces and vibrations and their effects on the surface roughness. Since the radial depth-of-cut was 50 mm, the cutter started to engage the workpiece between ϕ of 0 to 87.06 degrees, as shown in Figure 2.1.

Table 4.6: Simulated feed per tooth that was used in this study [Wang, 2019].

<hr/>							
<i>f_t</i> , feed (mm/tooth)							
<hr/>							
0.0254	0.127	0.203	0.305	0.406	0.508	0.559	0.635
<hr/>							

Cutting force results with the axial depth-of-cut: 0.15 mm

The cutting forces in the x , y , and z directions were computed from the radial, tangential, and axial cutting force components, as shown in equations (2.7), (2.8), and (2.9). We then varied the feed per tooth, as listed in Table 4.6, and computed the cutting forces in the x , y , and z directions to observe the effect of feed on them. The results are shown in Figures 4.5 through 4.28.

Cutting force in the x -direction

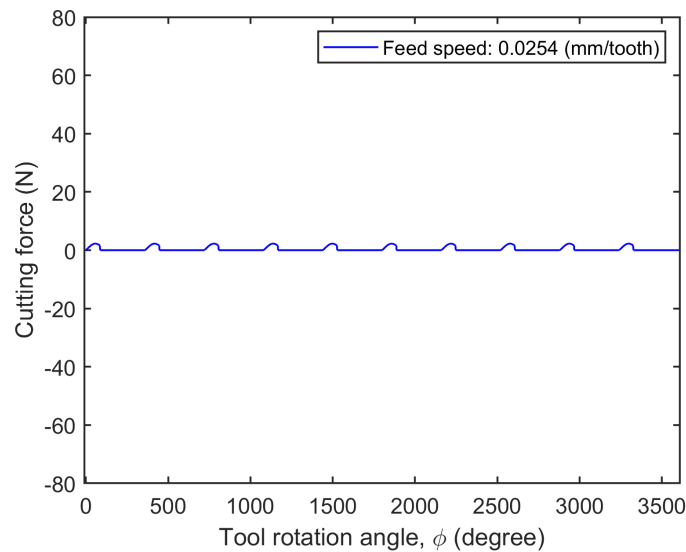


Figure 4.5: Cutting force in the x -direction at feed: 0.0254 (mm/tooth) and axial depth-of-cut: 0.15 (mm).

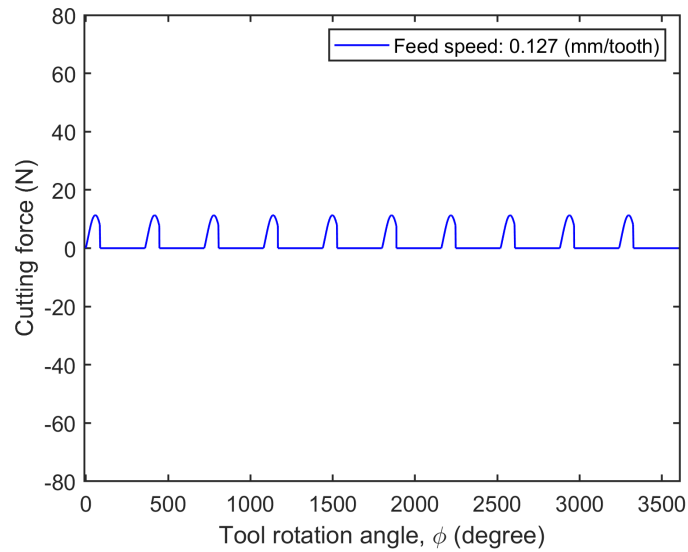


Figure 4.6: Cutting force in the x -direction at feed: 0.127 (mm/tooth) and axial depth-of-cut: 0.15 (mm).

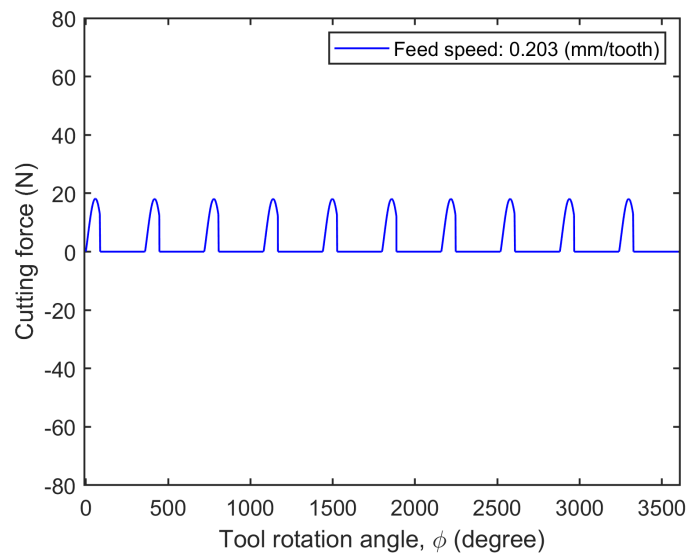


Figure 4.7: Cutting force in the x -direction at feed: 0.203 (mm/tooth) and axial depth-of-cut: 0.15 (mm).

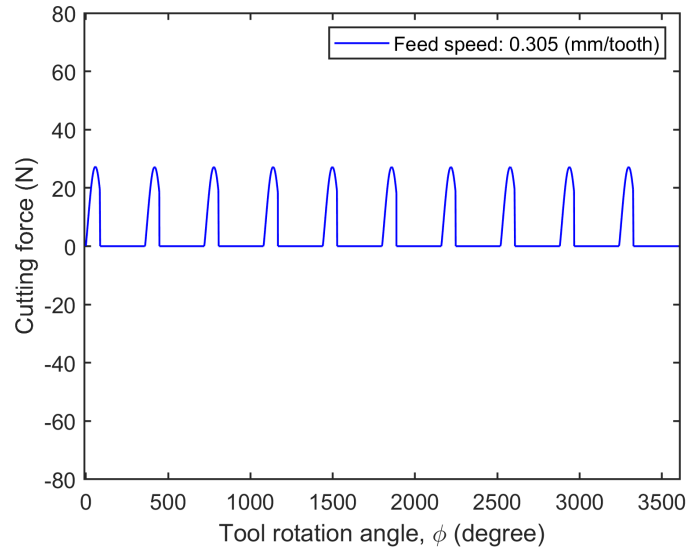


Figure 4.8: Cutting force in the x -direction at feed: 0.305 (mm/tooth) and axial depth-of-cut: 0.15 (mm).

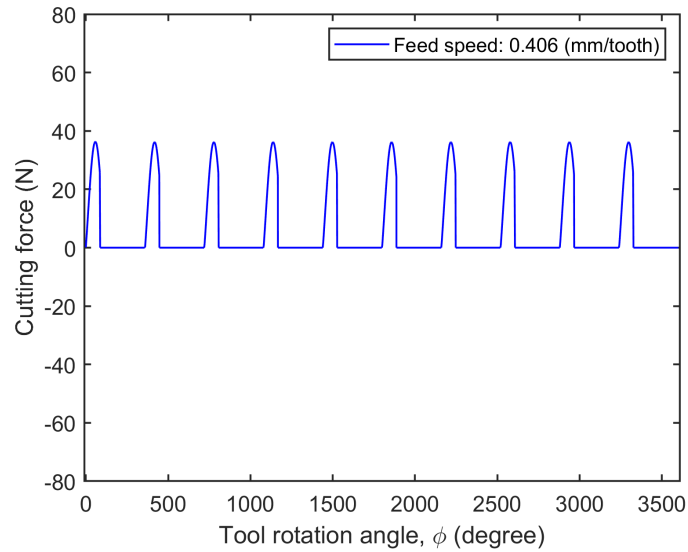


Figure 4.9: Cutting force in the x -direction at feed: 0.406 (mm/tooth) and axial depth-of-cut: 0.15 (mm).

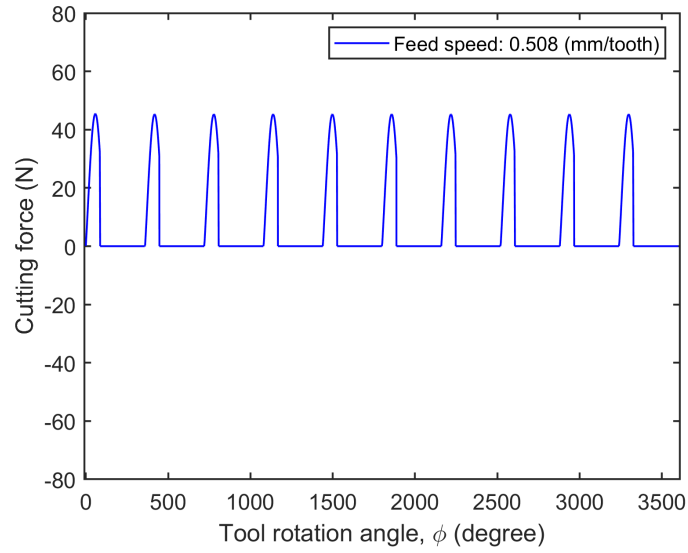


Figure 4.10: Cutting force in the x -direction at feed: 0.508 (mm/tooth) and axial depth-of-cut: 0.15 (mm).

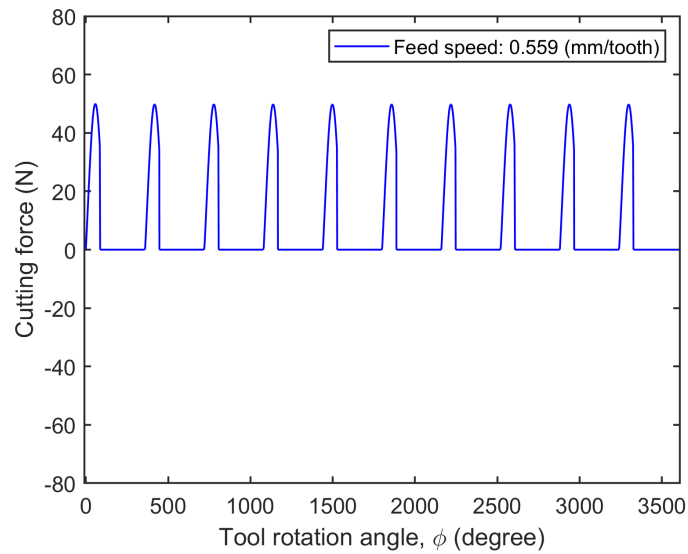


Figure 4.11: Cutting force in the x -direction at feed: 0.559 (mm/tooth) and axial depth-of-cut: 0.15 (mm).

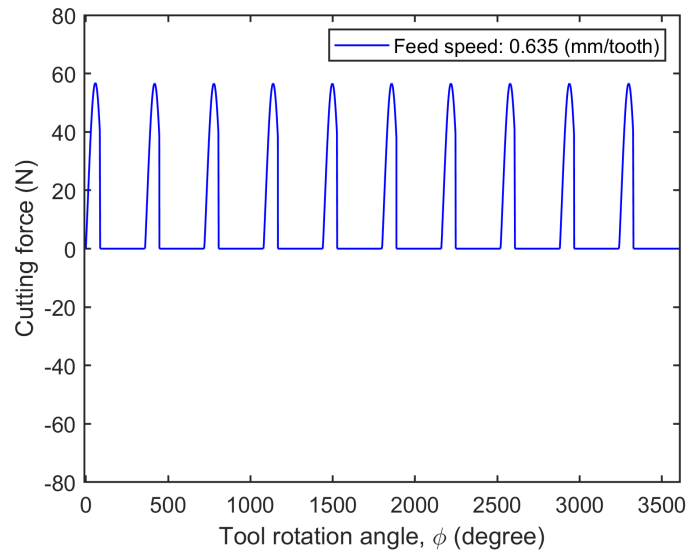


Figure 4.12: Cutting force in the x -direction at feed: 0.635 (mm/tooth) and axial depth-of-cut: 0.15 (mm).

Cutting force in the y -direction

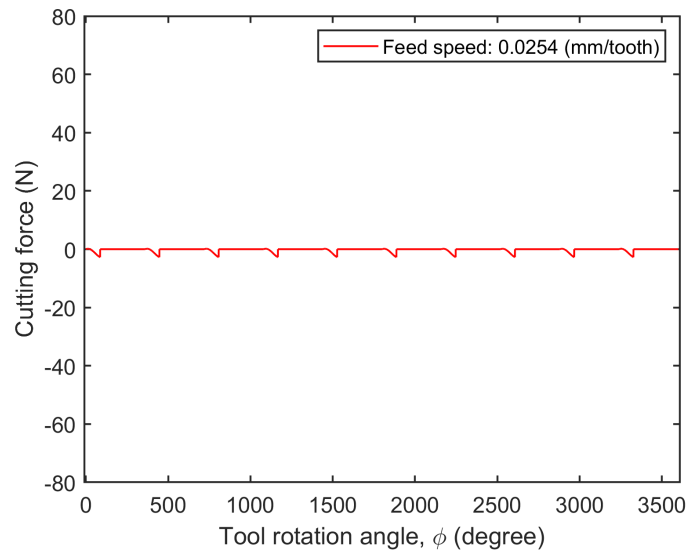


Figure 4.13: Cutting force in the y -direction at feed: 0.0254 (mm/tooth) and axial depth-of-cut: 0.15 (mm).

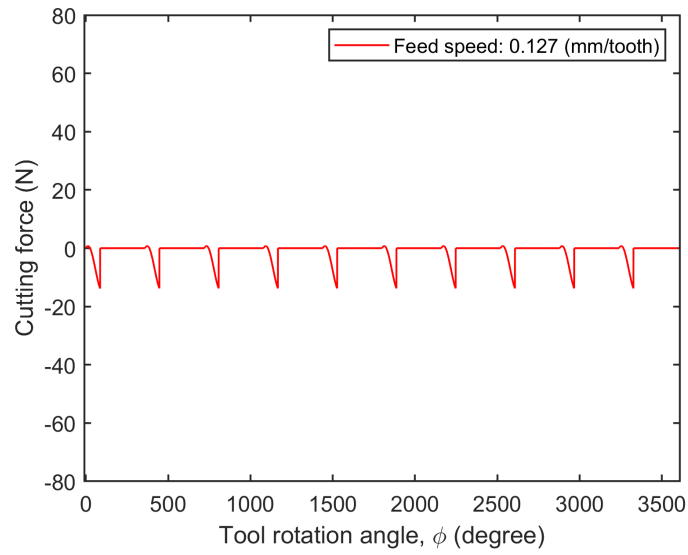


Figure 4.14: Cutting force in the y -direction at feed: 0.127 (mm/tooth) and axial depth-of-cut: 0.15 (mm).

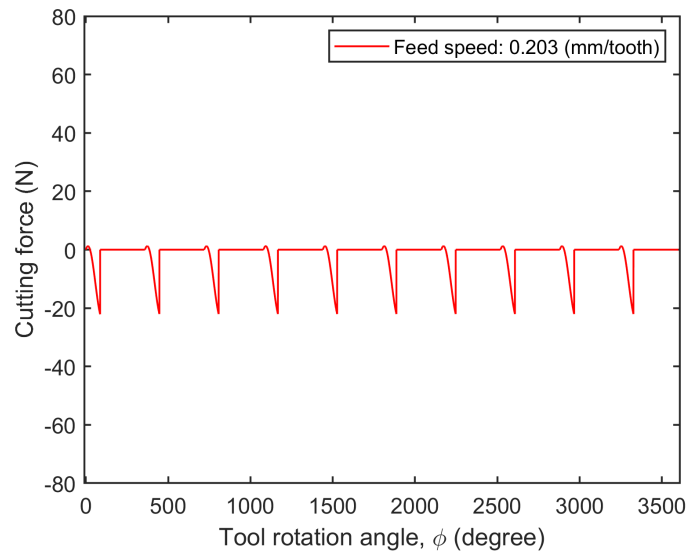


Figure 4.15: Cutting force in the y -direction at feed: 0.203 (mm/tooth) and axial depth-of-cut: 0.15 (mm).

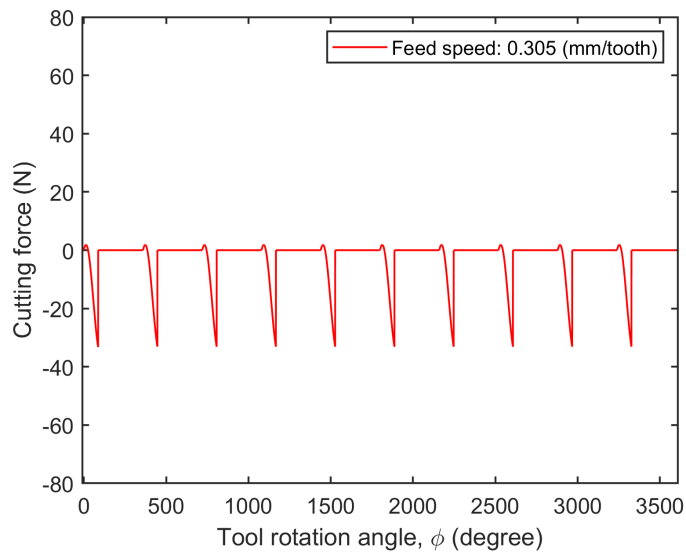


Figure 4.16: Cutting force in the y -direction at feed: 0.305 (mm/tooth) and axial depth-of-cut: 0.15 (mm).

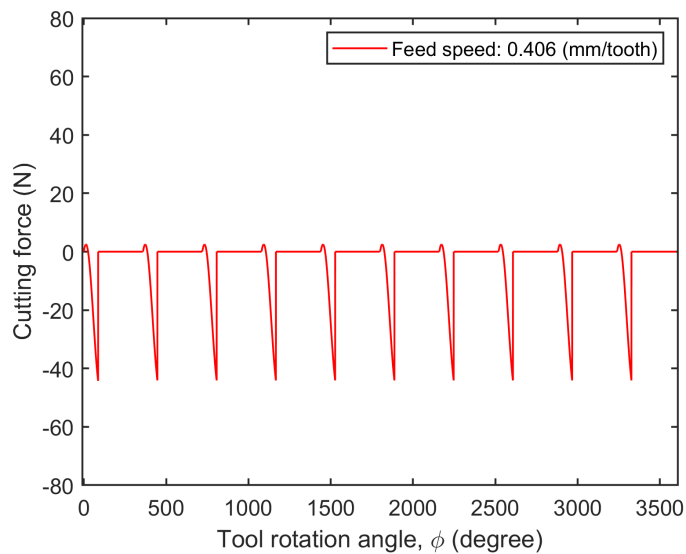


Figure 4.17: Cutting force in the y -direction at feed: 0.406 (mm/tooth) and axial depth-of-cut: 0.15 (mm).

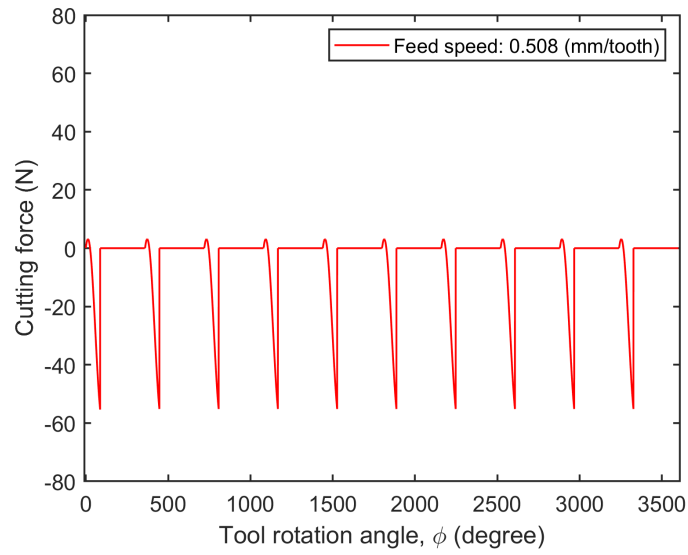


Figure 4.18: Cutting force in the y -direction at feed: 0.508 (mm/tooth) and axial depth-of-cut: 0.15 (mm).

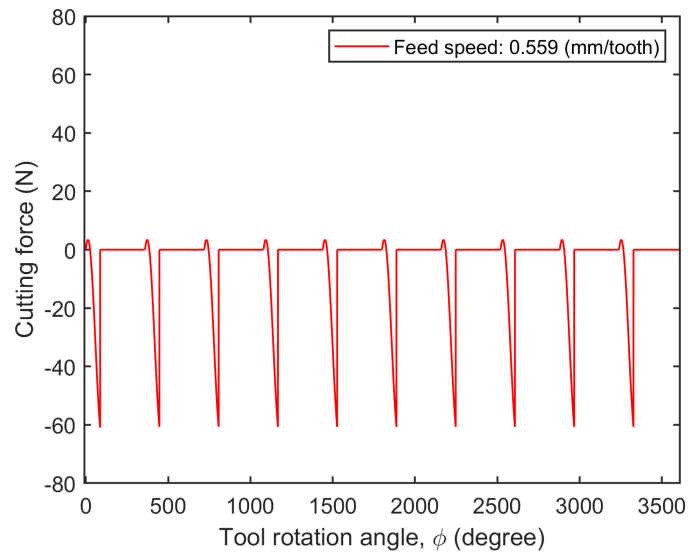


Figure 4.19: Cutting force in the y -direction at feed: 0.559 (mm/tooth) and axial depth-of-cut: 0.15 (mm).

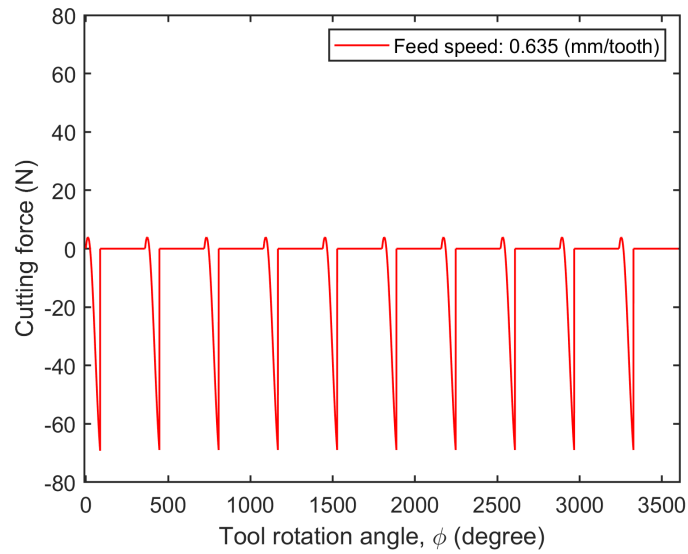


Figure 4.20: Cutting force in the y -direction at feed: 0.635 (mm/tooth) and axial depth-of-cut: 0.15 (mm).

Cutting force in the z -direction

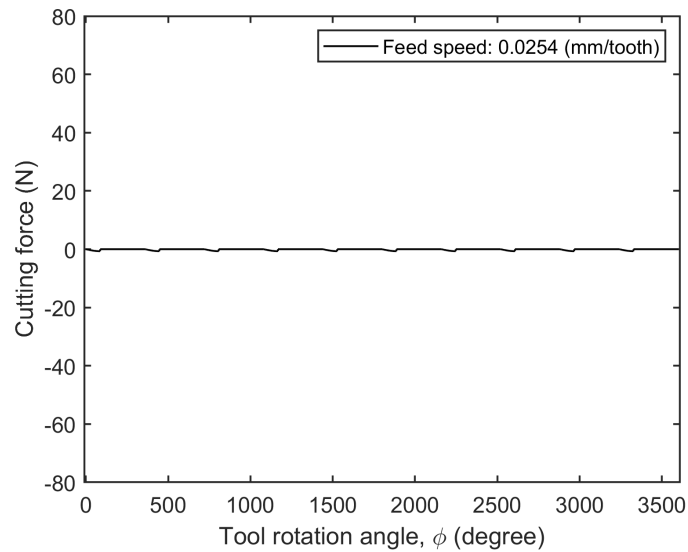


Figure 4.21: Cutting force in the z -direction at feed: 0.0254 (mm/tooth) and axial depth-of-cut: 0.15 (mm).

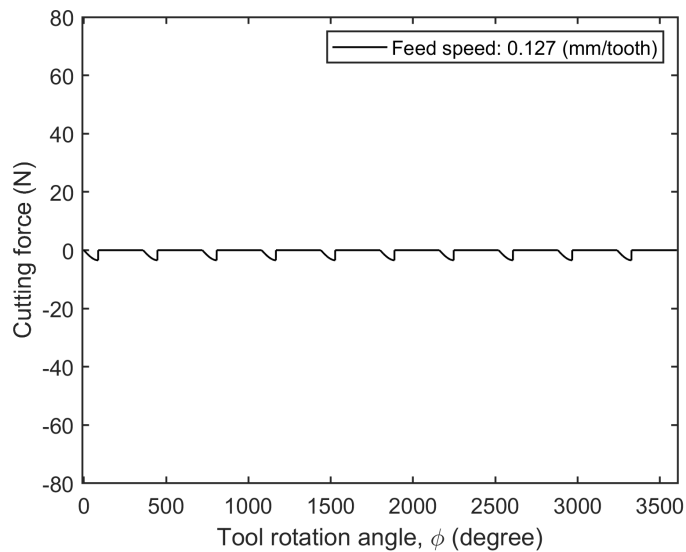


Figure 4.22: Cutting force in the z -direction at feed: 0.127 (mm/tooth) and axial depth-of-cut: 0.15 (mm).

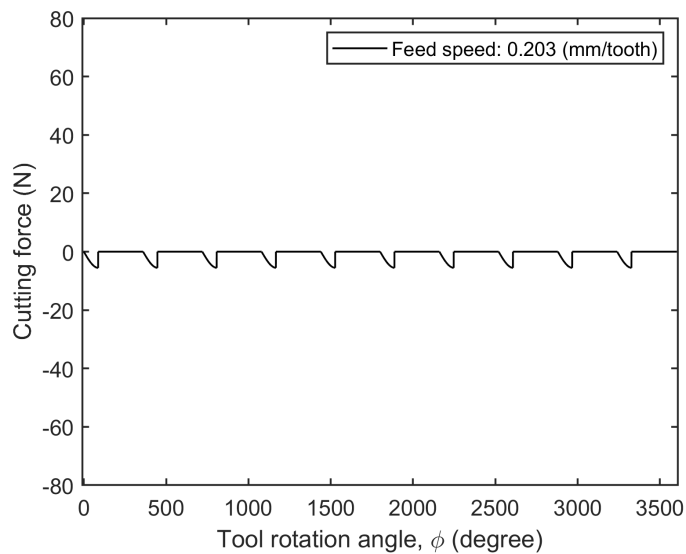


Figure 4.23: Cutting force in the z -direction at feed: 0.203 (mm/tooth) and axial depth-of-cut: 0.15 (mm).

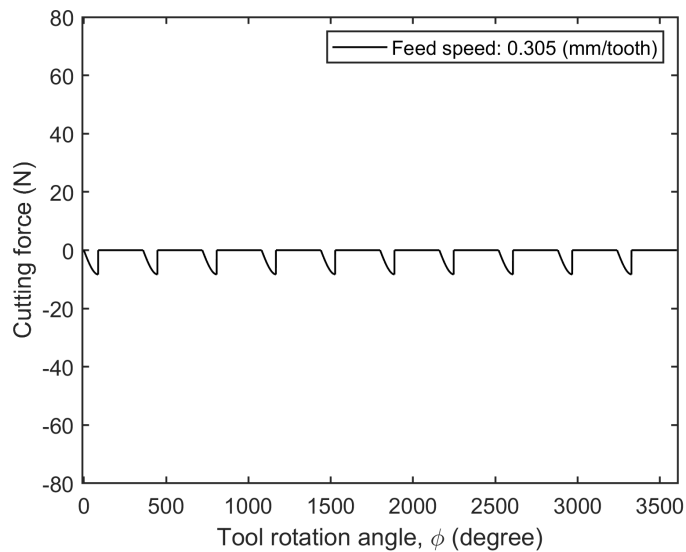


Figure 4.24: Cutting force in the z -direction at feed: 0.305 (mm/tooth) and axial depth-of-cut: 0.15 (mm).

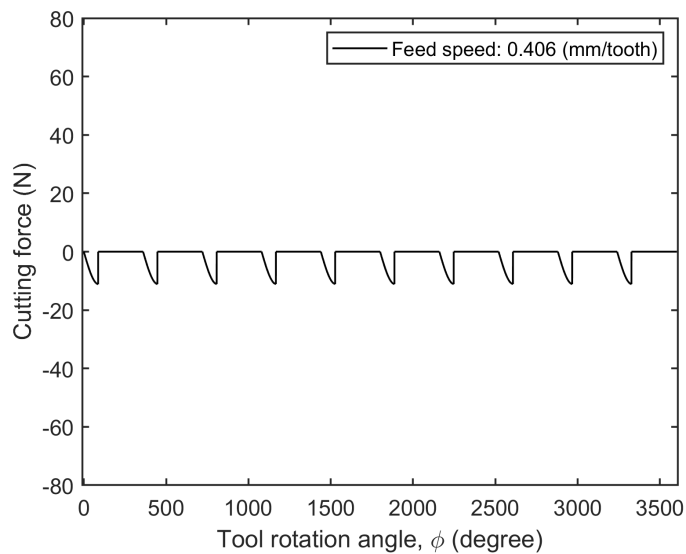


Figure 4.25: Cutting force in the z -direction at feed: 0.406 (mm/tooth) and axial depth-of-cut: 0.15 (mm).

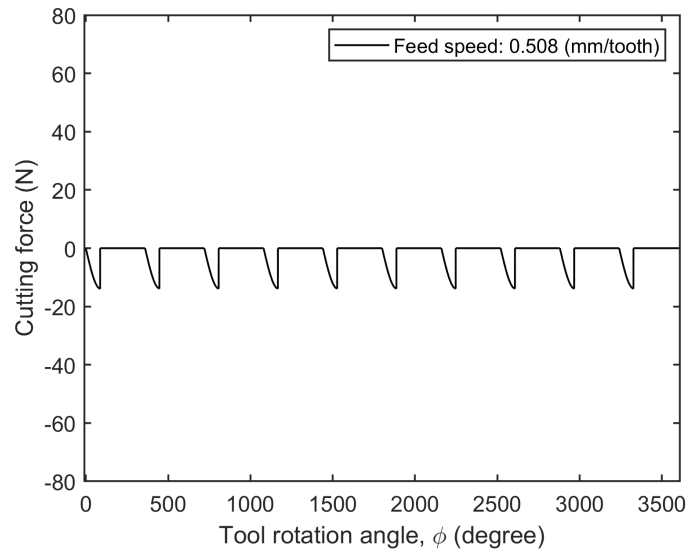


Figure 4.26: Cutting force in the z -direction at feed: 0.508 (mm/tooth) and axial depth-of-cut: 0.15 (mm).

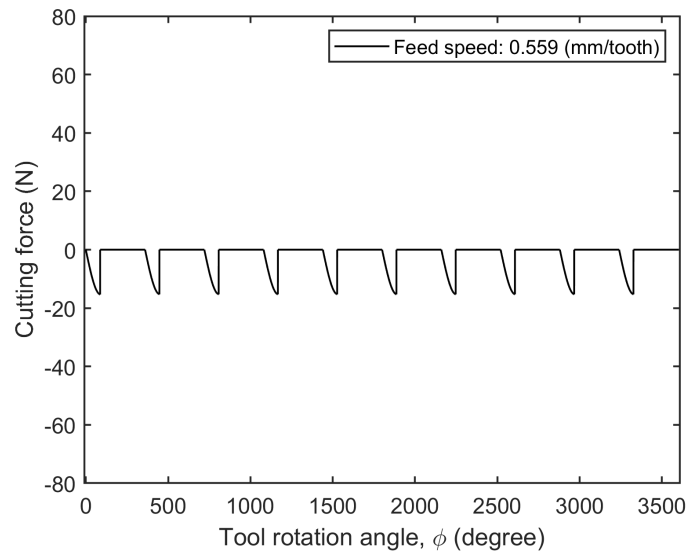


Figure 4.27: Cutting force in the z -direction at feed: 0.559 (mm/tooth) and axial depth-of-cut: 0.15 (mm).

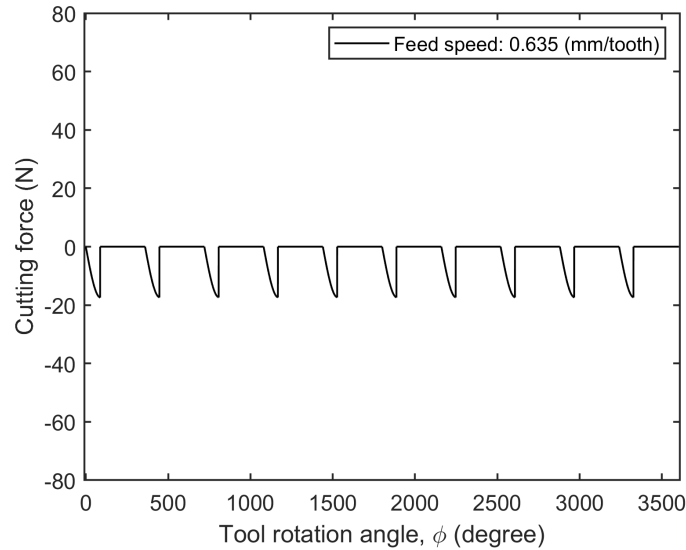


Figure 4.28: Cutting force in the z -direction at feed: 0.635 (mm/tooth) and axial depth-of-cut: 0.15 (mm).

Figures 4.5 through 4.28 show simulated cutting forces with varying feed speeds at an axial depth-of-cut of 0.15 mm. In the first revolution, there were no cutting forces at $87.06 < \phi < 360$ deg because the cutting tool was not interacting within these angles. The cutting forces generated by a tooth caused vibration on the cutter. Thus a wavy profile will be imprinted on the workpiece surface. When a subsequent tooth passed along the alignment of the waves, the cutting tool started the next revolution stably by dissipating all energies derived from cutting forces. Moreover, the cutting forces started at zero and increased toward the end of the cut as the chip thickness increased toward the end of the cut. To verify our model's ability to predict x , y , and z direction forces, and consequently vibration, with different axial depth-of-cuts, we also computed forces and vibrations for axial depth-of-cuts of 1 mm and 5 mm.

Cutting force results with the axial depth-of-cut: 1 mm

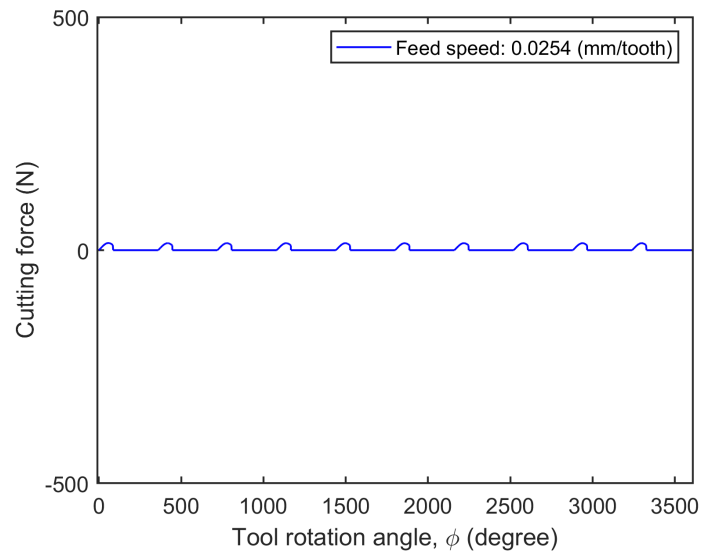


Figure 4.29: Cutting force in the x -direction at feed: 0.0254 (mm/tooth) and axial depth-of-cut: 1 (mm).

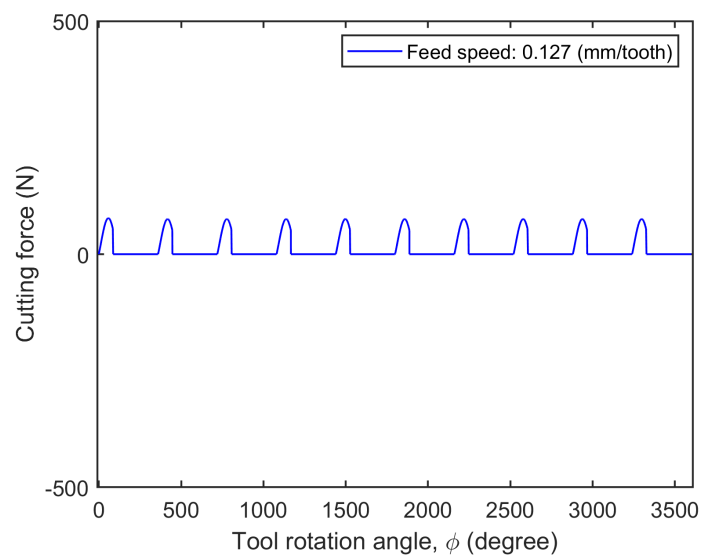


Figure 4.30: Cutting force in the x -direction at feed: 0.127 (mm/tooth) and axial depth-of-cut: 1 (mm).

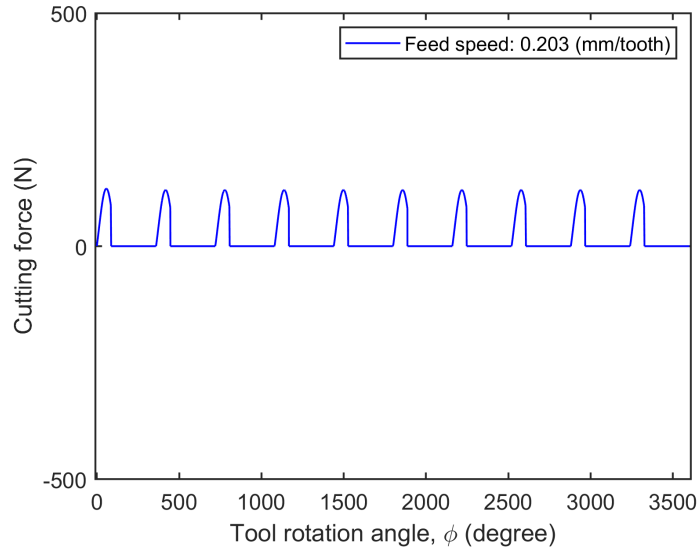


Figure 4.31: Cutting force in the x -direction at feed: 0.203 (mm/tooth) and axial depth-of-cut: 1 (mm).

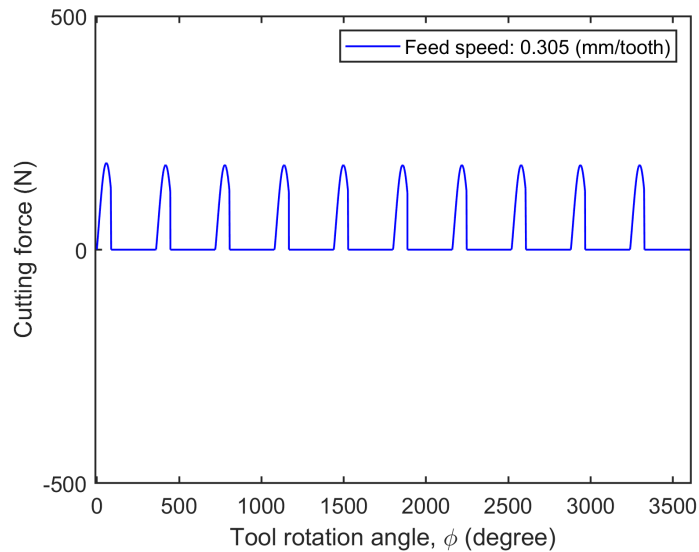


Figure 4.32: Cutting force in the x -direction at feed: 0.305 (mm/tooth) and axial depth-of-cut: 1 (mm).

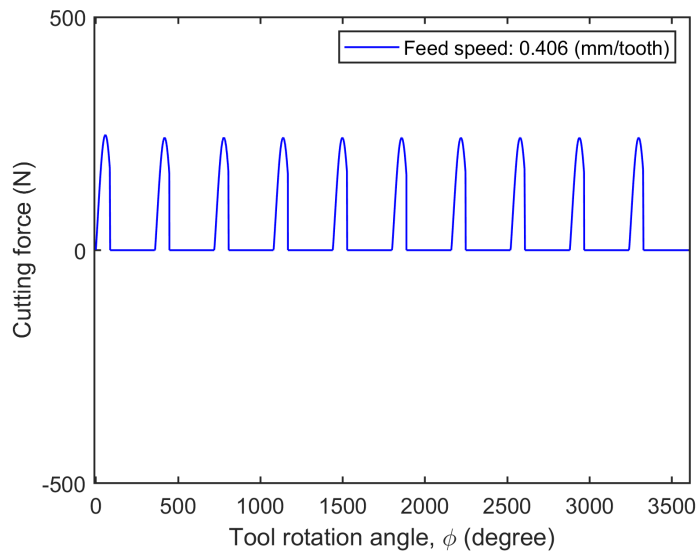


Figure 4.33: Cutting force in the x -direction at feed: 0.406 (mm/tooth) and axial depth-of-cut: 1 (mm).

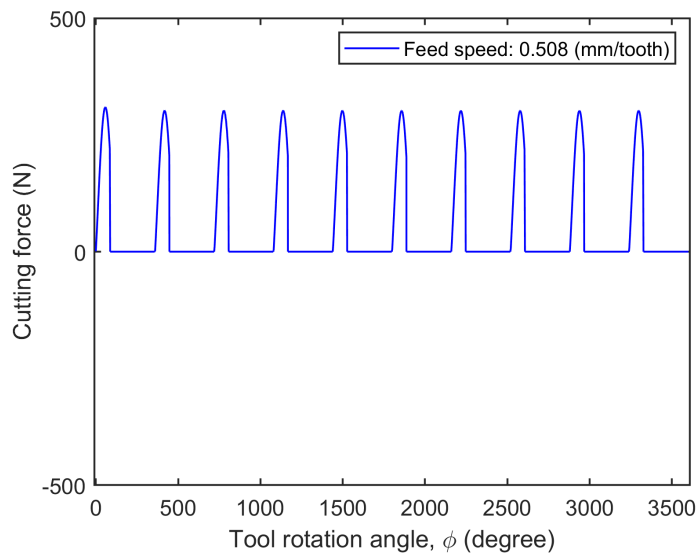


Figure 4.34: Cutting force in the x -direction at feed: 0.508 (mm/tooth) and axial depth-of-cut: 1 (mm).

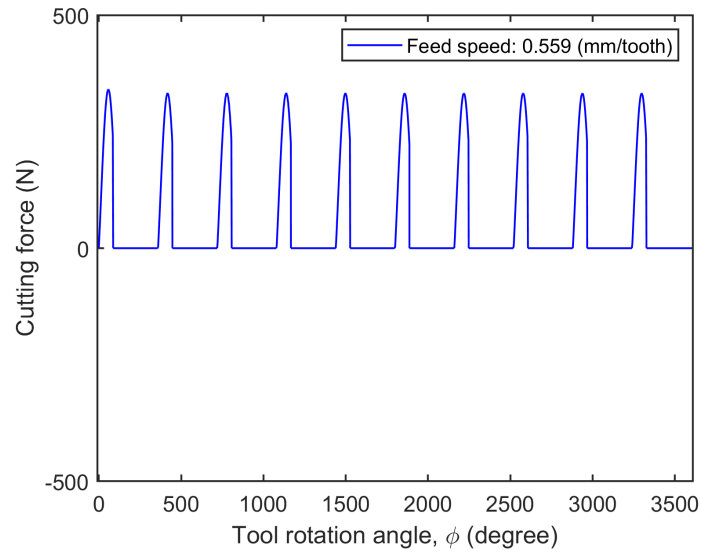


Figure 4.35: Cutting force in the x -direction at feed: 0.559 (mm/tooth) and axial depth-of-cut: 1 (mm).

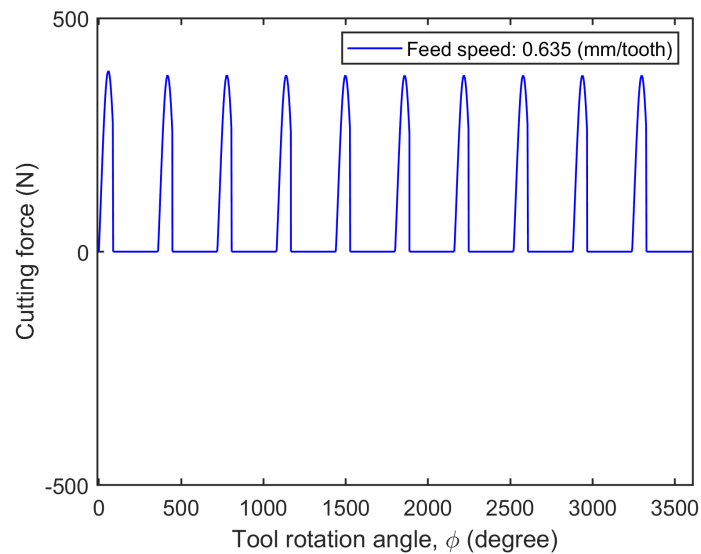


Figure 4.36: Cutting force in the x -direction at feed: 0.635 (mm/tooth) and axial depth-of-cut: 1 (mm).

Cutting force in the y -direction

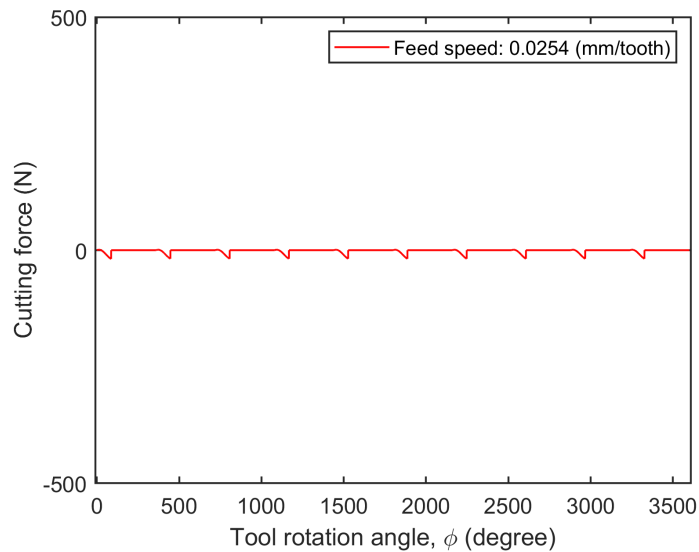


Figure 4.37: Cutting force in the y -direction at feed: 0.0254 (mm/tooth) and axial depth-of-cut: 1 (mm).

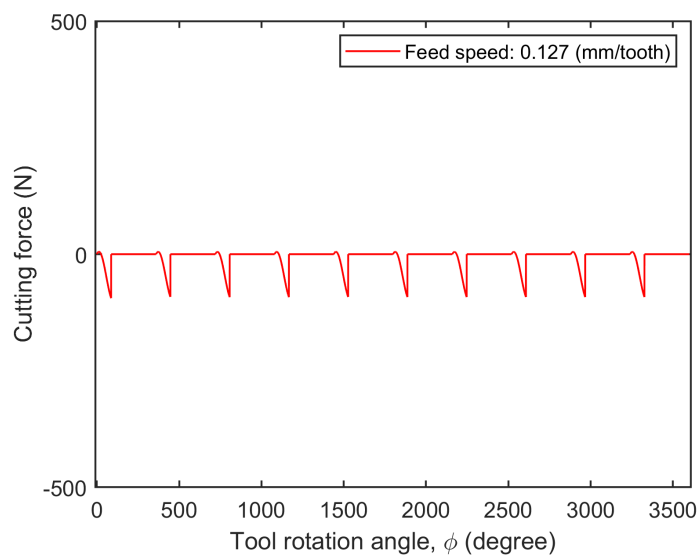


Figure 4.38: Cutting force in the y -direction at feed: 0.127 (mm/tooth) and axial depth-of-cut: 1 (mm).

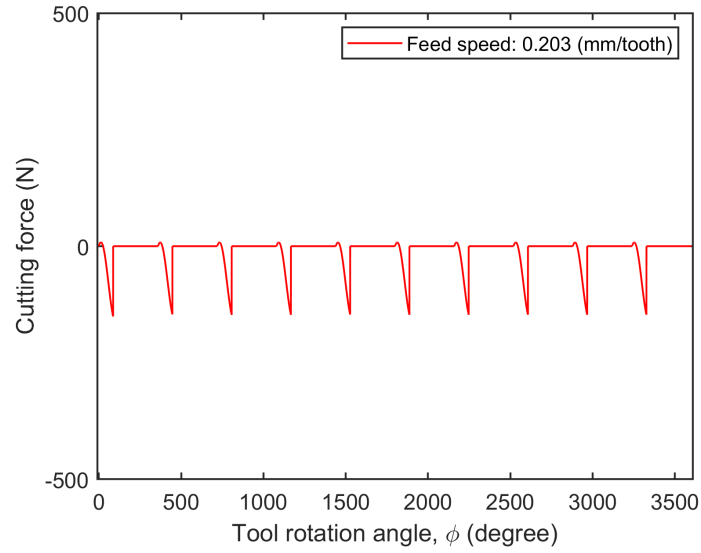


Figure 4.39: Cutting force in the y -direction at feed: 0.203 (mm/tooth) and axial depth-of-cut: 1 (mm).

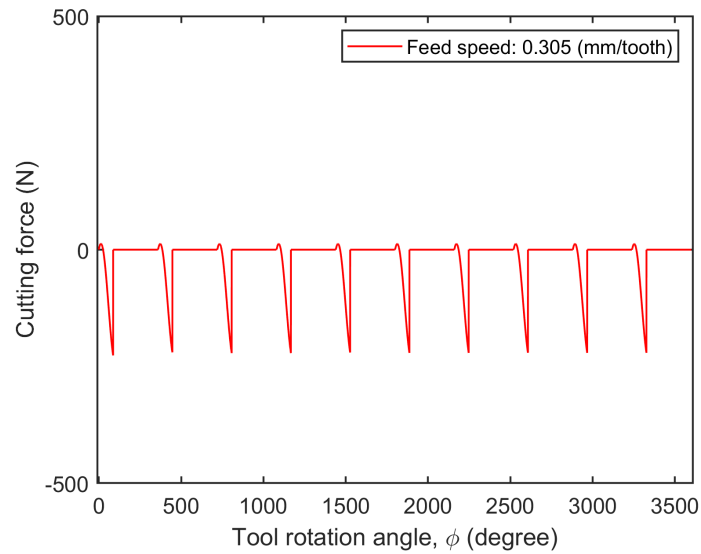


Figure 4.40: Cutting force in the y -direction at feed: 0.305 (mm/tooth) and axial depth-of-cut: 1 (mm).

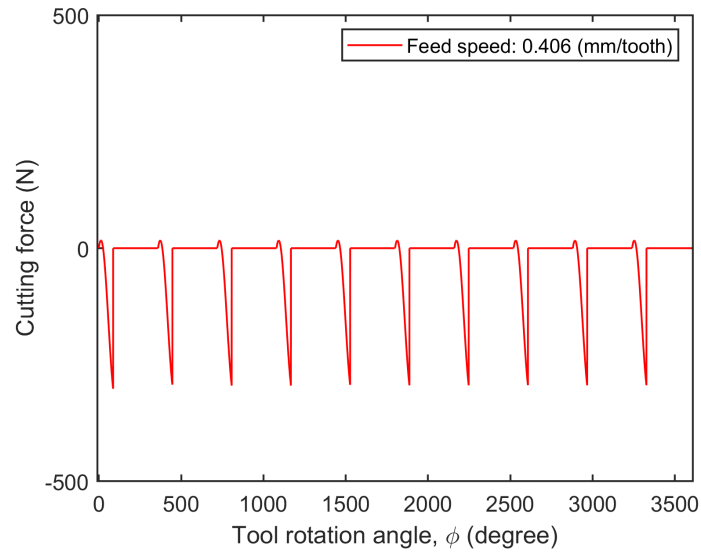


Figure 4.41: Cutting force in the y -direction at feed: 0.406 (mm/tooth) and axial depth-of-cut: 1 (mm).

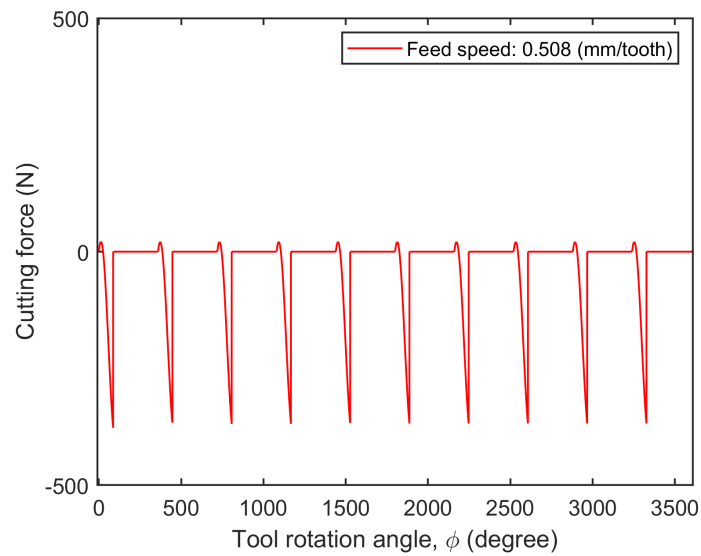


Figure 4.42: Cutting force in the y -direction at feed: 0.508 (mm/tooth) and axial depth-of-cut: 1 (mm).

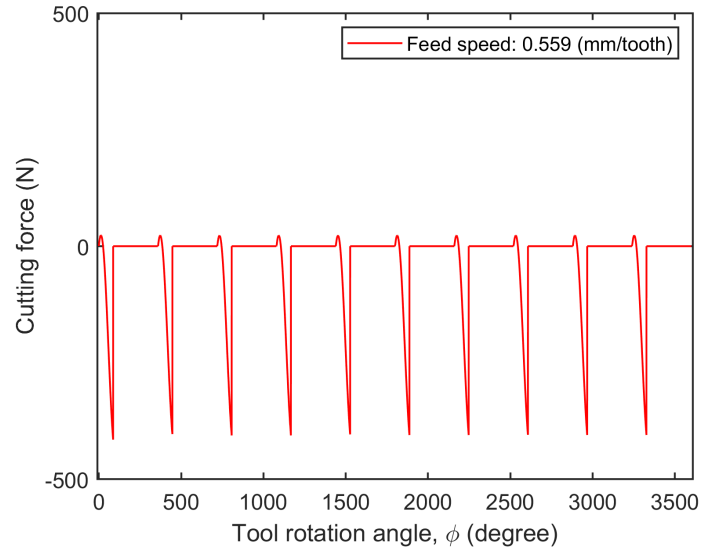


Figure 4.43: Cutting force in the y -direction at feed: 0.559 (mm/tooth) and axial depth-of-cut: 1 (mm).

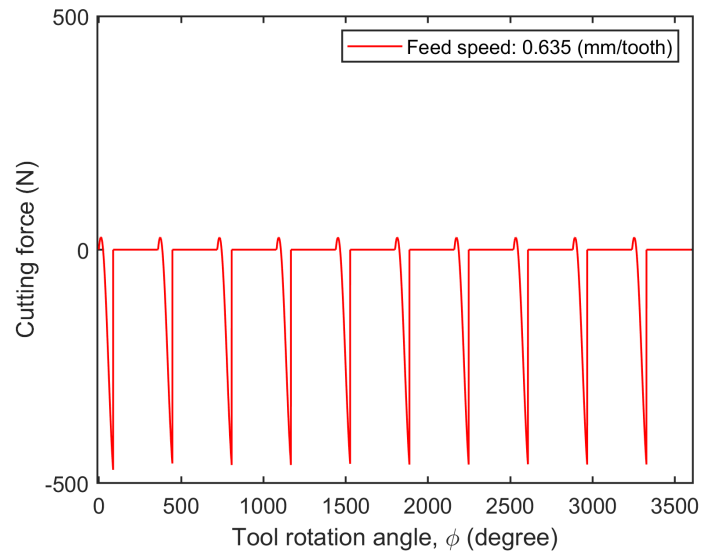


Figure 4.44: Cutting force in the y -direction at feed: 0.635 (mm/tooth) and axial depth-of-cut: 1 (mm).

Cutting force in the z -direction

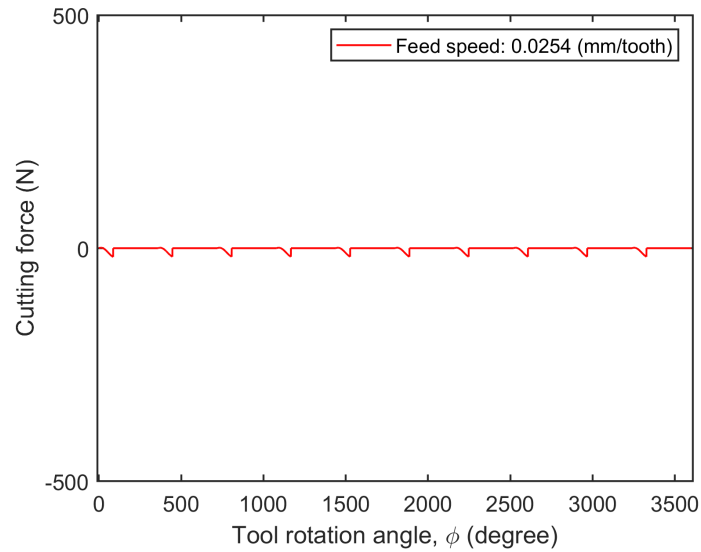


Figure 4.45: Cutting force in the z -direction at feed: 0.0254 (mm/tooth) and axial depth-of-cut: 1 (mm).

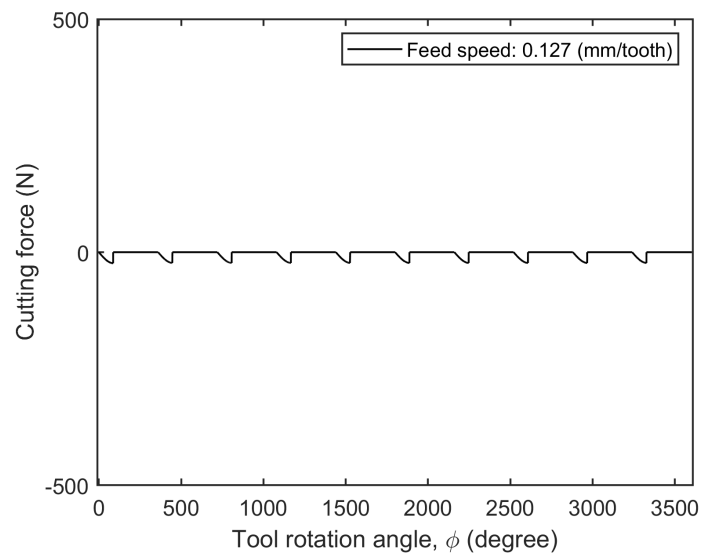


Figure 4.46: Cutting force in the z -direction at feed: 0.127 (mm/tooth) and axial depth-of-cut: 1 (mm).

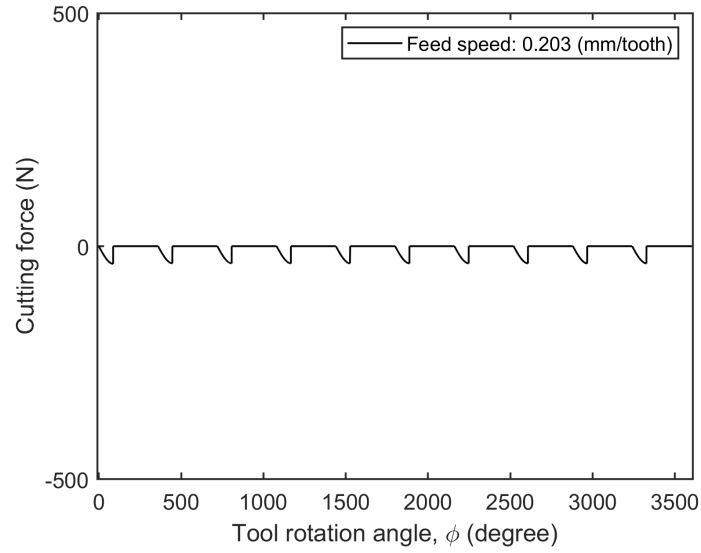


Figure 4.47: Cutting force in the z -direction at feed: 0.203 (mm/tooth) and axial depth-of-cut: 1 (mm).

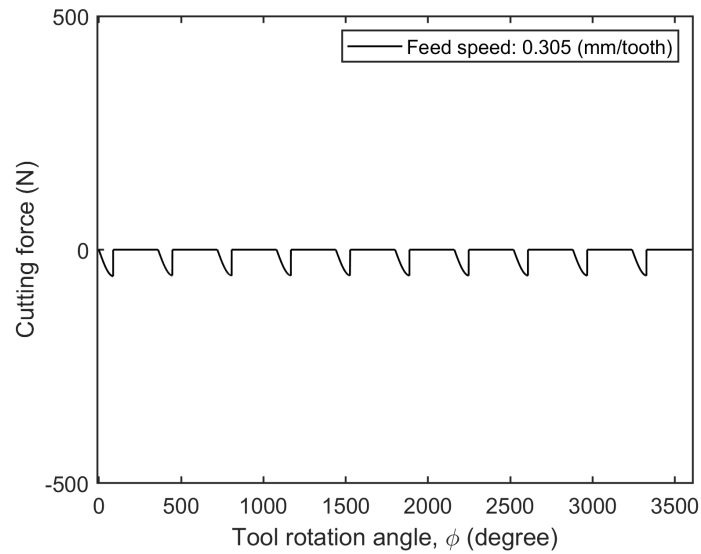


Figure 4.48: Cutting force in the z -direction at feed: 0.305 (mm/tooth) and axial depth-of-cut: 1 (mm).

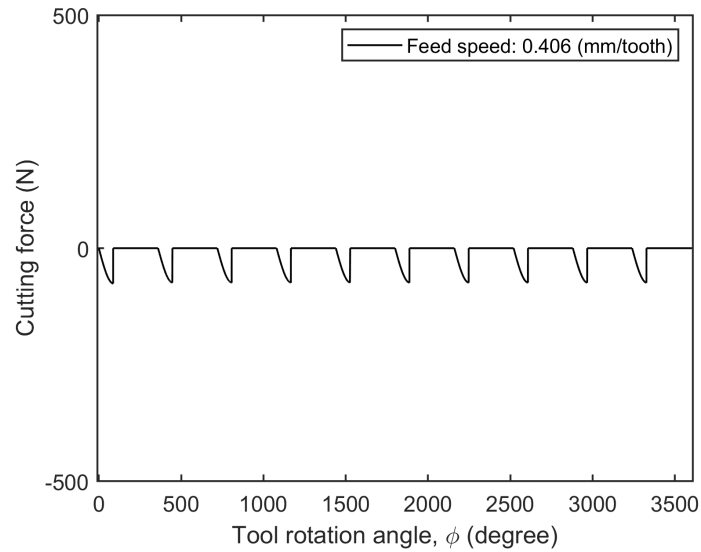


Figure 4.49: Cutting force in the z -direction at feed: 0.406 (mm/tooth) and axial depth-of-cut: 1 (mm).

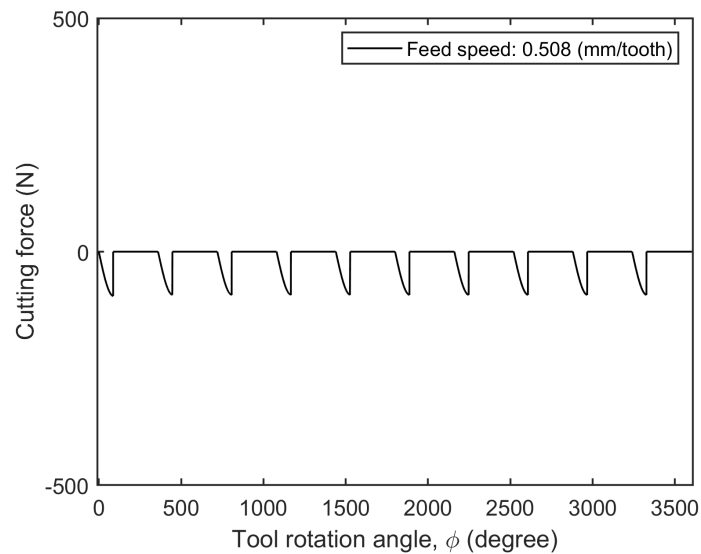


Figure 4.50: Cutting force in the z -direction at feed: 0.508 (mm/tooth) and axial depth-of-cut: 1 (mm).

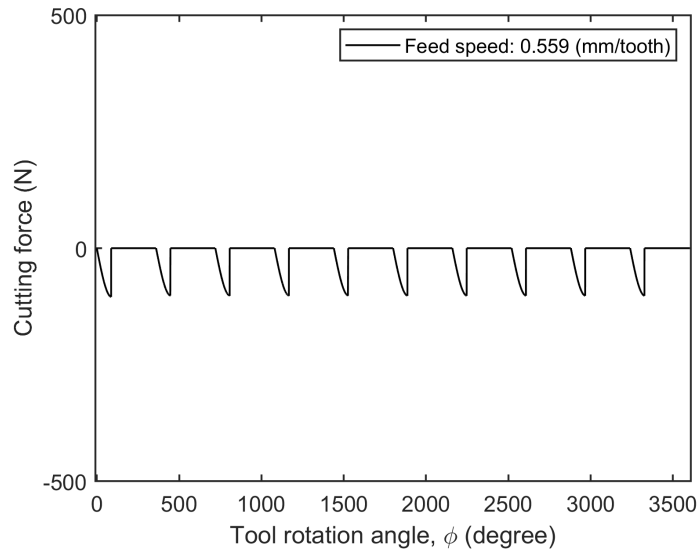


Figure 4.51: Cutting force in the z -direction at feed: 0.559 (mm/tooth) and axial depth-of-cut: 1 (mm).

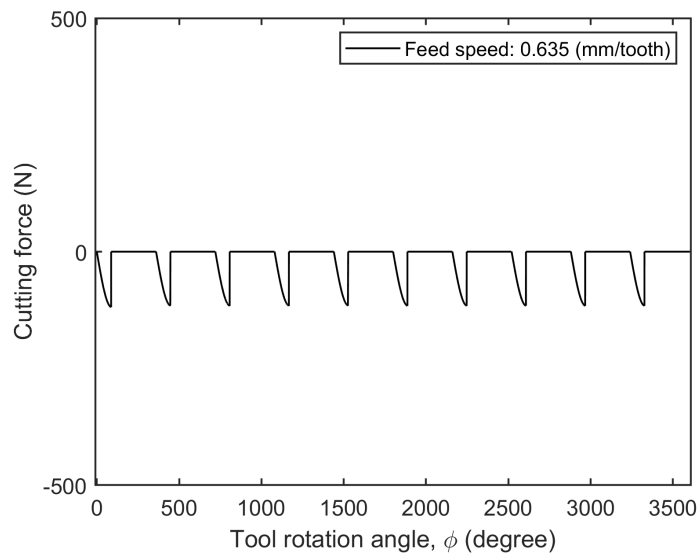


Figure 4.52: Cutting force in the z -direction at feed: 0.635 (mm/tooth) and axial depth-of-cut: 1 (mm).

Figures 4.29 through 4.52 show the cutting forces in the x , y , and z directions for an axial depth-of-cut of 1 mm. As expected, the cutting tool started interacting with the workpiece at 0 degrees and finished at 87.06 degrees, and the maximum cutting forces in the x , y , and z directions increased linearly with increasing feed speeds. Furthermore, an increase in the axial depth-of-cut increased the chip thickness, resulting in higher cutting forces.

Cutting force results with the axial depth-of-cut: 5 mm

Similarly, we computed the cutting forces with an axial depth-of-cut of 5 mm to verify the correlation between the difference in axial depth-of-cuts. Figures 4.53 through 4.76 present the results obtained from the milling simulation with an axial depth-of-cut of 5 mm. For the simulation with the axial depth-of-cut of 5mm, 100 revolutions were used since the cutting process was unstable, whereas 10 revolutions were considered in the simulations with axial depth-of-cuts of 0.15 mm and 1 mm.

Cutting force in the x -direction

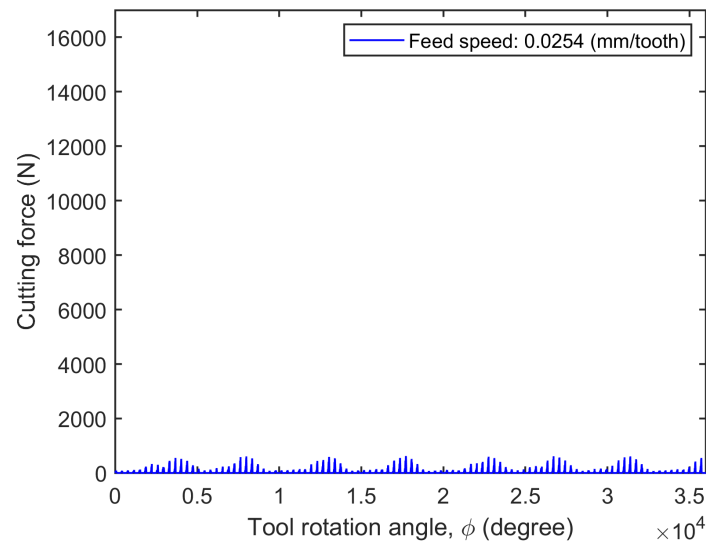


Figure 4.53: Cutting force in the x -direction at feed: 0.0254 (mm/tooth) and axial depth-of-cut: 5 (mm).

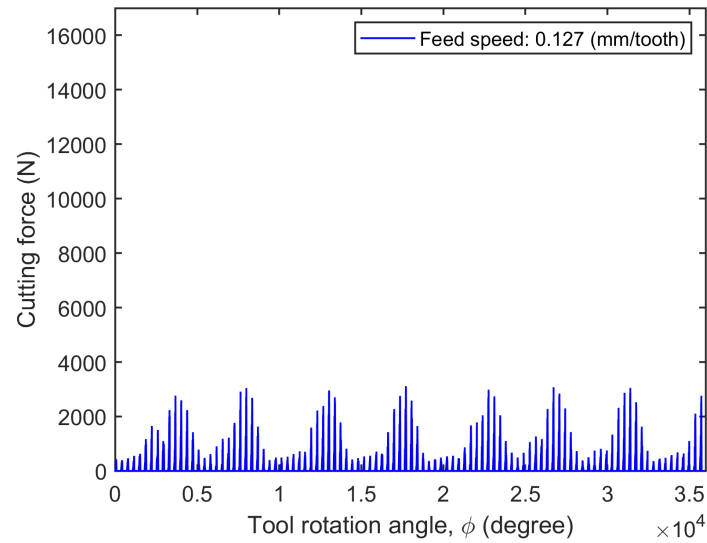


Figure 4.54: Cutting force in the x -direction at feed: 0.127 (mm/tooth) and axial depth-of-cut: 5 (mm).

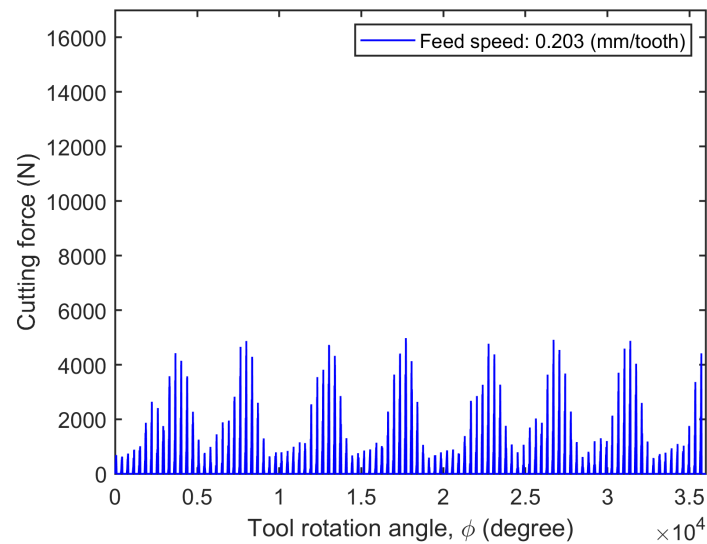


Figure 4.55: Cutting force in the x -direction at feed: 0.203 (mm/tooth) and axial depth-of-cut: 5 (mm).

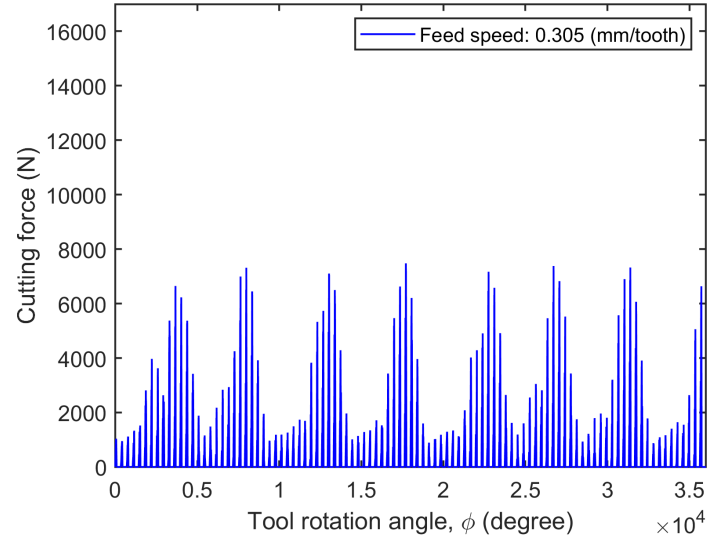


Figure 4.56: Cutting force in the x -direction at feed: 0.305 (mm/tooth) and axial depth-of-cut: 5 (mm).

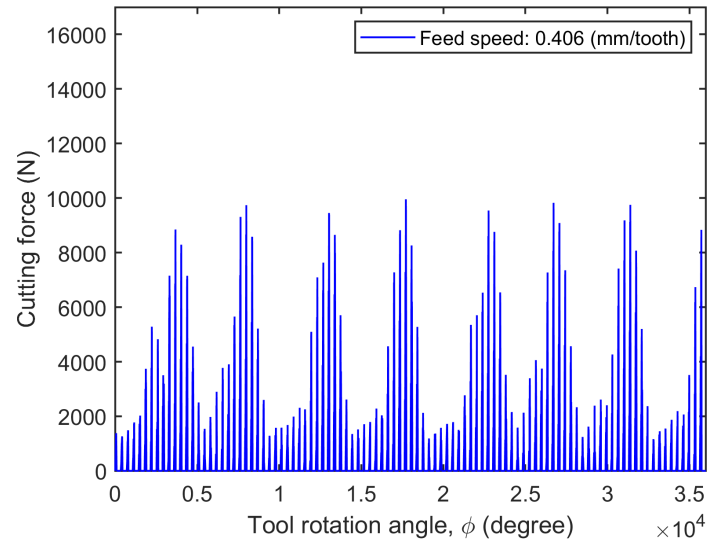


Figure 4.57: Cutting force in the x -direction at feed: 0.406 (mm/tooth) and axial depth-of-cut: 5 (mm).

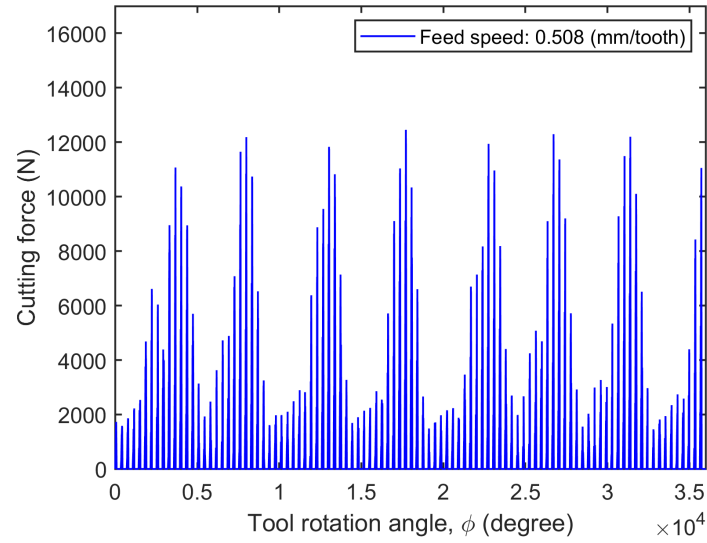


Figure 4.58: Cutting force in the x -direction at feed: 0.508 (mm/tooth) and axial depth-of-cut: 5 (mm).

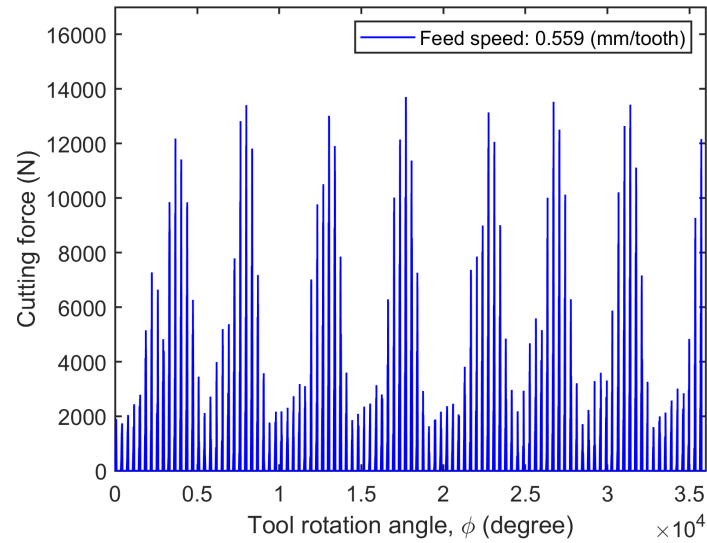


Figure 4.59: Cutting force in the x -direction at feed: 0.559 (mm/tooth) and axial depth-of-cut: 5 (mm).

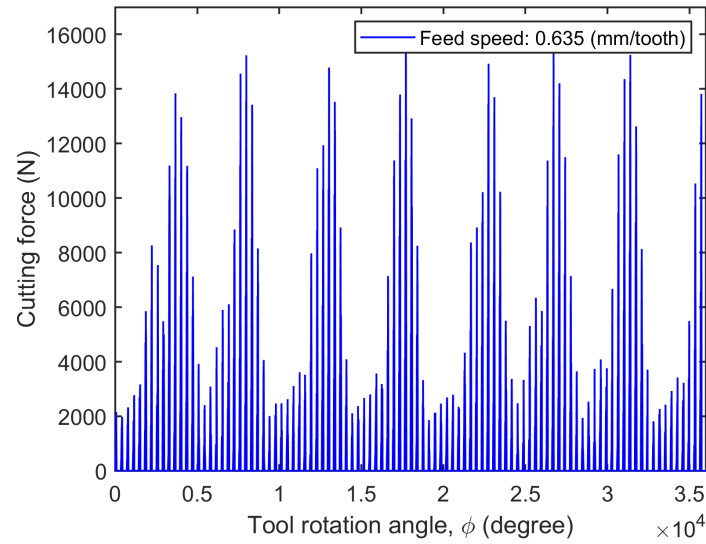


Figure 4.60: Cutting force in the x -direction at feed: 0.635 (mm/tooth) and axial depth-of-cut: 5 (mm).

Cutting force in the y -direction

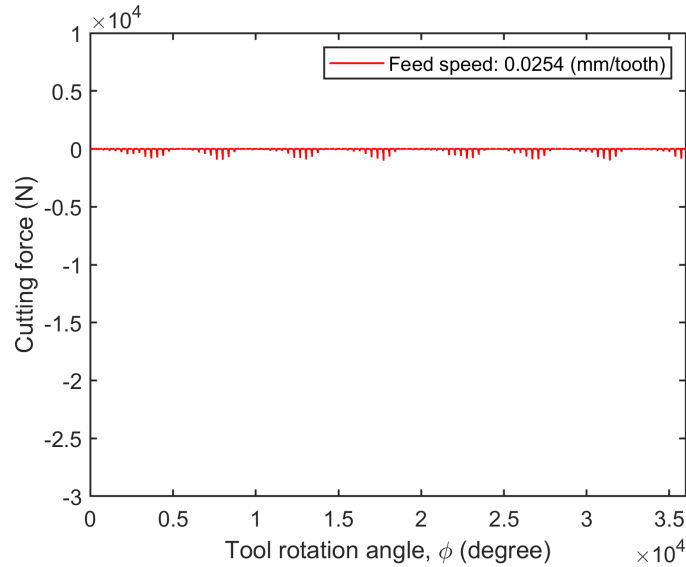


Figure 4.61: Cutting force in the y -direction at feed: 0.0254 (mm/tooth) and axial depth-of-cut: 5 (mm).

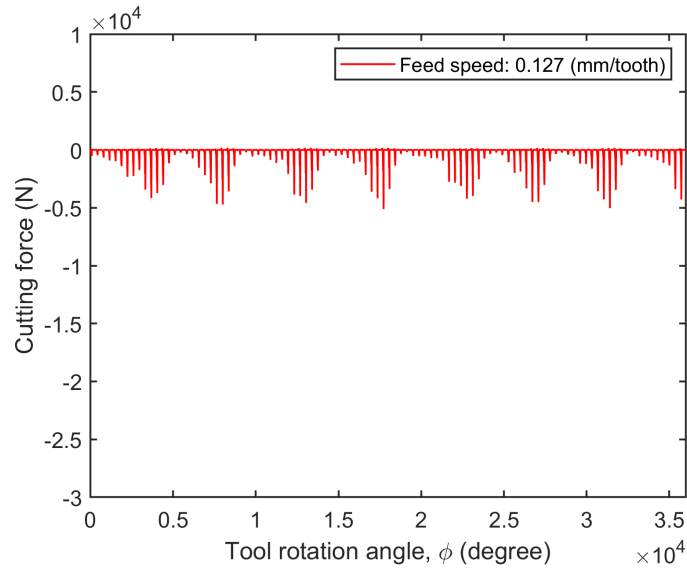


Figure 4.62: Cutting force in the y -direction at feed: 0.127 (mm/tooth) and axial depth-of-cut: 5 (mm).

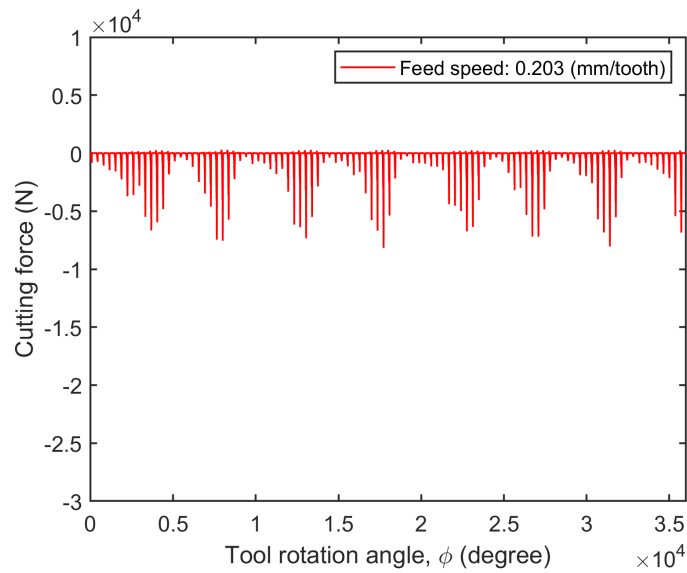


Figure 4.63: Cutting force in the y -direction at feed: 0.203 (mm/tooth) and axial depth-of-cut: 5 (mm).

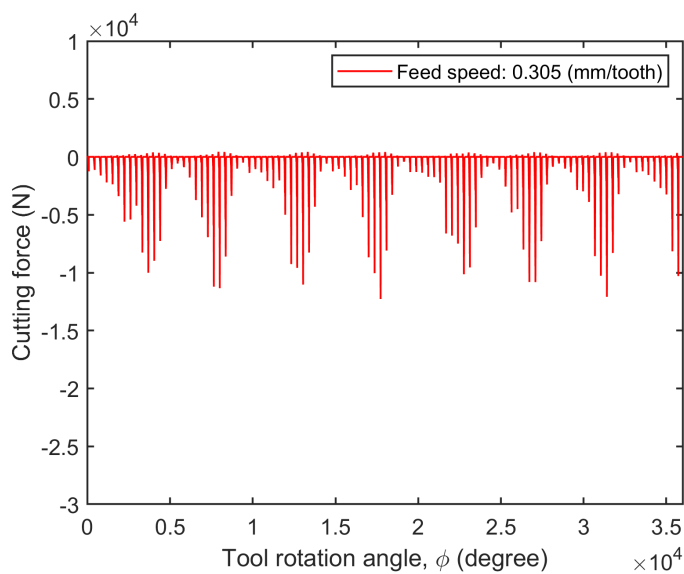


Figure 4.64: Cutting force in the y -direction at feed: 0.305 (mm/tooth) and axial depth-of-cut: 5 (mm).

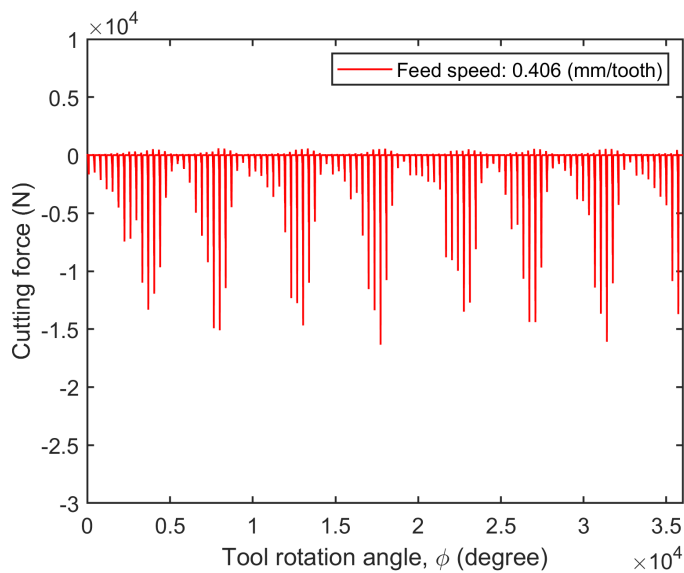


Figure 4.65: Cutting force in the y -direction at feed: 0.406 (mm/tooth) and axial depth-of-cut: 5 (mm).

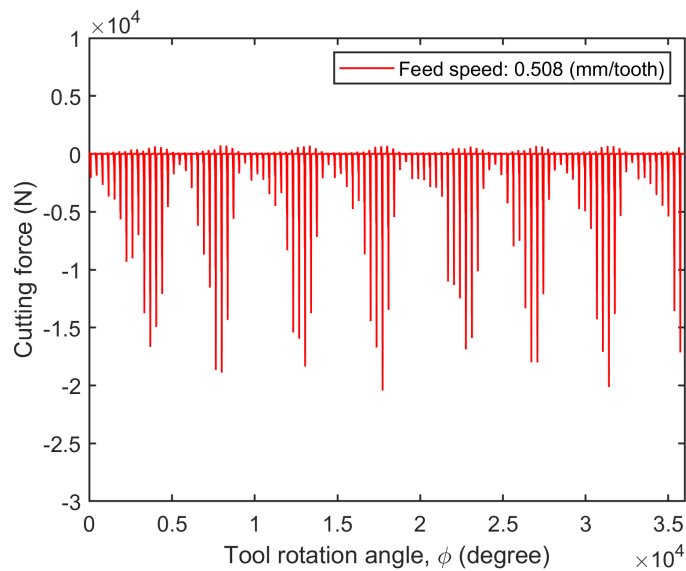


Figure 4.66: Cutting force in the y -direction at feed: 0.508 (mm/tooth) and axial depth-of-cut: 5 (mm).

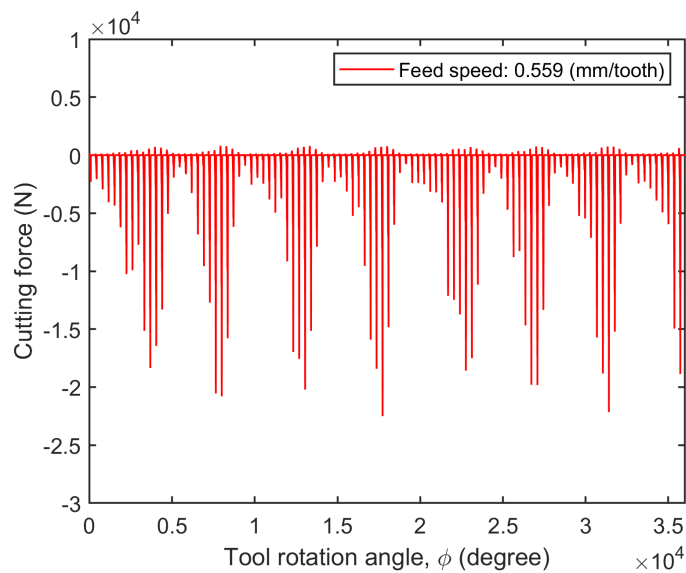


Figure 4.67: Cutting force in the y -direction at feed: 0.559 (mm/tooth) and axial depth-of-cut: 5 (mm).

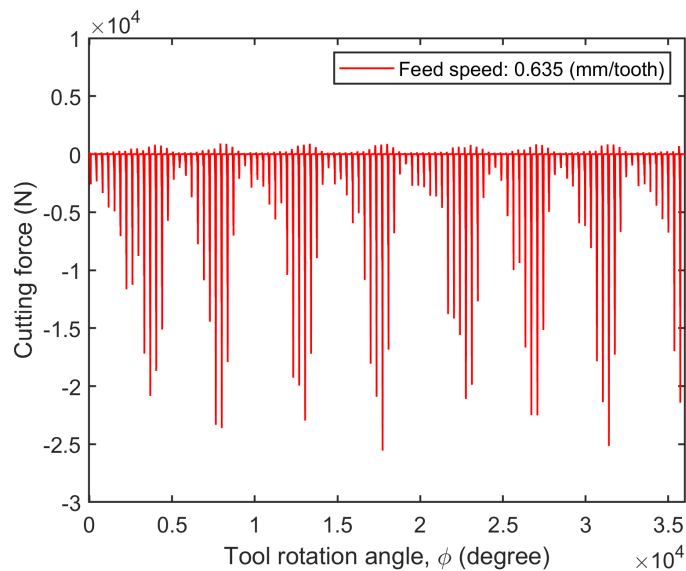


Figure 4.68: Cutting force in the y -direction at feed: 0.635 (mm/tooth) and axial depth-of-cut: 5 (mm).

Cutting force in the z -direction

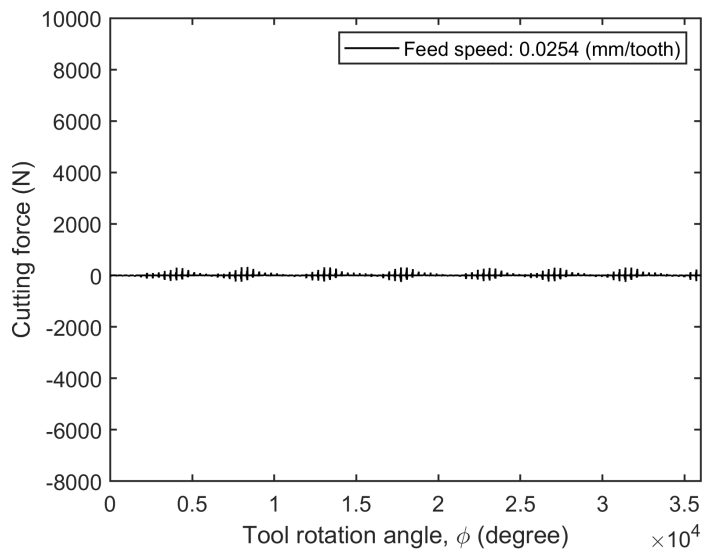


Figure 4.69: Cutting force in the z -direction at feed: 0.0254 (mm/tooth) and axial depth-of-cut: 5 (mm).

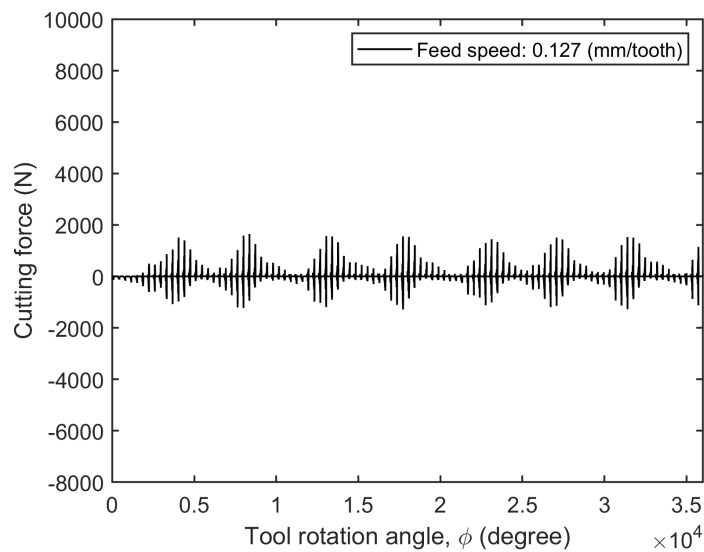


Figure 4.70: Cutting force in the z -direction at feed: 0.127 (mm/tooth) and axial depth-of-cut: 5 (mm).

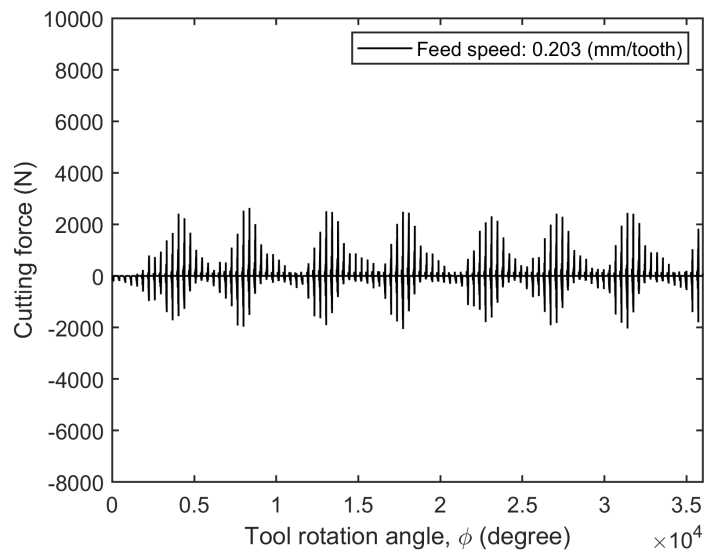


Figure 4.71: Cutting force in the z -direction at feed: 0.203 (mm/tooth) and axial depth-of-cut: 5 (mm).

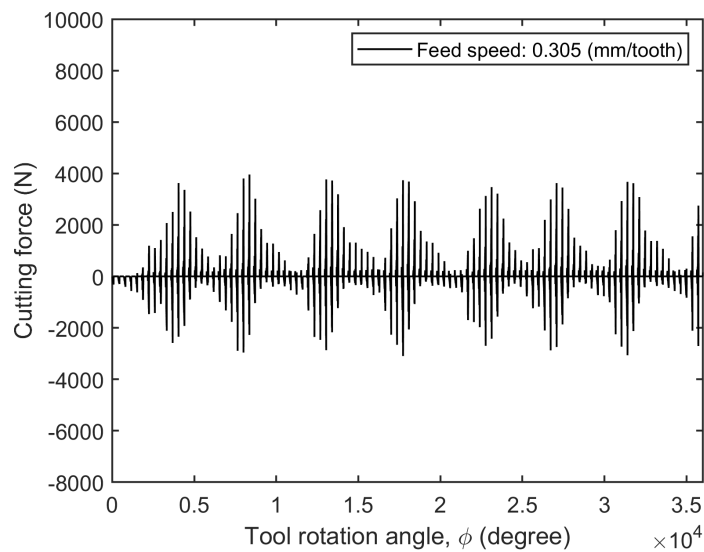


Figure 4.72: Cutting force in the z -direction at feed: 0.305 (mm/tooth) and axial depth-of-cut: 5 (mm).

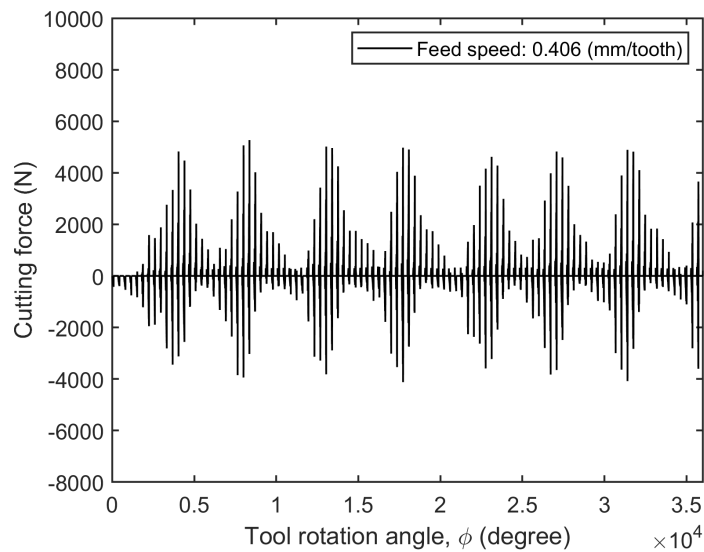


Figure 4.73: Cutting force in the z -direction at feed: 0.406 (mm/tooth) and axial depth-of-cut: 5 (mm).

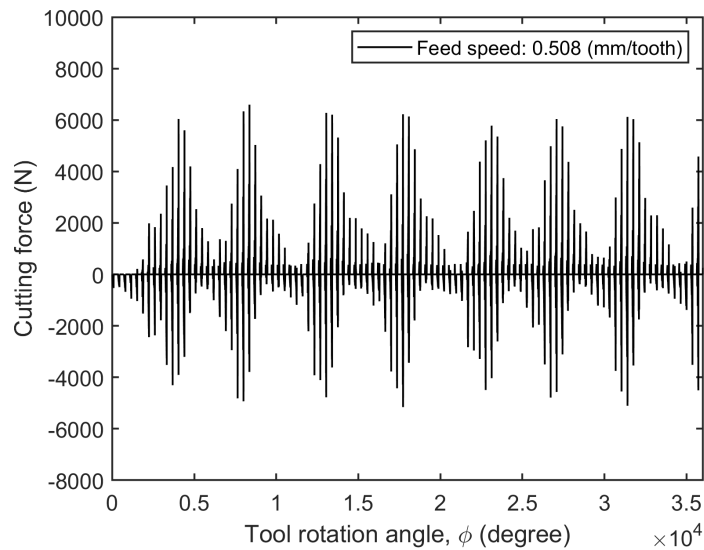


Figure 4.74: Cutting force in the z -direction at feed: 0.508 (mm/tooth) and axial depth-of-cut: 5 (mm).

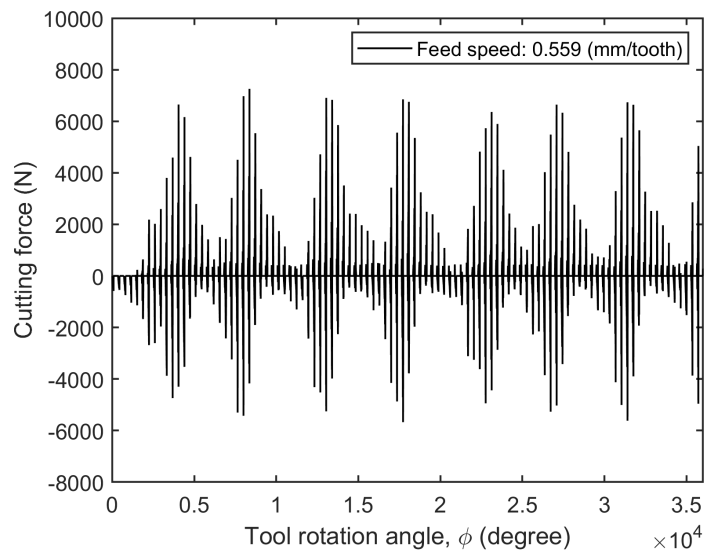


Figure 4.75: Cutting force in the z -direction at feed: 0.559 (mm/tooth) and axial depth-of-cut: 5 (mm).

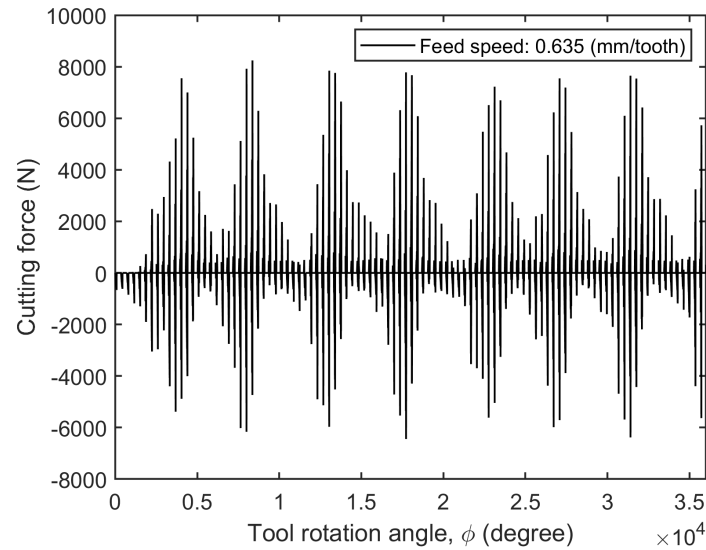


Figure 4.76: Cutting force in the z -direction at feed: 0.635 (mm/tooth) and axial depth-of-cut: 5 (mm).

Similarly, figures 4.53 through 4.76 show the cutting forces in the x , y , and z directions with an axial depth-of-cut of 5 mm. When a subsequent tooth passed along the alignment of the waves, it caused unstable cutting due to increasing or decreasing vibration. Therefore, the Fast Fourier Transform was applied to the cutting force in the x , y , and z directions to investigate the stability of the cutting process, and the results are presented in Appendix D. It was found that the cutting processes were unstable as the primary tooth passing frequency was close to the system's natural frequency.

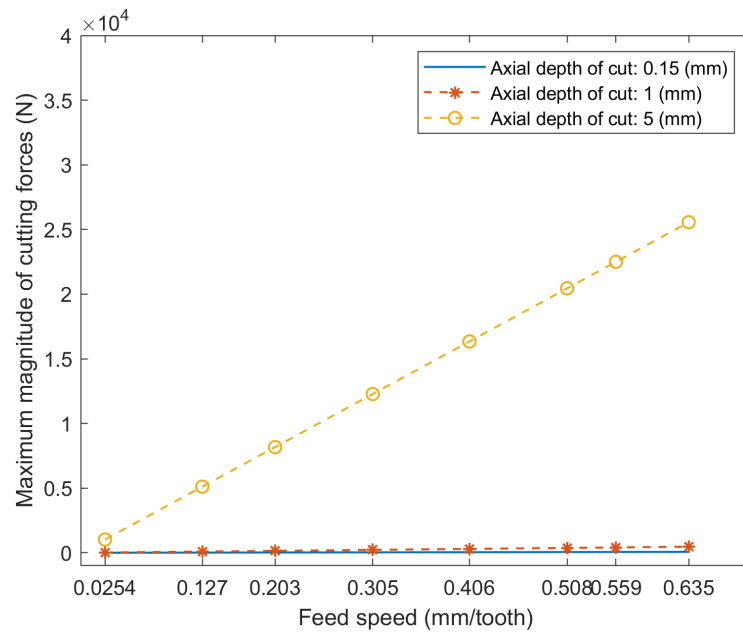


Figure 4.77: Computed maximum cutting forces in the y -direction with three axial depth-of-cuts.

It is noteworthy that a higher axial depth-of-cut caused fluctuations in the cutting forces that were not observed at depth-of-cuts of 0.15 and 1 mm. When comparing the three axial depth-of-cuts, it was observed that the maximum cutting forces in the y -direction changed significantly since the y -direction is the direction of action of the main cutting force. Moreover, the tool experienced the maximum feed resistance in the y -direction during the cutting process.

Figure 4.77 compares the maximum magnitude of cutting force in the y -direction at various feed rates. An increase in axial depth-of-cut resulted in a linear increase in the maximum magnitude of cutting force because axial depth-of-cut, b , has a linear effect on a cutting force, as shown in Equations (2.7) and (2.8). Furthermore, the

maximum cutting forces increased with an increase in the feed per tooth since the cutting force equations are based on the shear force on the flank surface of the cutting edge.

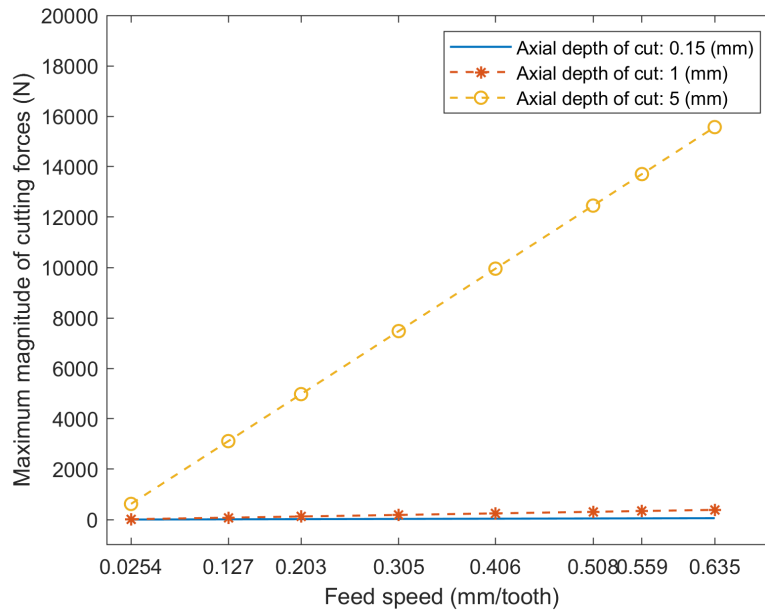


Figure 4.78: Computed maximum cutting force in the x -direction with three axial depth-of-cuts.

Similarly, figure 4.78 compares the maximum magnitude of cutting force in the x -direction at various feed speeds. The maximum cutting forces in the comparison of three axial depth-of-cuts were linearly increased with increasing feeds. This was due to the fact that increases in feed speeds and axial depth-of-cut increased the area of contact between the tool and the workpiece.

Figure 4.79 shows the maximum magnitude of cutting forces in the z -direction. The maximum cutting forces in the z -direction were relatively smaller than the max-

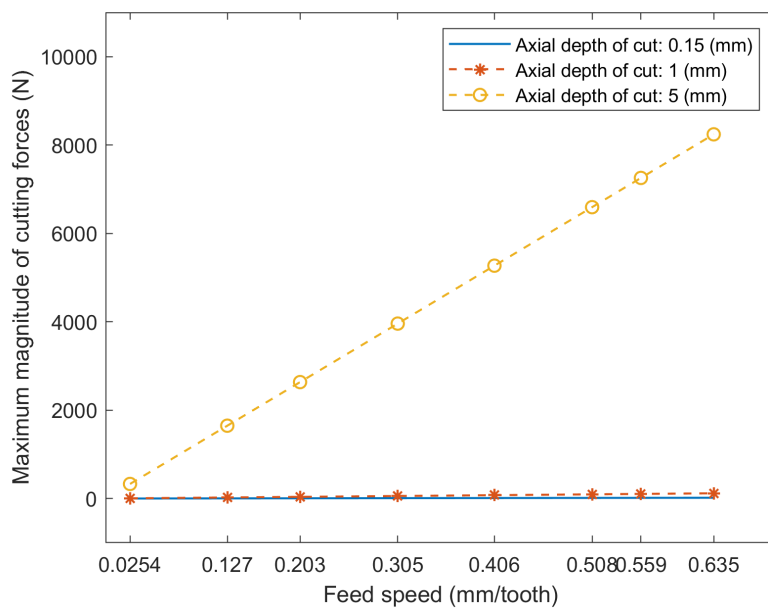


Figure 4.79: Computed maximum cutting force in the z -direction with three axial depth-of-cuts.

imum cutting forces in the x and y directions since the cutting force coefficient in the z -direction was smaller than coefficients in the x and y directions.

Vibration results in milling process

Tool vibration results with the axial depth-of-cut: 0.15 mm

The tool's vibrations, caused by cutting forces, were obtained by solving the equations of motion, Eq.(2.20) with the Newmark method. While the cutting forces were computed with varying feed speeds in three axial depth-of-cuts, tool vibrations were computed, as well. The vibrations in the x , y , and z directions are shown in Figures 4.80 to 4.103 when an axial depth-of-cut is 0.15 mm. The first revolution of the cutting process started at 0 degree and finished at 87.06 degree because the radial depth-of-cut was 50 mm when the tool diameter was 105.4 mm.

Tool displacement in the x -direction

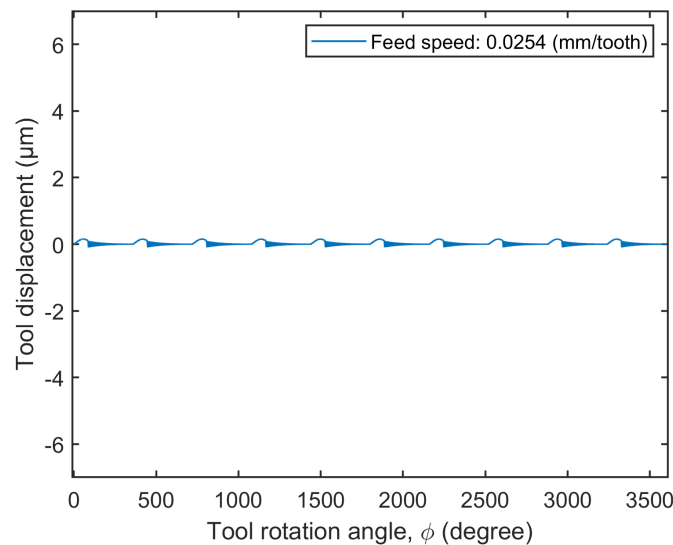


Figure 4.80: Tool displacement in the x -direction at feed: 0.0254 (mm/tooth) and axial depth-of-cut: 0.15 (mm).

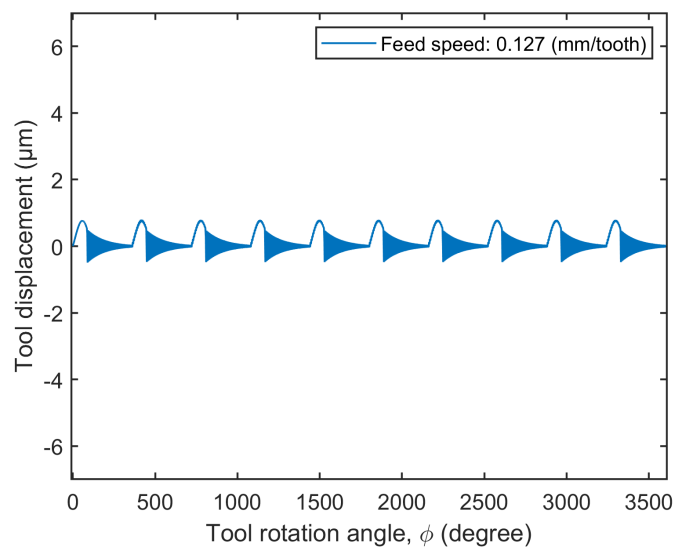


Figure 4.81: Tool displacement in the x -direction at feed: 0.127 (mm/tooth) and axial depth-of-cut: 0.15 (mm).

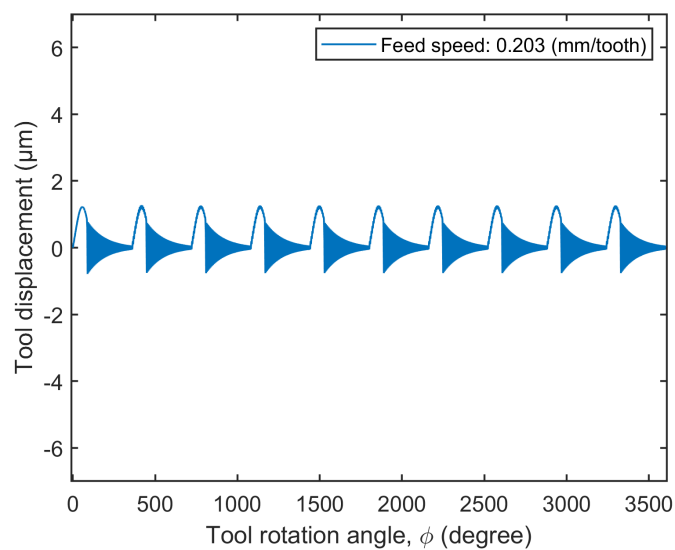


Figure 4.82: Tool displacement in the x -direction at feed: 0.203 (mm/tooth) and axial depth-of-cut: 0.15 (mm).

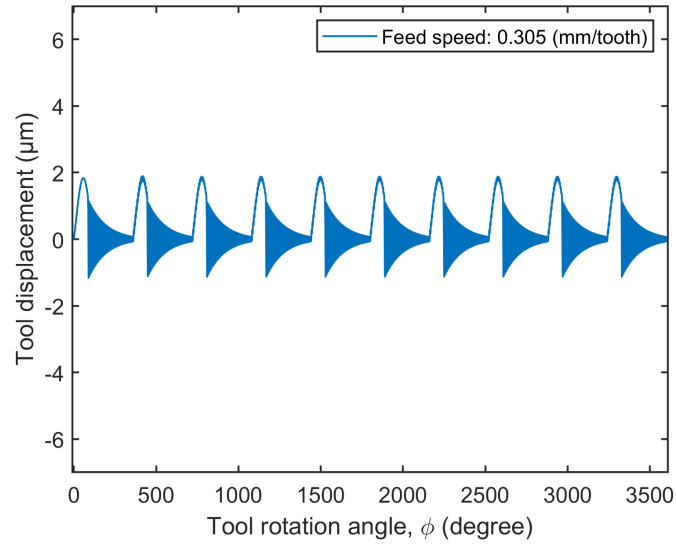


Figure 4.83: Tool displacement in the x -direction at feed: 0.305 (mm/tooth) and axial depth-of-cut: 0.15 (mm).

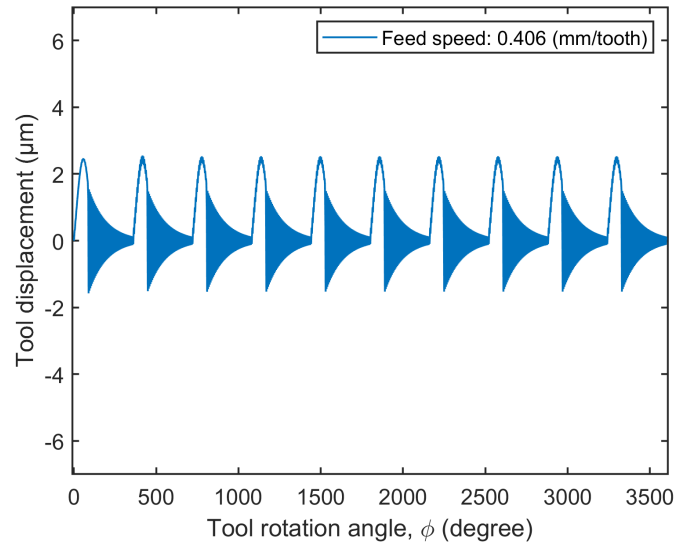


Figure 4.84: Tool displacement in the x -direction at feed: 0.406 (mm/tooth) and axial depth-of-cut: 0.15 (mm).

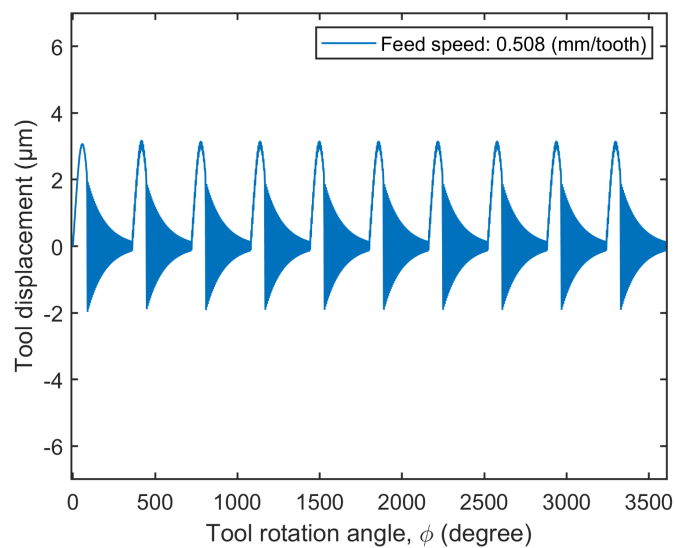


Figure 4.85: Tool displacement in the x -direction at feed: 0.508 (mm/tooth) and axial depth-of-cut: 0.15 (mm).

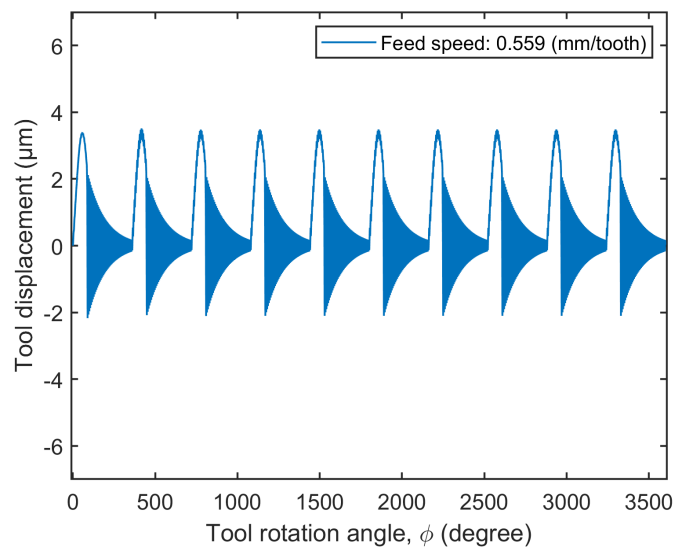


Figure 4.86: Tool displacement in the x -direction at feed: 0.559 (mm/tooth) and axial depth-of-cut: 0.15 (mm).

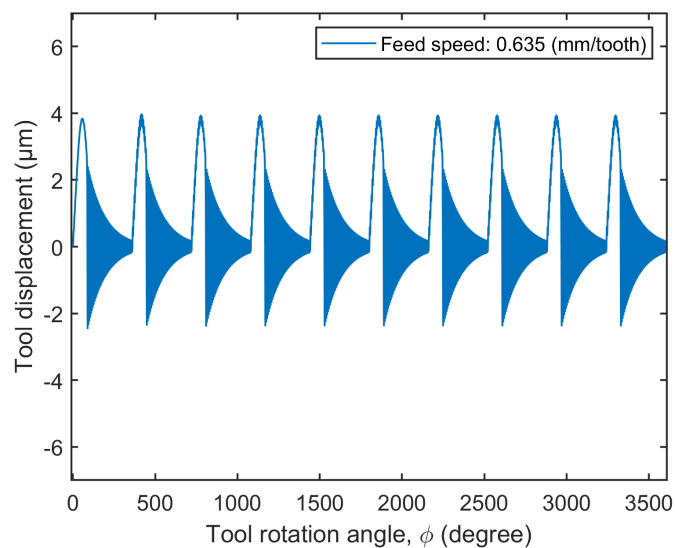


Figure 4.87: Tool displacement in the x -direction at feed: 0.635 (mm/tooth) and axial depth-of-cut: 0.15 (mm).

Tool displacement in the y -direction

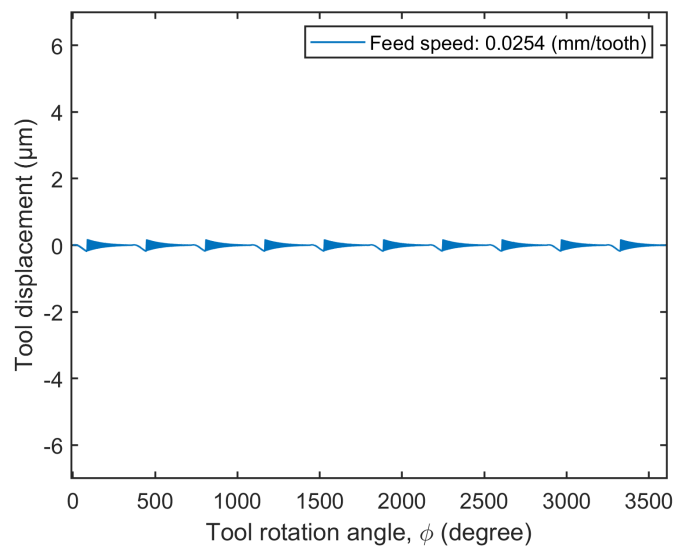


Figure 4.88: Tool displacement in the y -direction at feed: 0.0254 (mm/tooth) and axial depth-of-cut: 0.15 (mm).

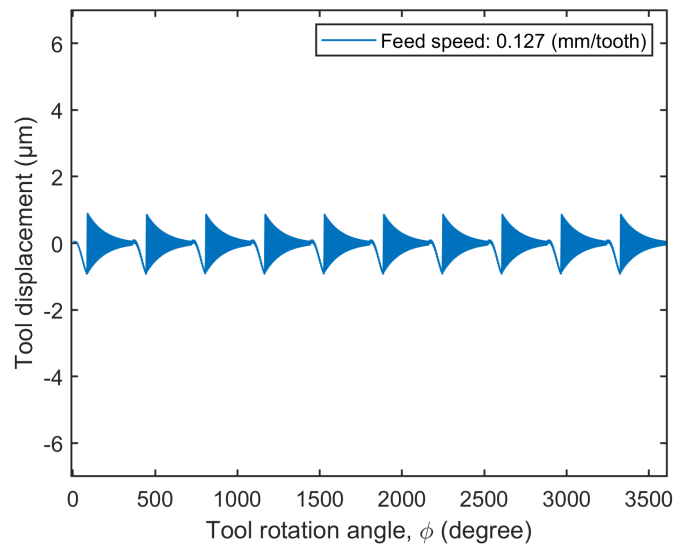


Figure 4.89: Tool displacement in the y -direction at feed: 0.127 (mm/tooth) and axial depth-of-cut: 0.15 (mm).

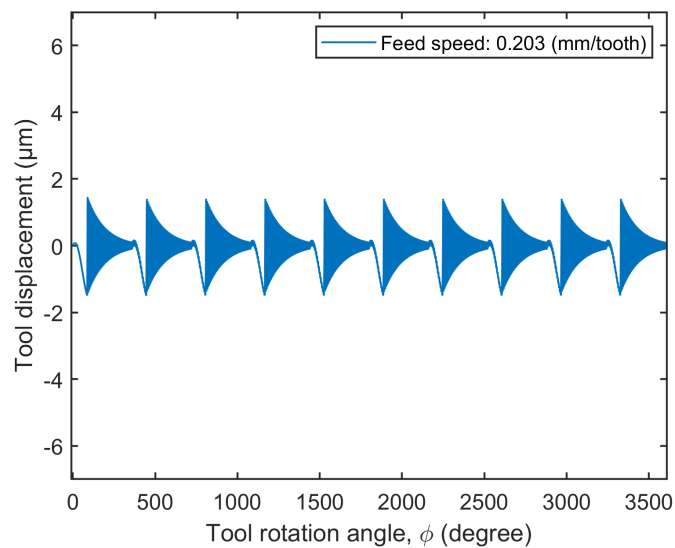


Figure 4.90: Tool displacement in the y -direction at feed: 0.203 (mm/tooth) and axial depth-of-cut: 0.15 (mm).

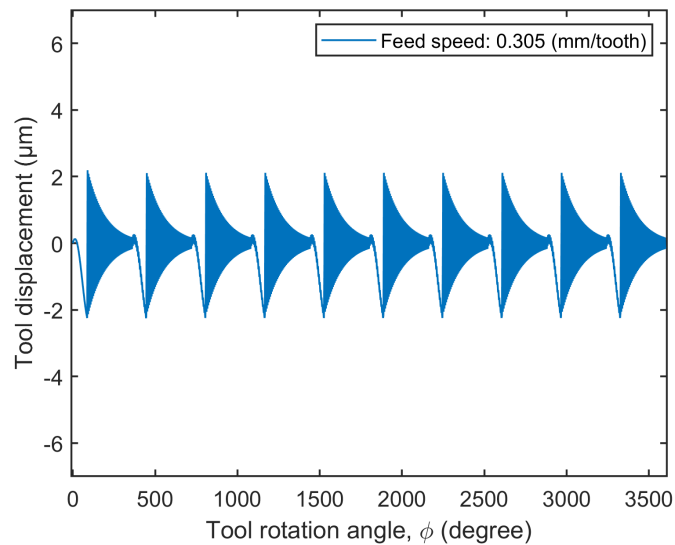


Figure 4.91: Tool displacement in the y -direction at feed: 0.305 (mm/tooth) and axial depth-of-cut: 0.15 (mm).

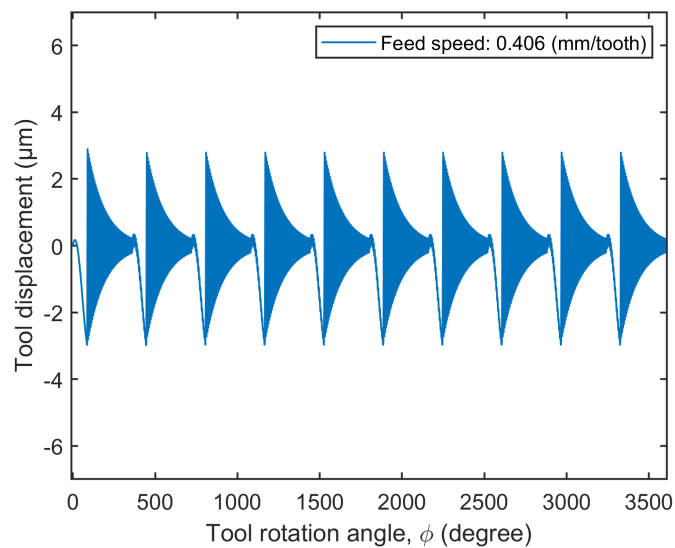


Figure 4.92: Tool displacement in the y -direction at feed: 0.406 (mm/tooth) and axial depth-of-cut: 0.15 (mm).

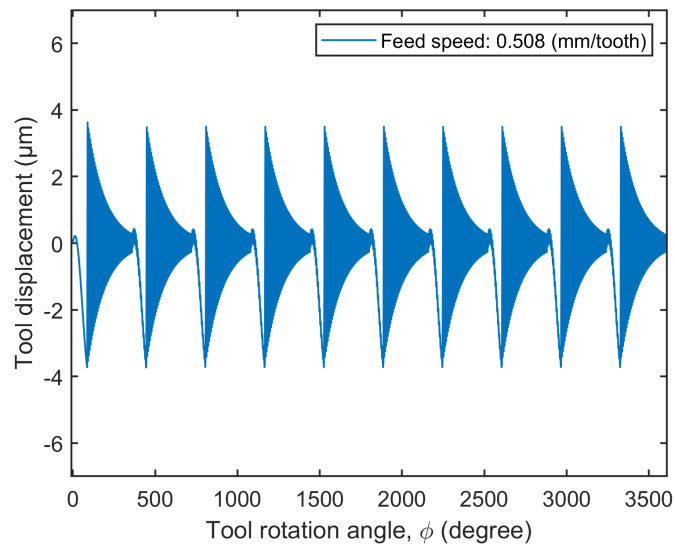


Figure 4.93: Tool displacement in the y -direction at feed: 0.508 (mm/tooth) and axial depth-of-cut: 0.15 (mm).

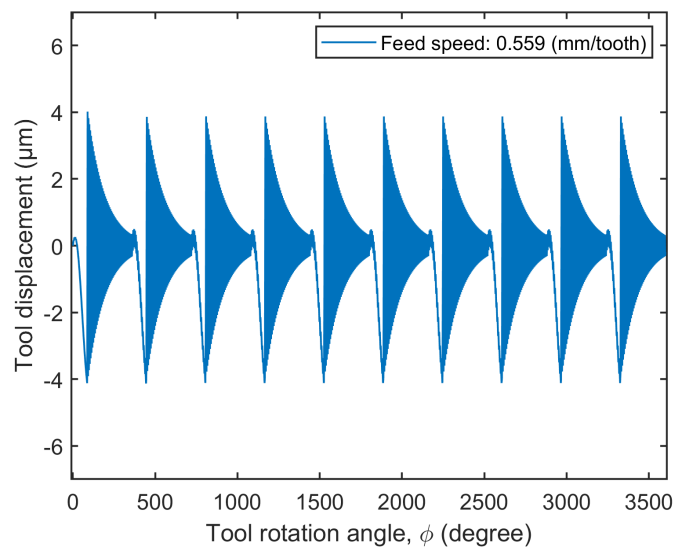


Figure 4.94: Tool displacement in the y -direction at feed: 0.559 (mm/tooth) and axial depth-of-cut: 0.15 (mm).

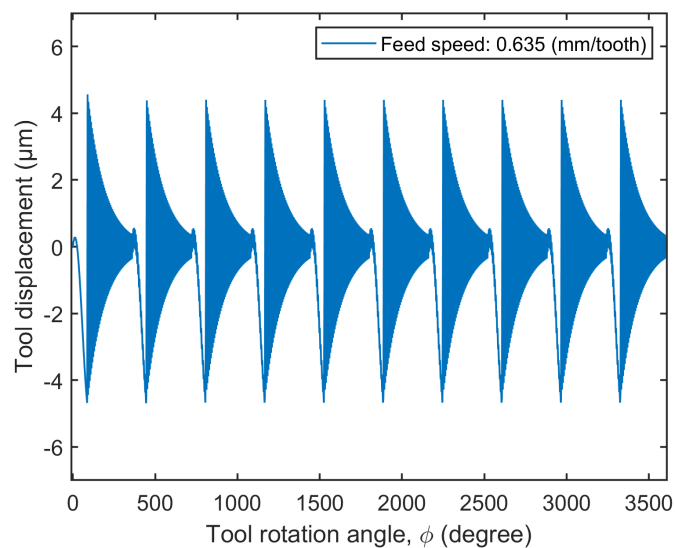


Figure 4.95: Tool displacement in the y -direction at feed: 0.635 (mm/tooth) and axial depth-of-cut: 0.15 (mm).

Tool displacement in the z -direction

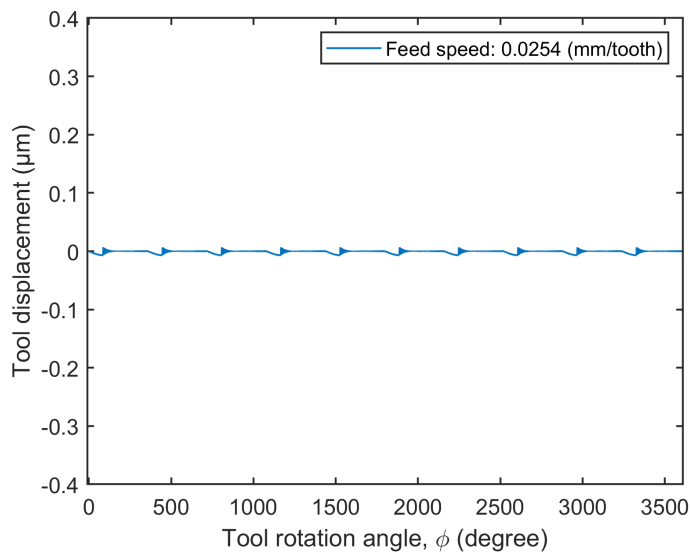


Figure 4.96: Tool displacement in the z -direction at feed: 0.0254 (mm/tooth) and axial depth-of-cut: 0.15 (mm).

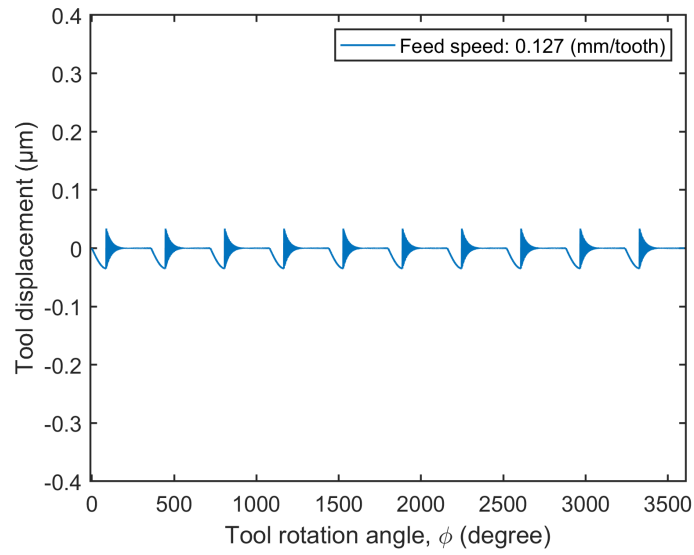


Figure 4.97: Tool displacement in the z -direction at feed: 0.127 (mm/tooth) and axial depth-of-cut: 0.15 (mm).

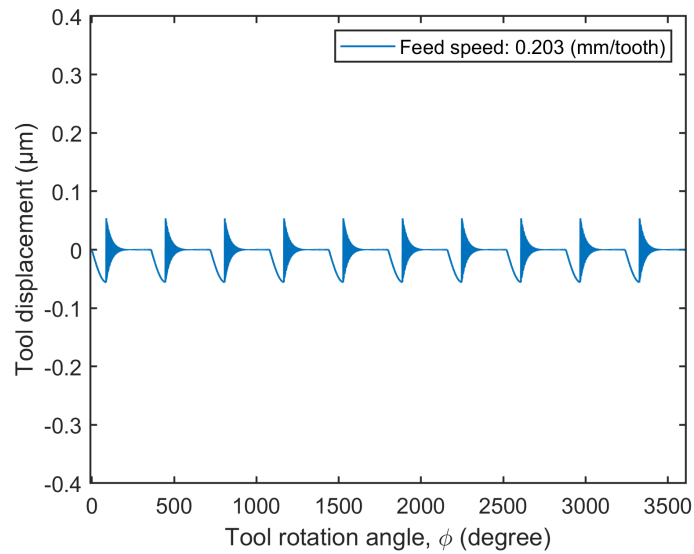


Figure 4.98: Tool displacement in the z -direction at feed: 0.203 (mm/tooth) and axial depth-of-cut: 0.15 (mm).

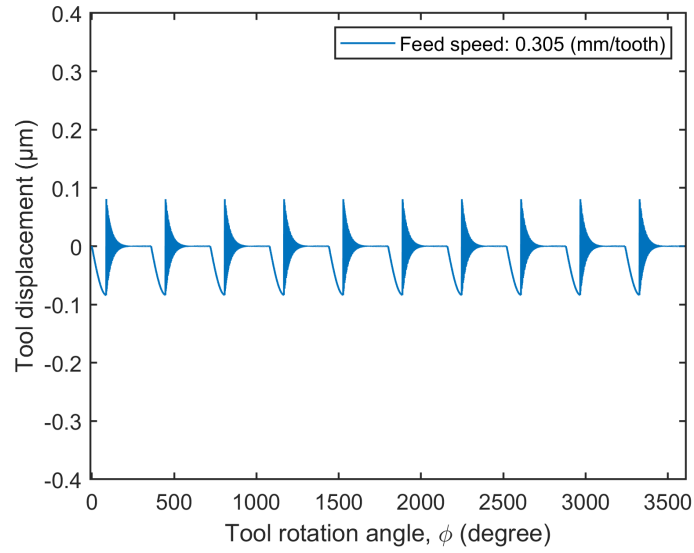


Figure 4.99: Tool displacement in the z -direction at feed: 0.305 (mm/tooth) and axial depth-of-cut: 0.15 (mm).

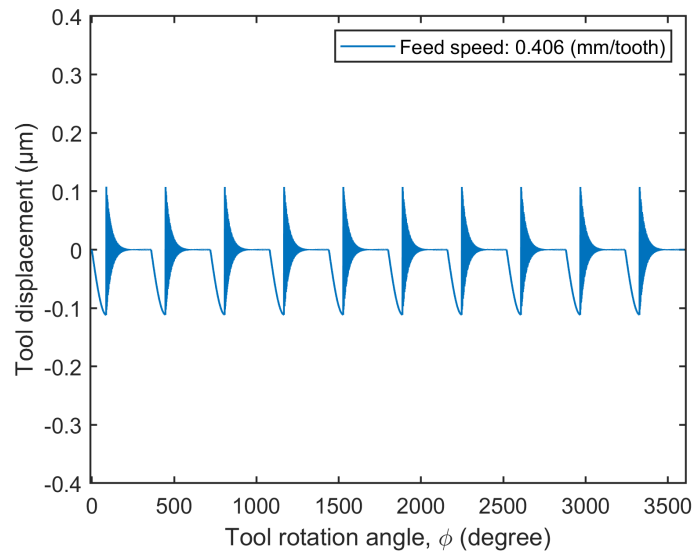


Figure 4.100: Tool displacement in the z -direction at feed: 0.406 (mm/tooth) and axial depth-of-cut: 0.15 (mm).

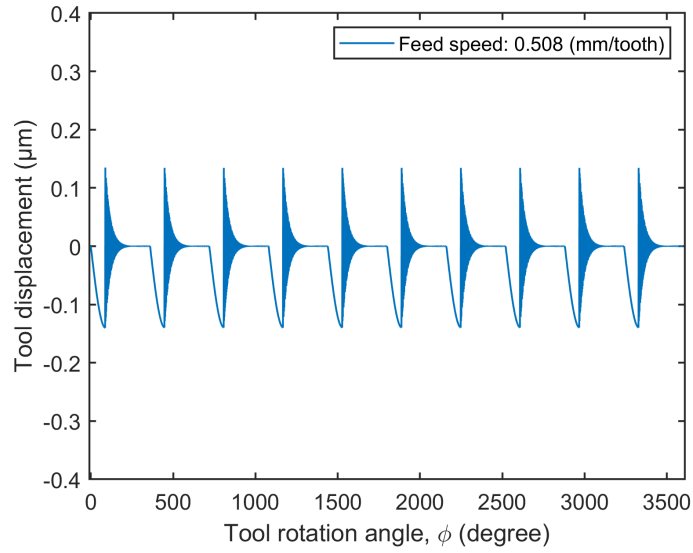


Figure 4.101: Tool displacement in the z -direction at feed: 0.508 (mm/tooth) and axial depth-of-cut: 0.15 (mm).

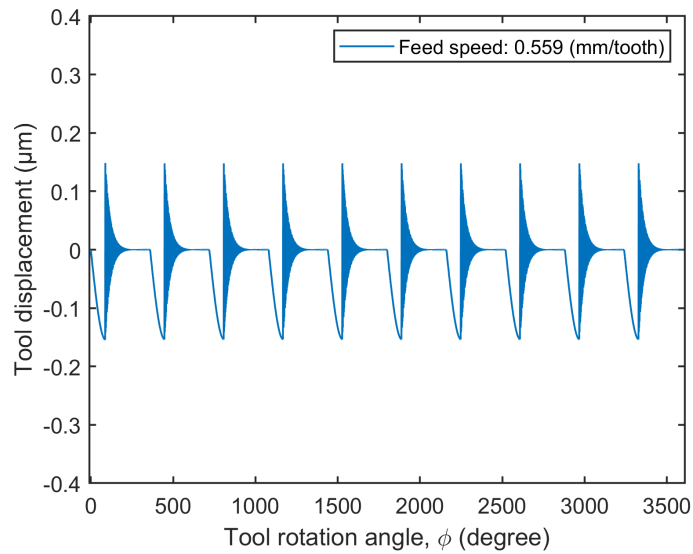


Figure 4.102: Tool displacement in the z -direction at feed: 0.559 (mm/tooth) and axial depth-of-cut: 0.15 (mm).

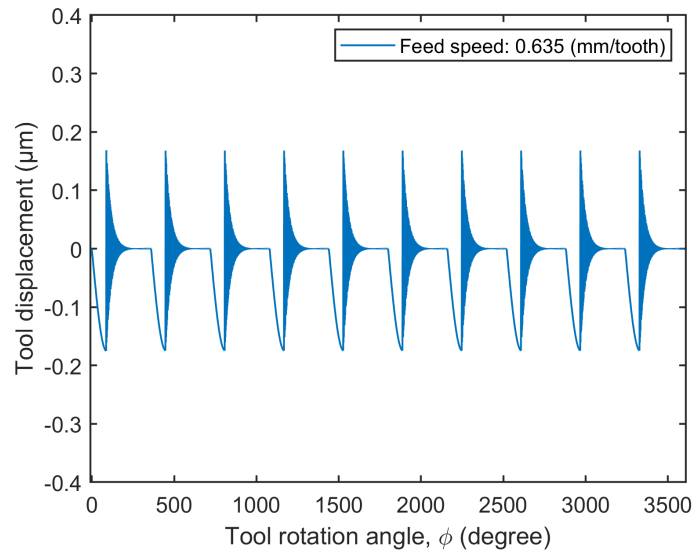


Figure 4.103: Tool displacement in the z -direction at feed: 0.635 (mm/tooth) and axial depth-of-cut: 0.15 (mm).

Tool displacement results with the axial depth-of-cut: 1 mm

Similarly, Figures 4.104 through 4.127 display the tool displacements in the x , y , and z directions for an axial depth-of-cut of 1 mm. The tool experienced the highest feed resistance in the y -axis-axis and continued to vibrate until the cutting tool rotation was completed. Despite starting metal cutting in the subsequent revolution, the cutting process remained stable. It was also observed that the maximum vibration magnitude increased with a higher feed, due to an increase in cutting force.

Tool displacement in the x -direction

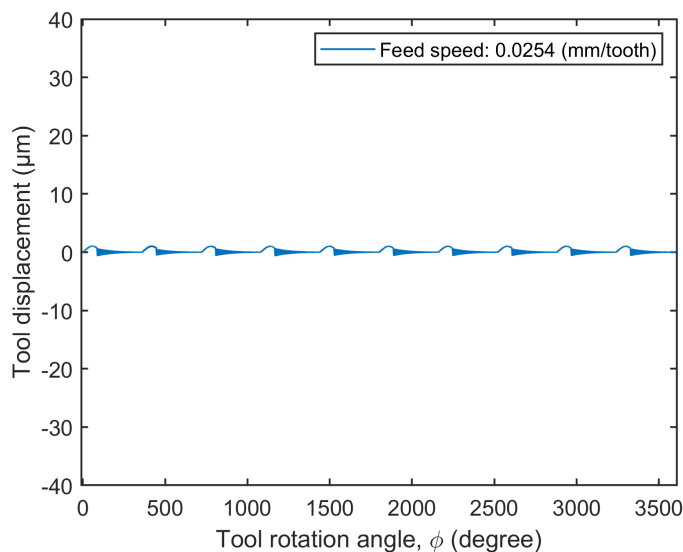


Figure 4.104: Tool displacement in the x -direction at feed: 0.0254 (mm/tooth) and axial depth-of-cut: 1 (mm).

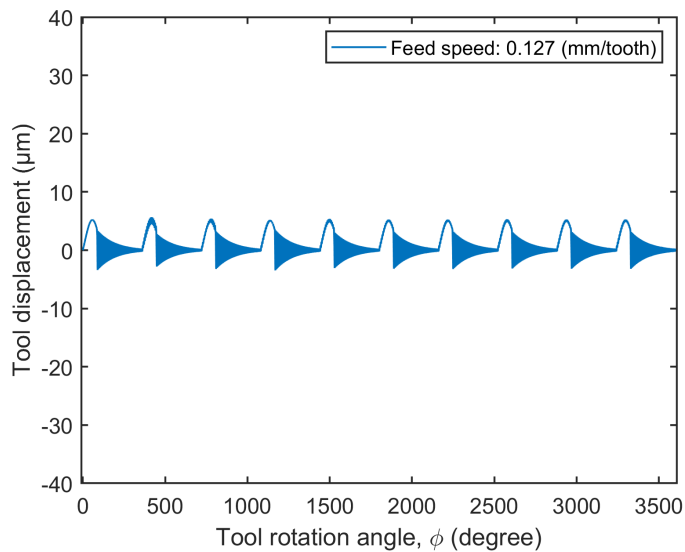


Figure 4.105: Tool displacement in the x -direction at feed: 0.127 (mm/tooth) and axial depth-of-cut: 1 (mm).

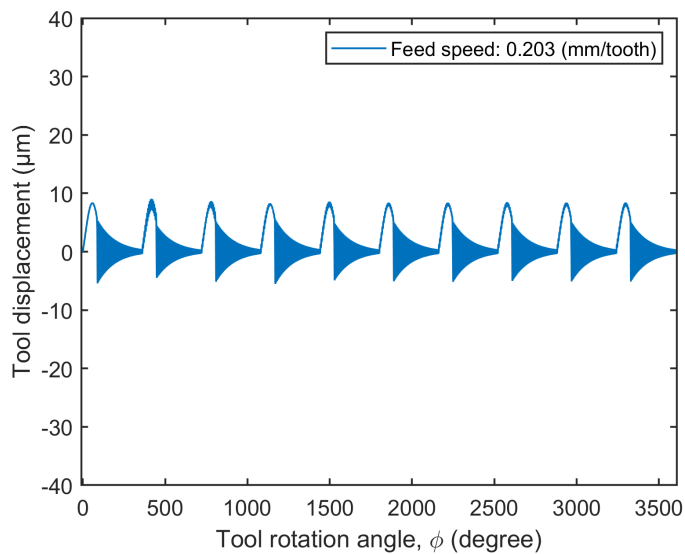


Figure 4.106: Tool displacement in the x -direction at feed: 0.203 (mm/tooth) and axial depth-of-cut: 1 (mm).

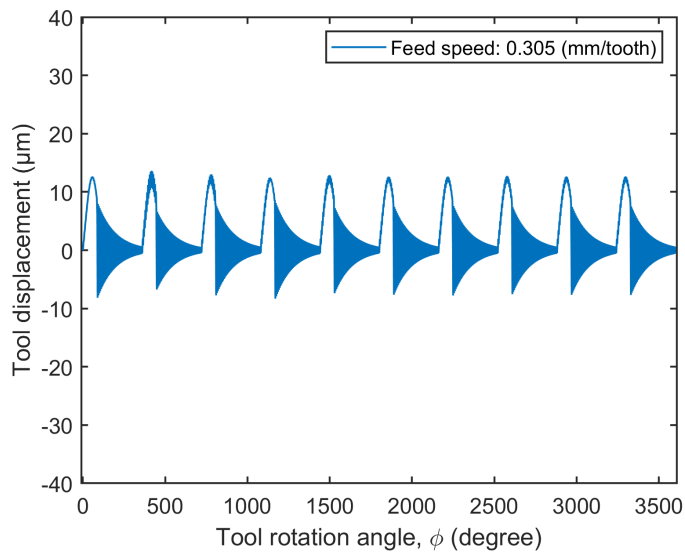


Figure 4.107: Tool displacement in the x -direction at feed: 0.305 (mm/tooth) and axial depth-of-cut: 1 (mm).

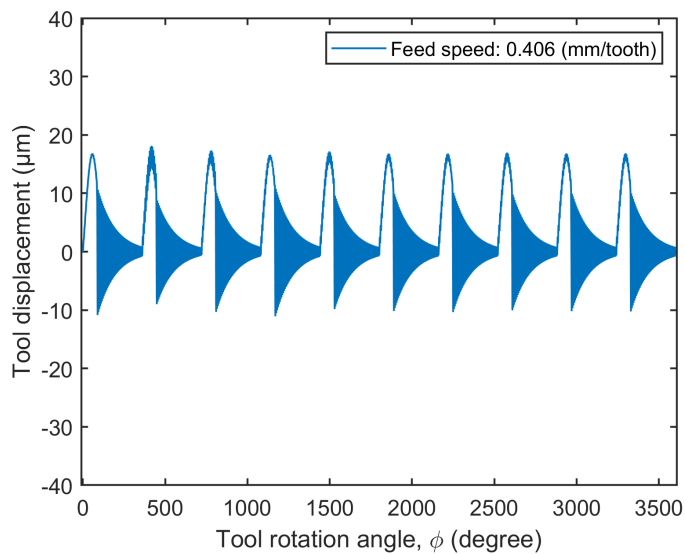


Figure 4.108: Tool displacement in the x -direction at feed: 0.406 (mm/tooth) and axial depth-of-cut: 1 (mm).

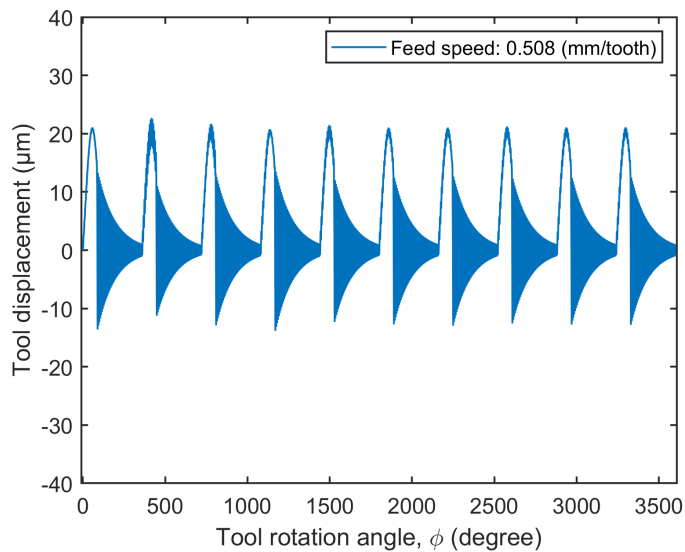


Figure 4.109: Tool displacement in the x -direction at feed: 0.508 (mm/tooth) and axial depth-of-cut: 1 (mm).

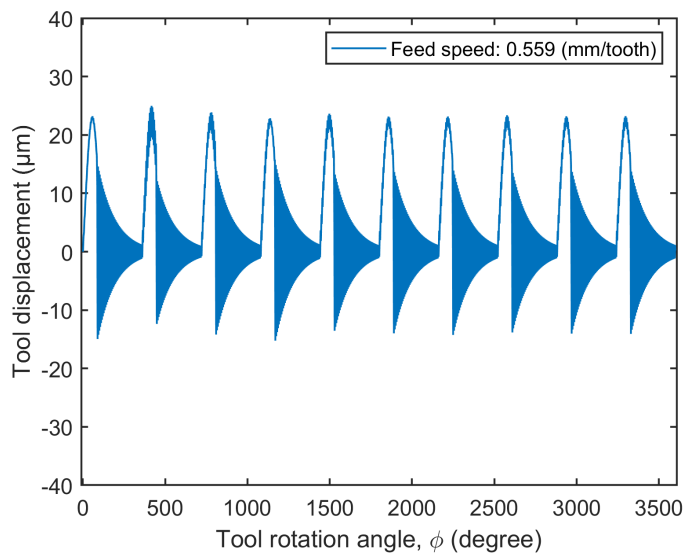


Figure 4.110: Tool displacement in the x -direction at feed: 0.559 (mm/tooth) and axial depth-of-cut: 1 (mm).

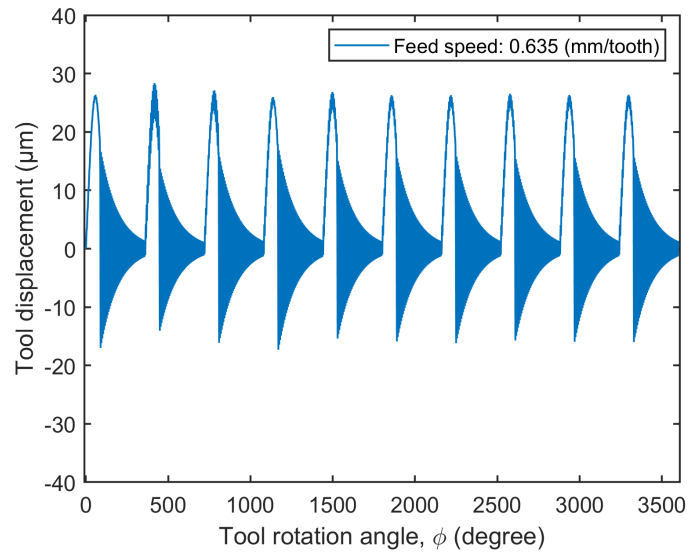


Figure 4.111: Tool displacement in the x -direction at feed: 0.635 (mm/tooth) and axial depth-of-cut: 1 (mm).

Tool displacement in the y -direction

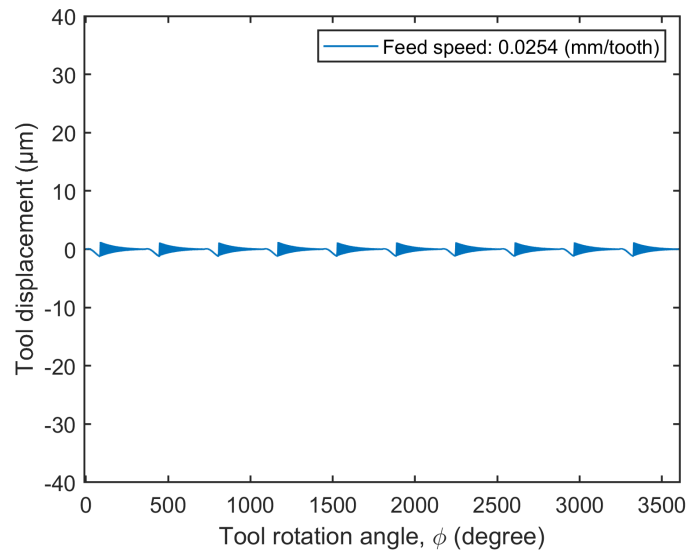


Figure 4.112: Tool displacement in the y -direction at feed: 0.0254 (mm/tooth) and axial depth-of-cut: 1 (mm).

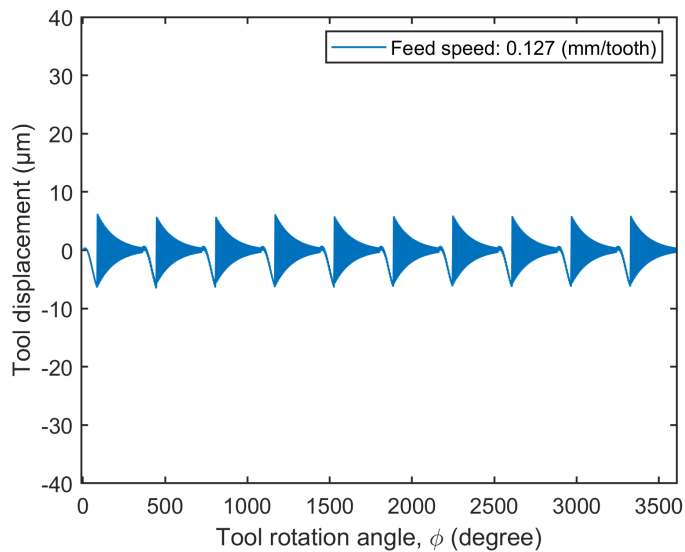


Figure 4.113: Tool displacement in the y -direction at feed: 0.127 (mm/tooth) and axial depth-of-cut: 1 (mm).

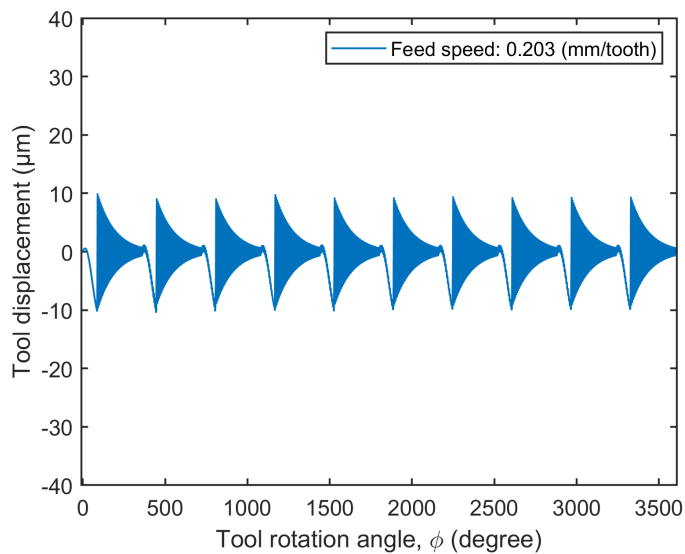


Figure 4.114: Tool displacement in the y -direction at feed: 0.203 (mm/tooth) and axial depth-of-cut: 1 (mm).

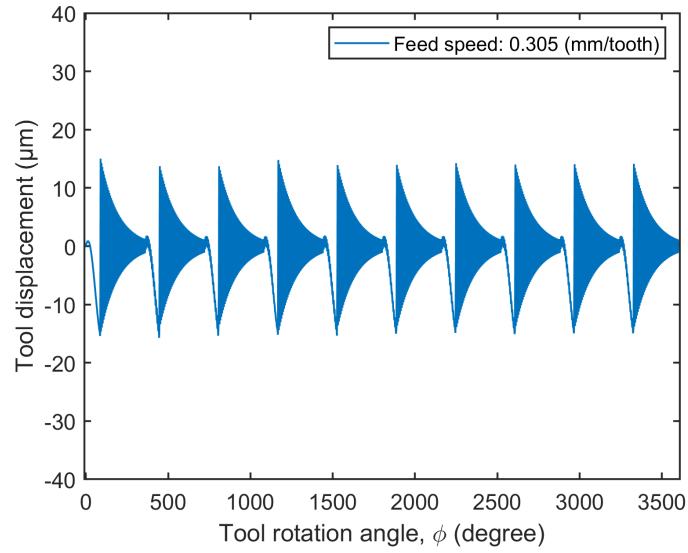


Figure 4.115: Tool displacement in the y -direction at feed: 0.305 (mm/tooth) and axial depth-of-cut: 1 (mm).

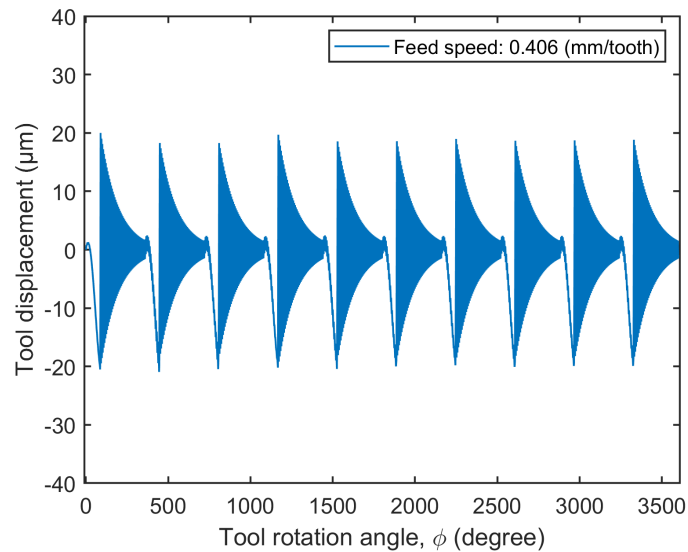


Figure 4.116: Tool displacement in the y -direction at feed: 0.406 (mm/tooth) and axial depth-of-cut: 1 (mm).

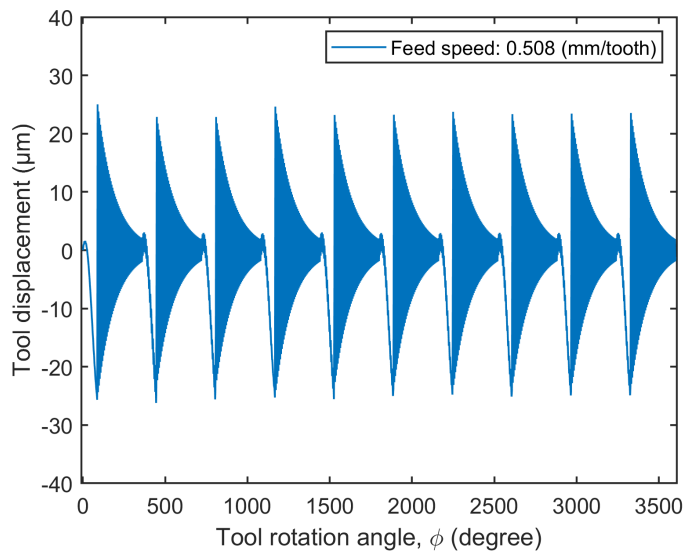


Figure 4.117: Tool displacement in the y -direction at feed: 0.508 (mm/tooth) and axial depth-of-cut: 1 (mm).

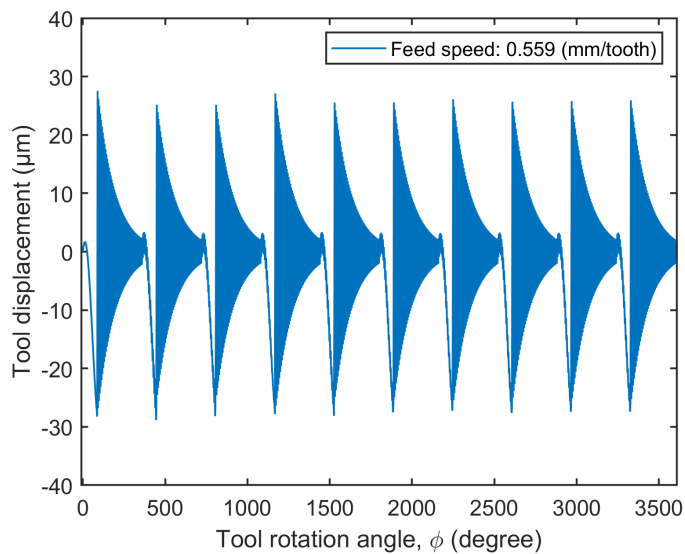


Figure 4.118: Tool displacement in the y -direction at feed: 0.559 (mm/tooth) and axial depth-of-cut: 1 (mm).

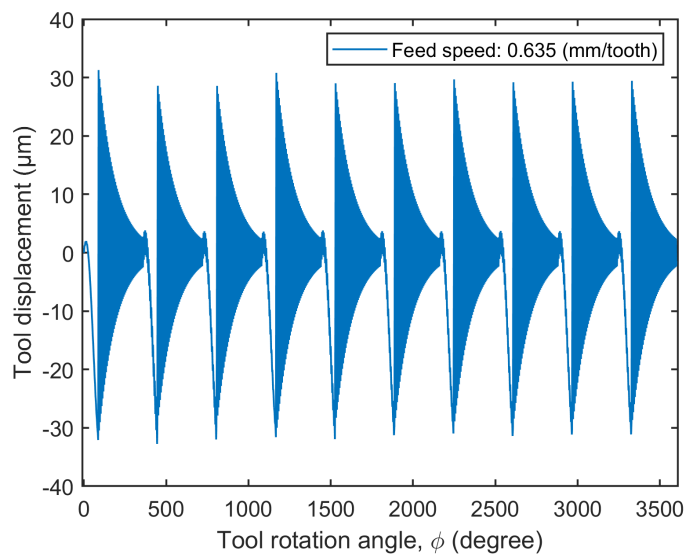


Figure 4.119: Tool displacement in the y -direction at feed: 0.635 (mm/tooth) and axial depth-of-cut: 1 (mm).

Tool displacement in the z -direction

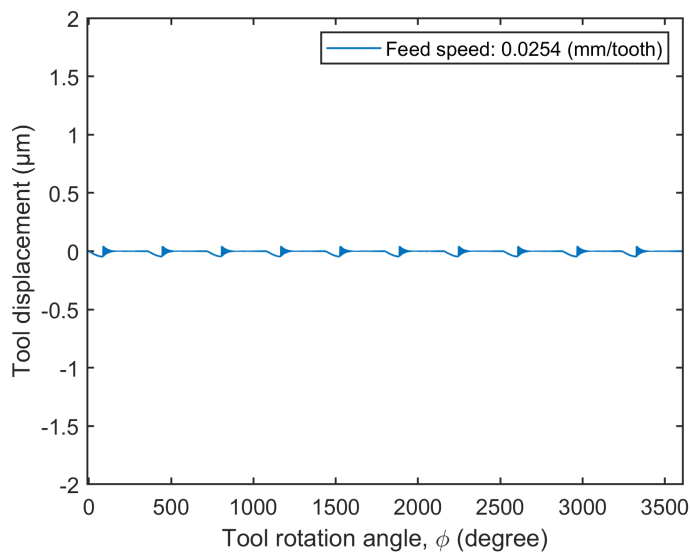


Figure 4.120: Tool displacement in the z -direction at feed: 0.0254 (mm/tooth) and axial depth-of-cut: 1 (mm).

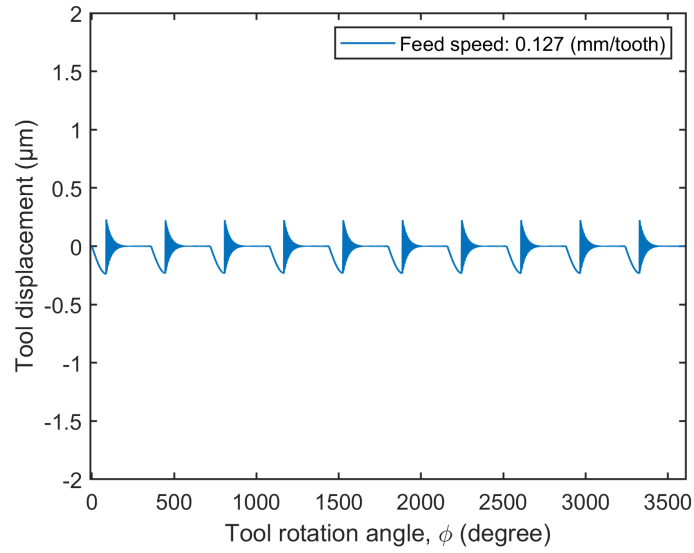


Figure 4.121: Tool displacement in the z -direction at feed: 0.127 (mm/tooth) and axial depth-of-cut: 1 (mm).

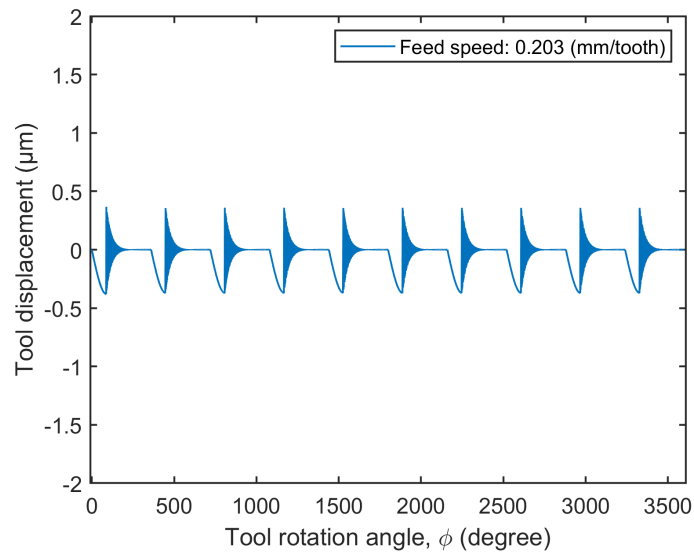


Figure 4.122: Tool displacement in the z -direction at feed: 0.203 (mm/tooth) and axial depth-of-cut: 1 (mm).

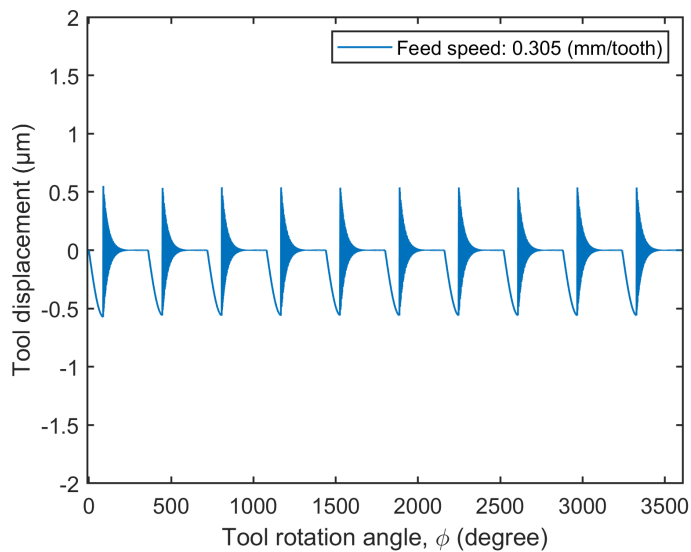


Figure 4.123: Tool displacement in the z -direction at feed: 0.305 (mm/tooth) and axial depth-of-cut: 1 (mm).

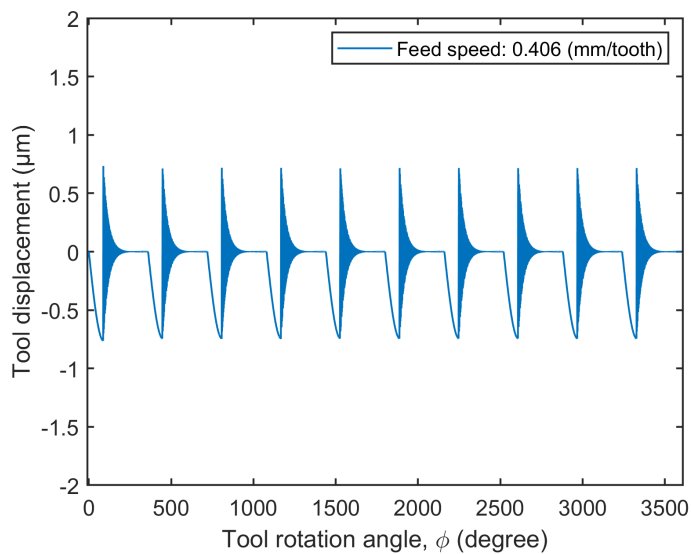


Figure 4.124: Tool displacement in the z -direction at feed: 0.406 (mm/tooth) and axial depth-of-cut: 1 (mm).

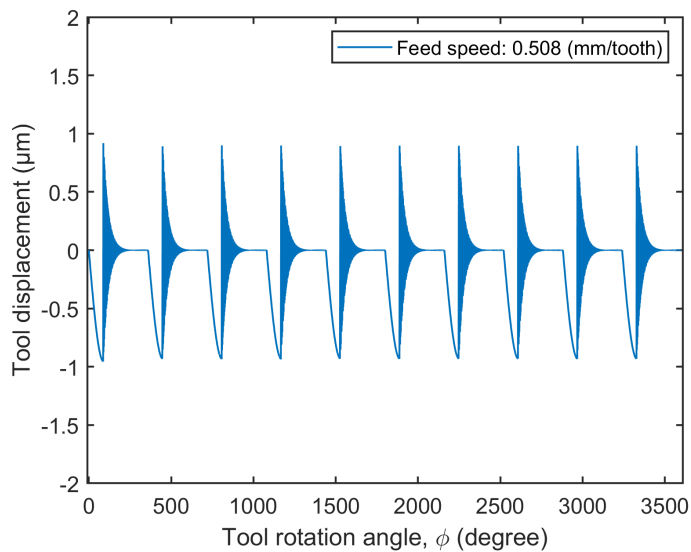


Figure 4.125: Tool displacement in the z -direction at feed: 0.508 (mm/tooth) and axial depth-of-cut: 1 (mm).

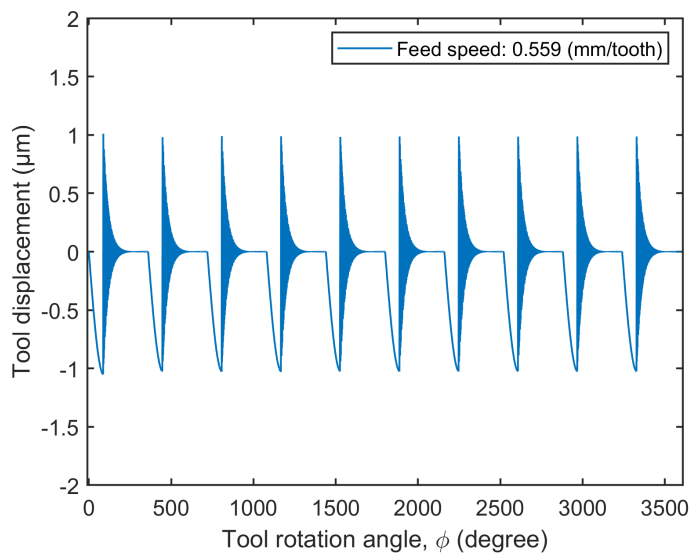


Figure 4.126: Tool displacement in the z -direction at feed: 0.559 (mm/tooth) and axial depth-of-cut: 1 (mm).

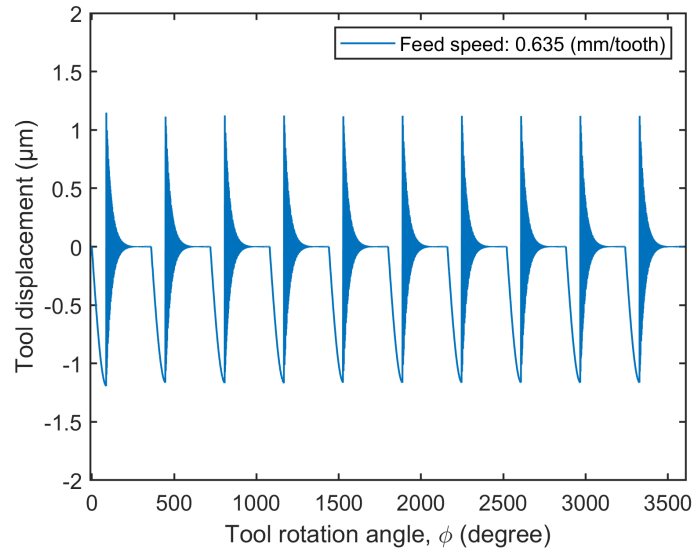


Figure 4.127: Tool displacement in the z -direction at feed: 0.635 (mm/tooth) and axial depth-of-cut: 1 (mm).

Tool displacement results with the axial depth-of-cut: 5 mm

Figures 4.128 through 4.151 show the tool vibrations in the x , y , and z directions at an axial depth-of-cut of 5 mm. The higher depth-of-cut generated significant vibration than 0.15 mm and 1 mm depth-of-cuts. Moreover, residual vibration on the tool increased or decreased unstably since the cutting process frequency was close to the system's natural frequency.

Tool displacement in the x -direction

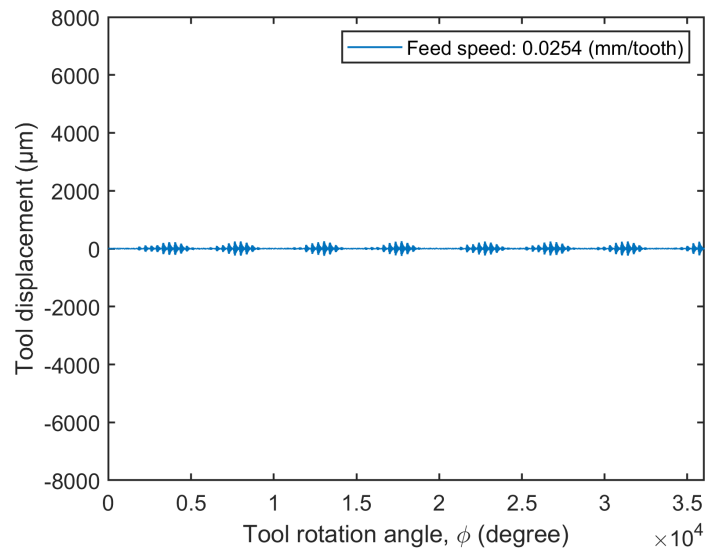


Figure 4.128: Tool displacement in the x -direction at feed: 0.0254 (mm/tooth) and axial depth-of-cut: 5 (mm).

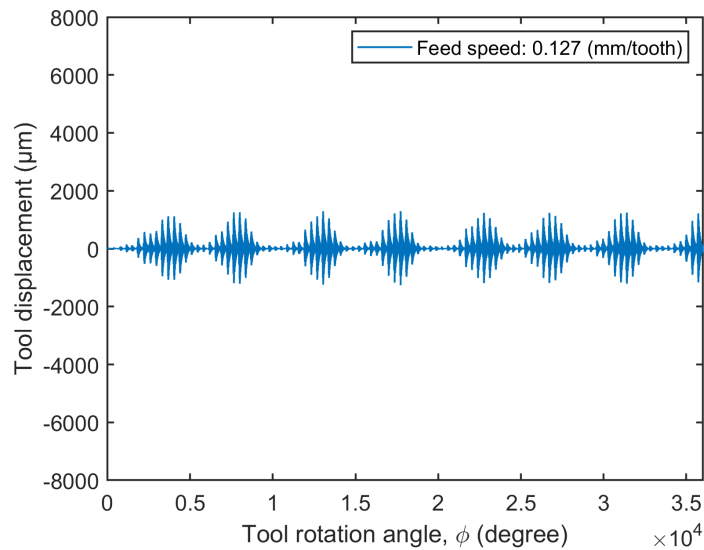


Figure 4.129: Tool displacement in the x -direction at feed: 0.127 (mm/tooth) and axial depth-of-cut: 5 (mm).

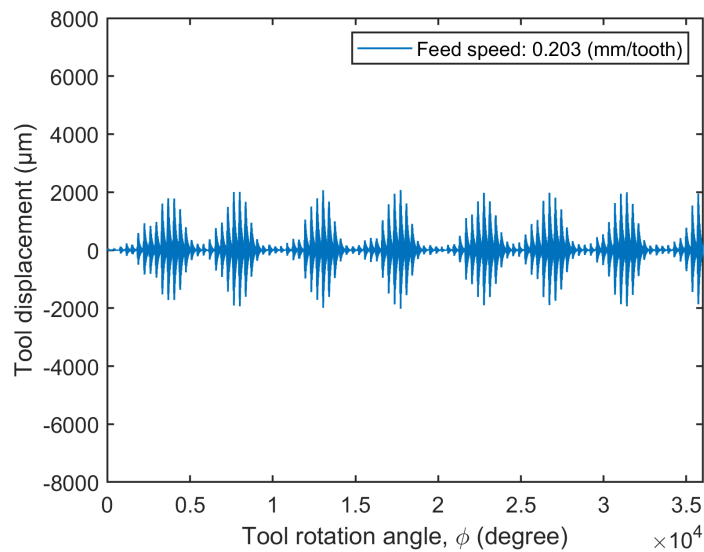


Figure 4.130: Tool displacement in the x -direction at feed: 0.203 (mm/tooth) and axial depth-of-cut: 5 (mm).

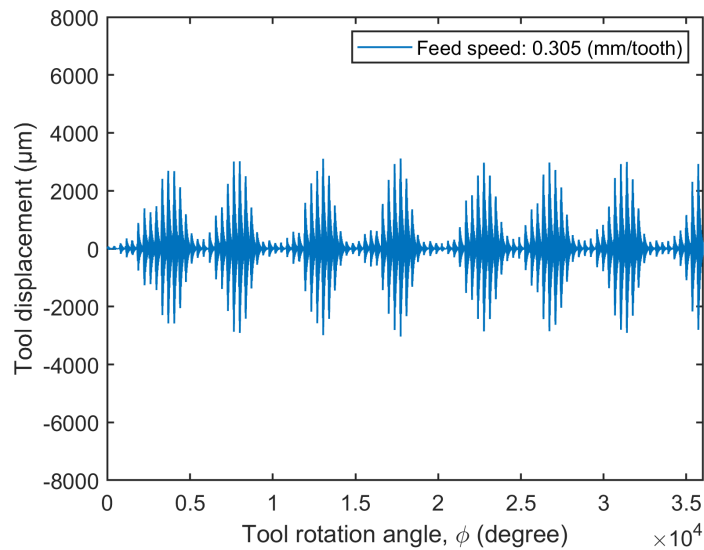


Figure 4.131: Tool displacement in the x -direction at feed: 0.305 (mm/tooth) and axial depth-of-cut: 5 (mm).

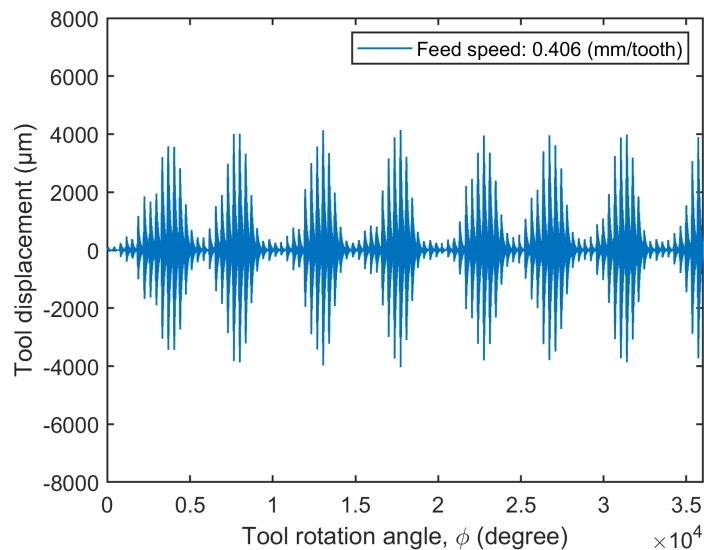


Figure 4.132: Tool displacement in the x -direction at feed: 0.406 (mm/tooth) and axial depth-of-cut: 5 (mm).

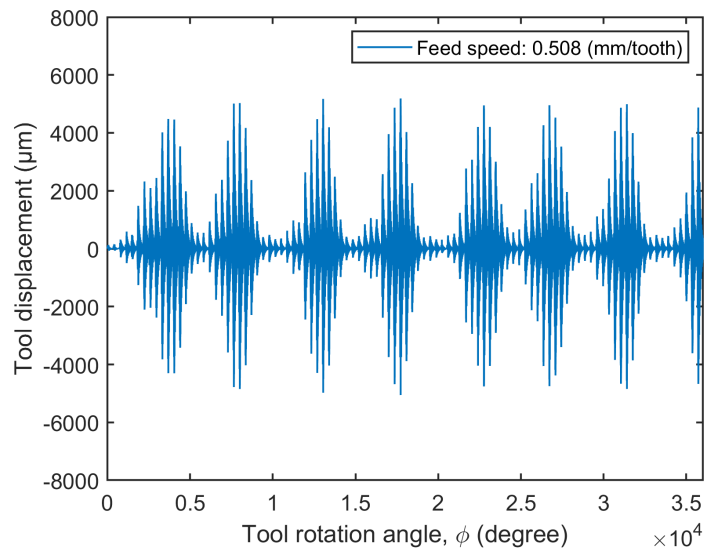


Figure 4.133: Tool displacement in the x -direction at feed: 0.508 (mm/tooth) and axial depth-of-cut: 5 (mm).

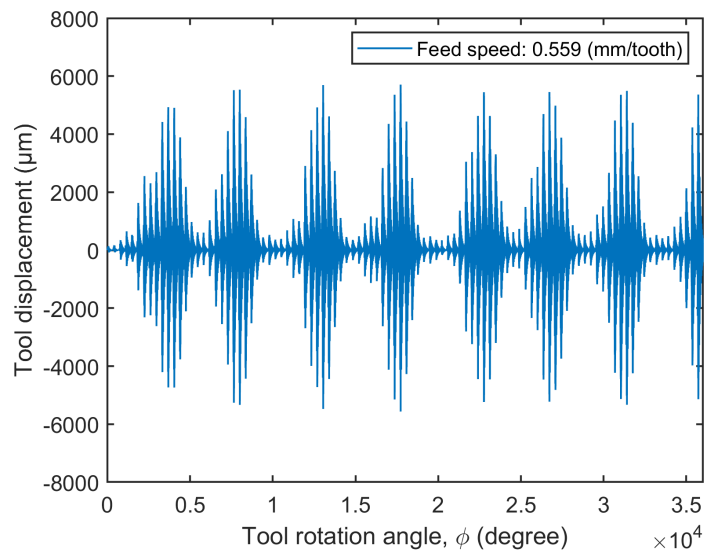


Figure 4.134: Tool displacement in the x -direction at feed: 0.559 (mm/tooth) and axial depth-of-cut: 5 (mm).

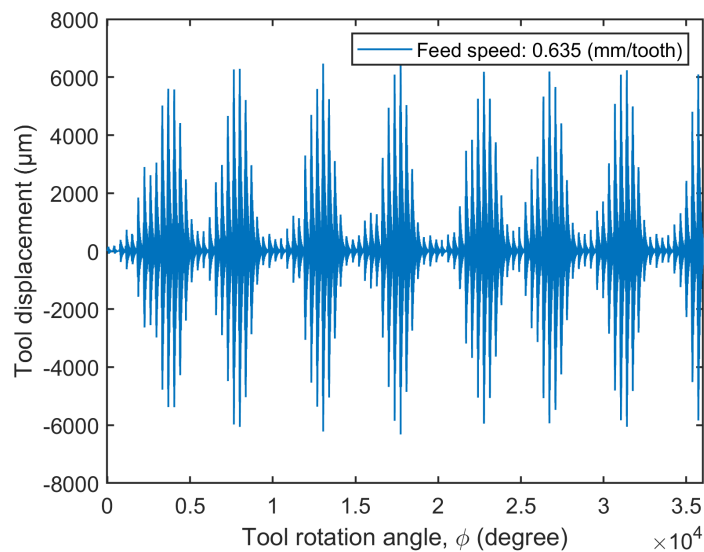


Figure 4.135: Tool displacement in the x -direction at feed: 0.635 (mm/tooth) and axial depth-of-cut: 5 (mm).

Tool displacement in the y -direction

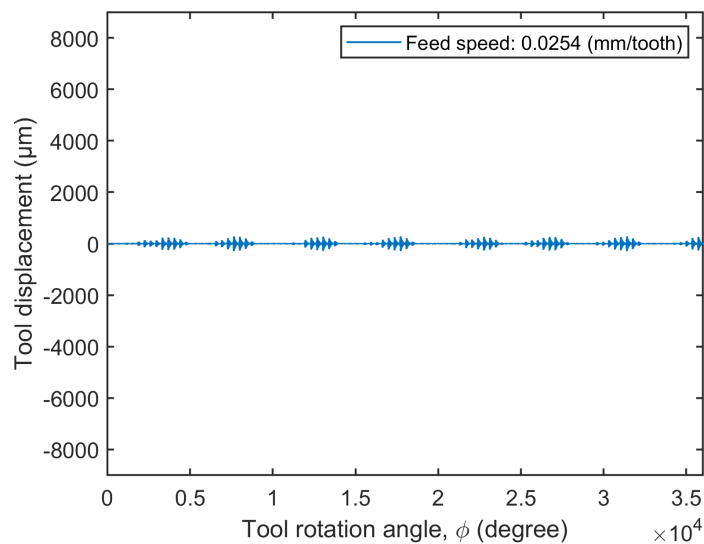


Figure 4.136: Tool displacement in the y -direction at feed: 0.0254 (mm/tooth) and axial depth-of-cut: 5 (mm).

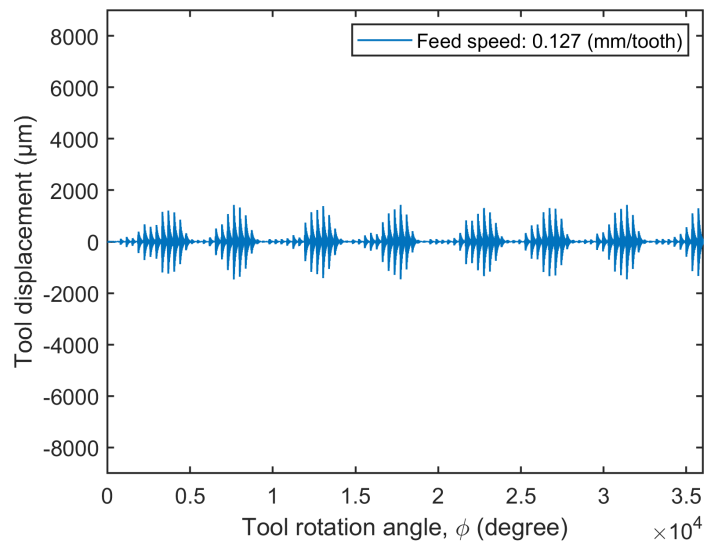


Figure 4.137: Tool displacement in the y -direction at feed: 0.127 (mm/tooth) and axial depth-of-cut: 5 (mm).

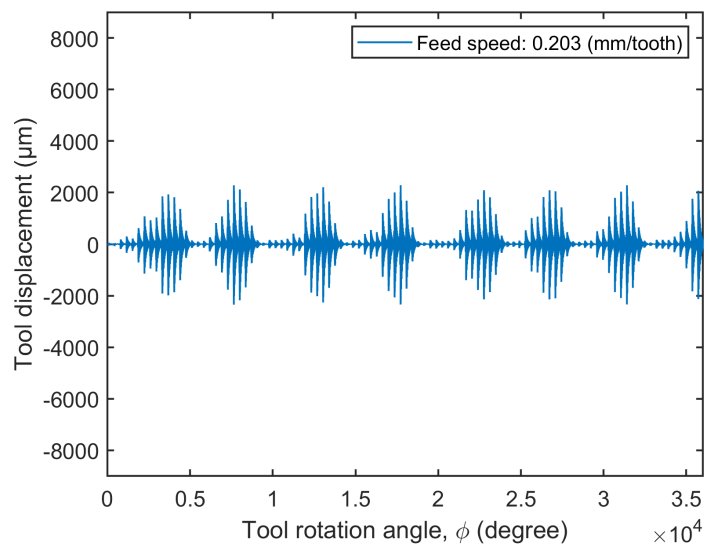


Figure 4.138: Tool displacement in the y -direction at feed: 0.203 (mm/tooth) and axial depth-of-cut: 5 (mm).

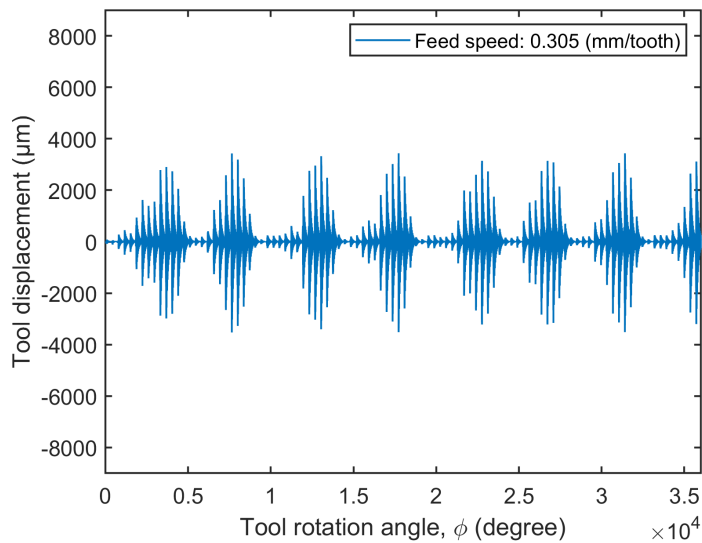


Figure 4.139: Tool displacement in the y -direction at feed: 0.305 (mm/tooth) and axial depth-of-cut: 5 (mm).

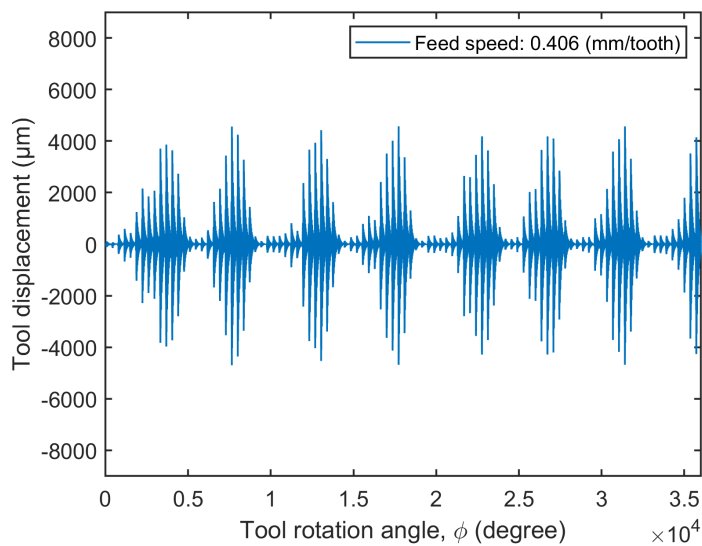


Figure 4.140: Tool displacement in the y -direction at feed: 0.406 (mm/tooth) and axial depth-of-cut: 5 (mm).

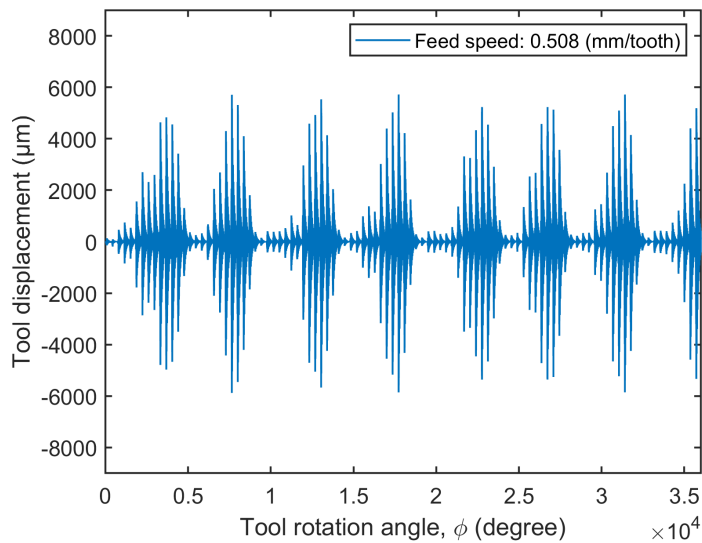


Figure 4.141: Tool displacement in the y -direction at feed: 0.508 (mm/tooth) and axial depth-of-cut: 5 (mm).

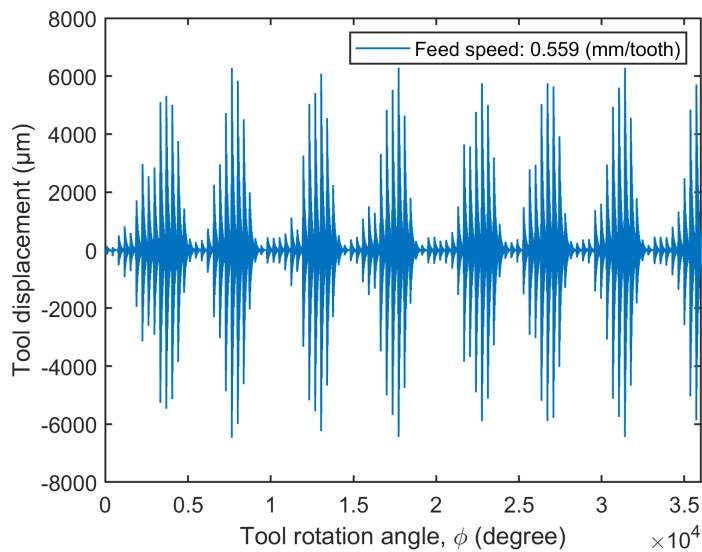


Figure 4.142: Tool displacement in the y -direction at feed: 0.559 (mm/tooth) and axial depth-of-cut: 5 (mm).

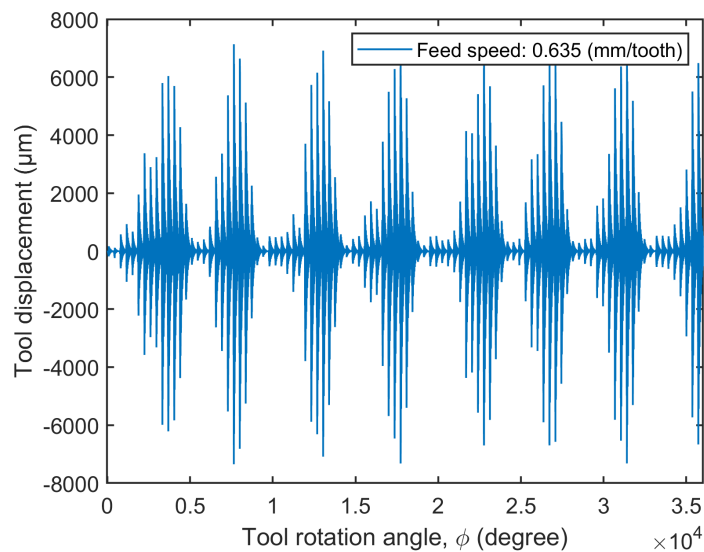


Figure 4.143: Tool displacement in the y -direction at feed: 0.635 (mm/tooth) and axial depth-of-cut: 5 (mm).

Tool displacement in the z -direction

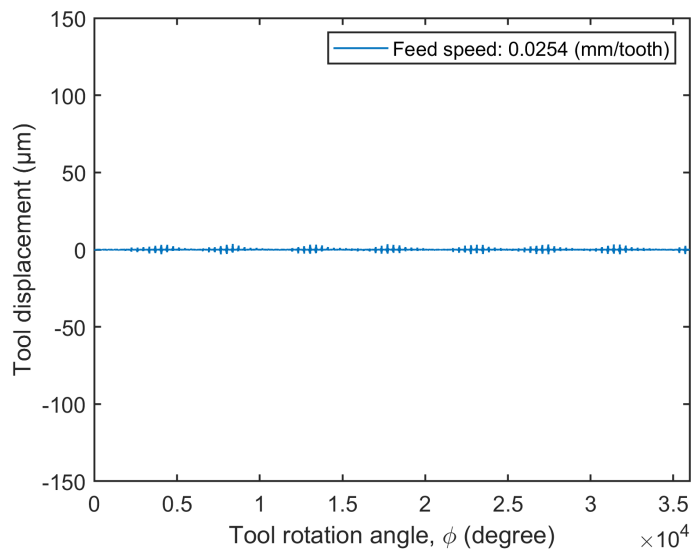


Figure 4.144: Tool displacement in the z -direction at feed: 0.0254 (mm/tooth) and axial depth-of-cut: 5 (mm).

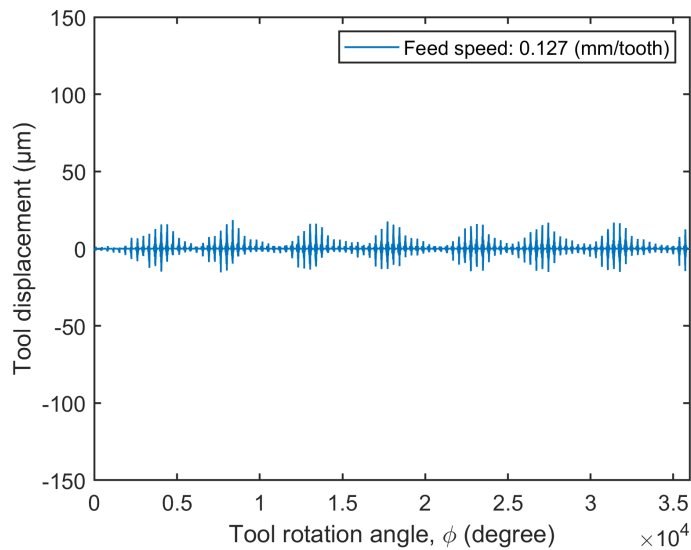


Figure 4.145: Tool displacement in the z -direction at feed: 0.127 (mm/tooth) and axial depth-of-cut: 5 (mm).

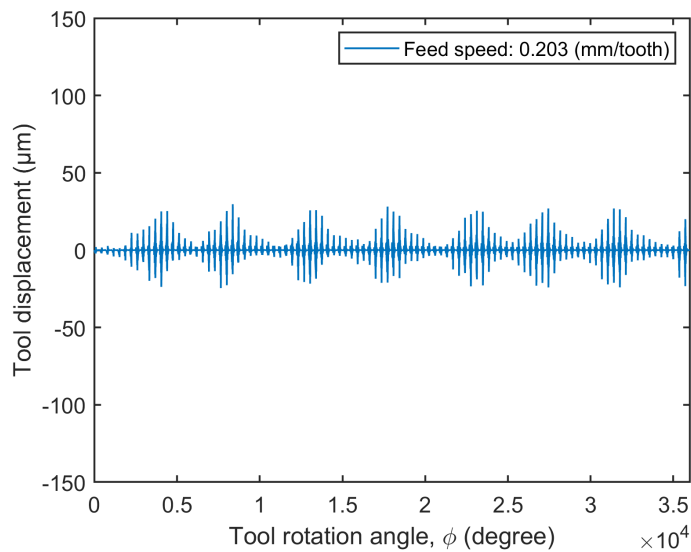


Figure 4.146: Tool displacement in the z -direction at feed: 0.203 (mm/tooth) and axial depth-of-cut: 5 (mm).

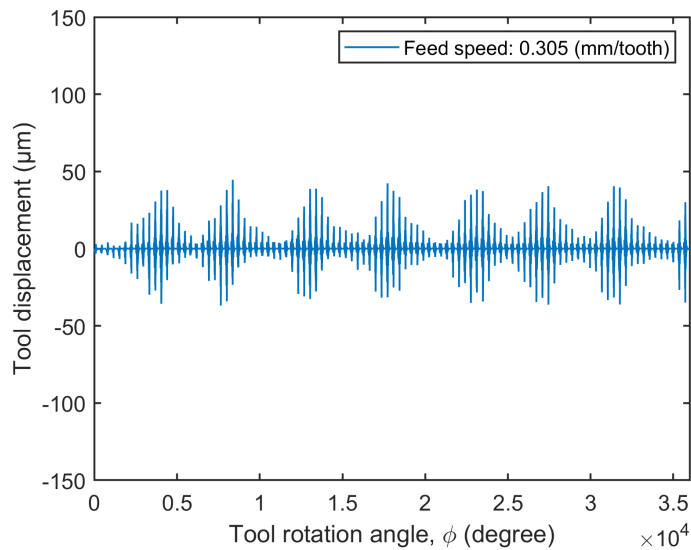


Figure 4.147: Tool displacement in the z -direction at feed: 0.305 (mm/tooth) and axial depth-of-cut: 5 (mm).

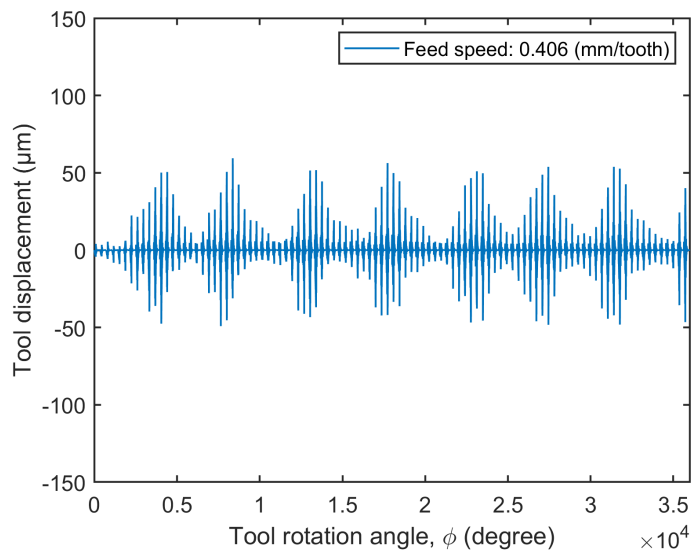


Figure 4.148: Tool displacement in the z -direction at feed: 0.406 (mm/tooth) and axial depth-of-cut: 5 (mm).

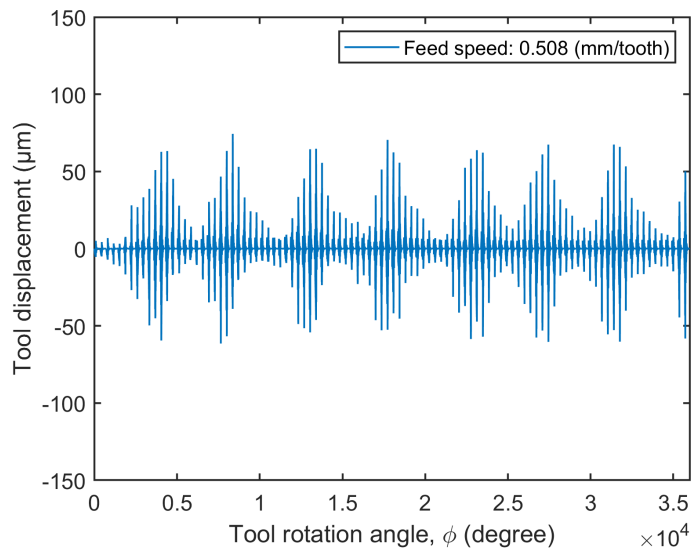


Figure 4.149: Tool displacement in the z -direction at feed: 0.508 (mm/tooth) and axial depth-of-cut: 5 (mm).

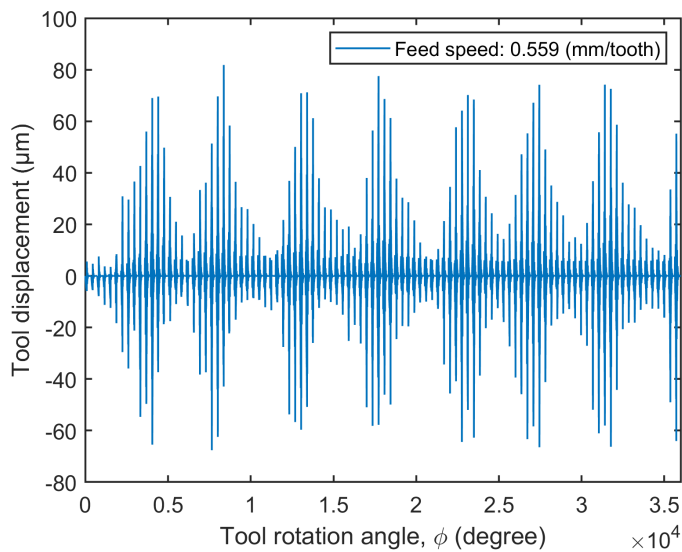


Figure 4.150: Tool displacement in the z -direction at feed: 0.559 (mm/tooth) and axial depth-of-cut: 5 (mm).

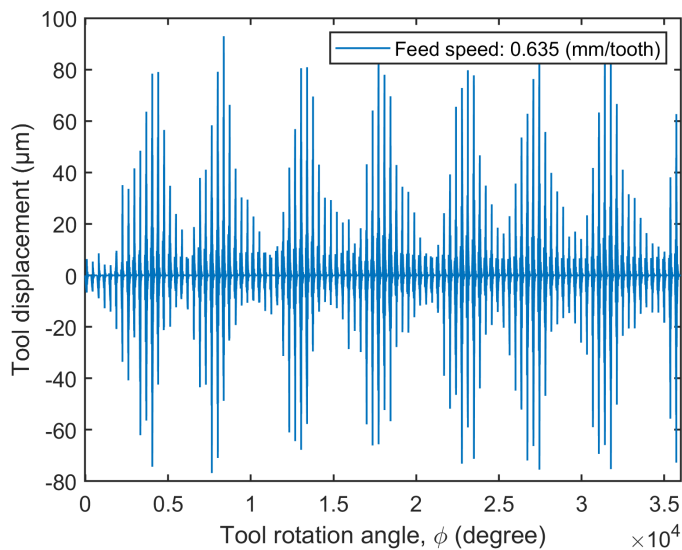


Figure 4.151: Tool displacement in the z -direction at feed: 0.635 (mm/tooth) and axial depth-of-cut: 5 (mm).

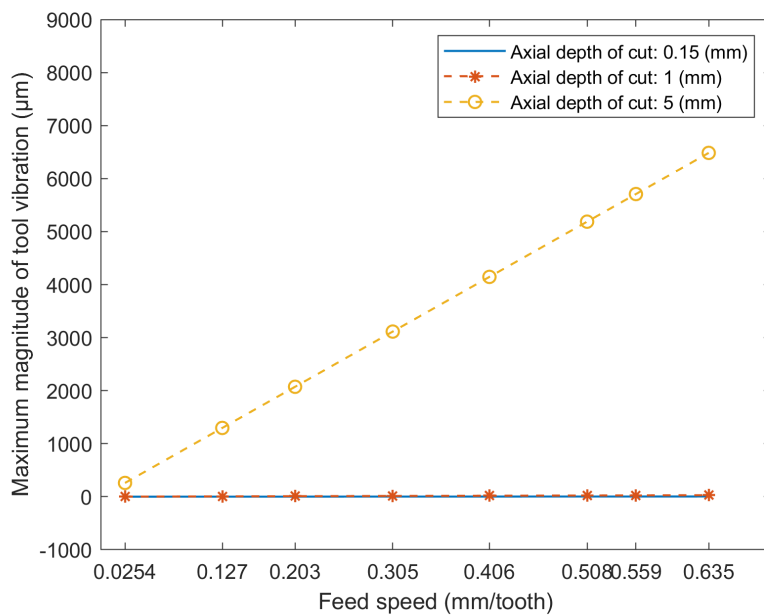


Figure 4.152: Computed maximum tool displacement in the x -direction with three axial depth-of-cuts.

Figure 4.152 compares the maximum magnitude of the tool vibration in the x -direction at various feeds for the three axial depth-of-cuts studied. When the axial depth-of-cut was increased, the maximum magnitude of tool vibration in the x -direction was linearly increased.

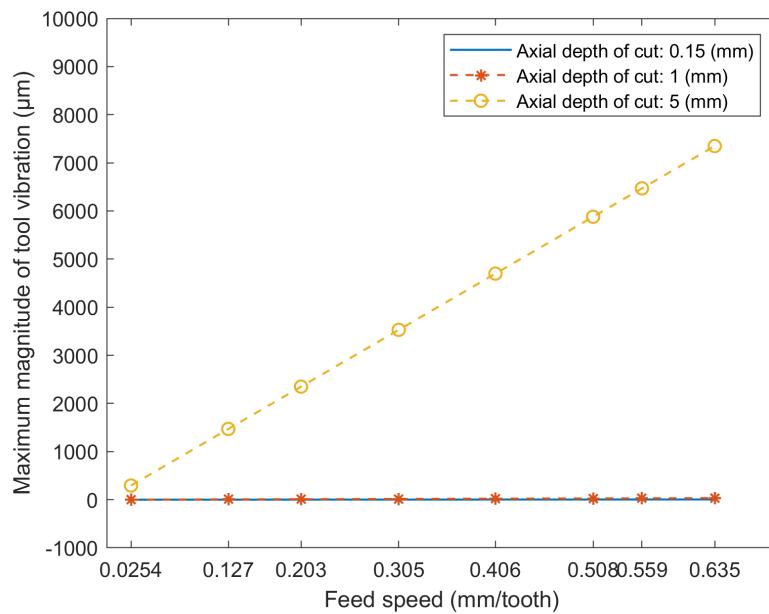


Figure 4.153: Computed maximum tool displacement in the y -direction with three axial depth-of-cuts.

Similarly, Figures 4.153 and 4.154 compare the maximum magnitude of the tool displacement in the y and z directions, respectively. As shown in Figures 4.77, 4.78, and 4.79, the highest magnitude of cutting forces in the y direction resulted in the highest tool vibrations along with an increase in feed speed (mm/tooth) and axial depth-of-cut.

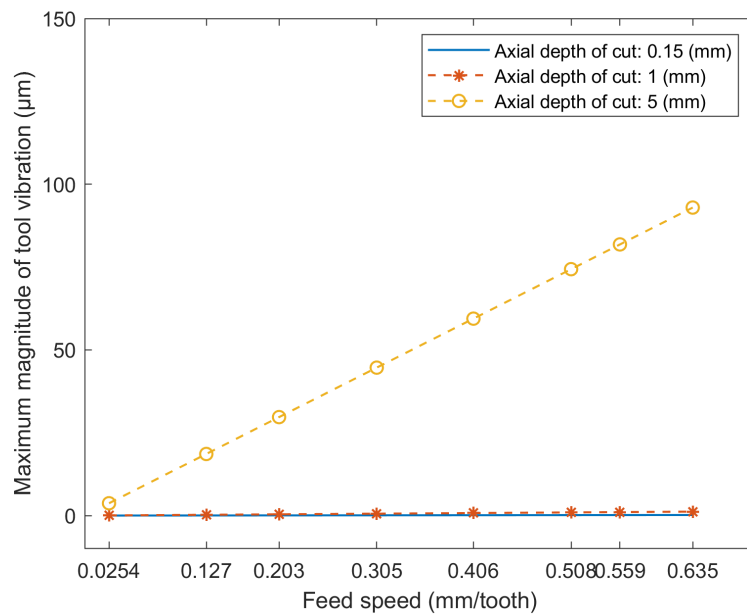


Figure 4.154: Computed maximum tool displacement in the z-direction with three axial depth-of-cuts.

4.3 Surface roughness results from milling experiments

To determine a range of surface roughness and compare it with a computed range of surface roughness, 27 readings were obtained at each machined surface, and all measurements are listed in Appendix C.

Table 4.7: Experiment surface roughness results at axial depth-of-cut of 0.15 mm.

Feed (mm/tooth)	Minimum (μm)	Maximum (μm)	Average (μm)
0.0254	0.0510	0.078	0.0613
0.127	0.100	0.182	0.129
0.203	0.086	0.243	0.153
0.305	0.116	0.246	0.1655
0.406	0.130	0.290	0.210
0.508	0.130	0.282	0.225
0.559	0.163	0.350	0.248
0.632	0.165	0.389	0.244

As listed in table 4.7, the surface roughness obtained by milling experiments is summarized. The maximum surface roughness increased with an increasing feed speed,

and the average surface roughness increased except in the experiment at a feed speed of 0.632 mm/tooth.

Table 4.8: Experiment surface roughness results at axial depth-of-cut of 1 mm.

Feed (mm/tooth)	Minimum (μm)	Maximum (μm)	Average (μm)
0.0254	0.049	0.196	0.073
0.127	0.074	0.220	0.116
0.203	0.071	0.224	0.143
0.305	0.099	0.373	0.161
0.406	0.094	0.269	0.206
0.508	0.122	0.419	0.242
0.559	0.147	0.442	0.262
0.632	0.173	0.399	0.285

In Table 4.8, the surface finish are listed when the axial depth-of-cut was 1 mm. Similarly, the average surface roughness generally increased with increasing feed speed. However, a significant difference in maximum and average surface finish was not observed between axial depth-of-cuts of 0.15 mm and 1 mm.

Table 4.9: Surface roughness experiment results at axial depth-of-cut of 5 mm.

Feed (mm/tooth)	Minimum (μm)	Maximum (μm)	Average (μm)
0.0254	0.064	0.189	0.089
0.127	0.084	0.204	0.140
0.203	0.107	0.337	0.210
0.305	0.169	0.536	0.324
0.406	0.118	0.461	0.258
0.508	0.259	1.372	0.864
0.559	0.318	1.929	1.137
0.632	0.44	3.53	1.43

Table 4.9 presented the results of milling operations performed with an axial depth-of-cut of 5 mm. With varying feed speeds, the gap between the minimum and maximum surface roughness is higher than the values obtained at the axial depth-of-cuts of 0.15 mm and 1 mm.

Arithmetic surface roughness

The results listed in Table 4.10 were obtained by using the arithmetic surface roughness Eq.(1.11). The arithmetic surface roughness model depends only on the feed and tool nose radius and does not consider the effect of vibration on surface roughness. Thus, while the surface roughness values obtained by milling experiments increased along with the increase in axial depth-of-cuts, the arithmetic surface roughness did not estimate the surface roughness.

Table 4.10: Average surface roughness estimation by arithmetic surface roughness Eq (1.11).

Feed (mm/tooth)	Surface roughness		
	Axial depth-of-cut:	Axial depth-of-cut:	Axial depth-of-cut:
	0.15 mm (μm)	1 mm (μm)	5 mm (μm)
0.0254	0.026	0.026	0.026
0.127	0.647	0.647	0.647
0.203	1.658	1.658	1.658
0.305	3.757	3.757	3.757
0.406	6.696	6.696	6.696
0.508	10.564	10.564	10.564
0.559	12.850	12.850	12.850
0.632	16.711	16.711	16.711

It turns out that the arithmetic surface roughness is not proper to estimate the

surface roughness with respect to various axial depth-of-cuts. In addition, when a square insert is used in the milling process, the arithmetic surface roughness cannot predict the surface finish properly.

Mathematical surface roughness

The results in Table 4.11 were computed using Eq.(2.54) for the mathematical surface roughness model. The mathematical surface roughness values were considered the maximum and minimum tool vibrations in the x direction (feed direction) and tool geometry.

Table 4.11: Surface roughness estimation by mathematical surface roughness Eq (2.54).

Axial depth-of-cut (mm)	Feed (mm/tooth)	Minimum (μm)	Maximum (μm)	Mean (μm)
0.15	0.0254	0.026	0.026	0.026
	0.127	0.642	0.656	0.656
	0.203	1.645	1.679	1.679
	0.305	3.728	3.805	3.805
	0.406	6.644	6.782	6.782
	0.508	10.480	10.700	10.700
	0.559	12.748	13.017	13.017
	0.635	16.576	16.929	16.929
1	0.0254	0.024	0.028	0.028
	0.127	0.613	0.707	0.707

Continued on next page

Table 4.11 – Continued from previous page

Axial depth-of-cut (mm)	Feed (mm/tooth)	Minimum (μm)	Maximum (μm)	Mean (μm)
1	0.203	1.568	1.810	1.810
	0.305	3.554	4.103	4.103
	0.406	6.332	7.317	7.317
	0.508	9.985	11.552	11.552
	0.559	12.142	14.058	14.058
	0.635	15.783	18.296	18.296
5	0.0254	2.08	3.27	3.27
	0.127	58.53	101.48	101.48
	0.203	219.97	336.32	336.32
	0.305	425.22	536.01	536.01
	0.406	567.43	691.27	691.27
	0.508	690.89	835.18	835.18
	0.559	749.24	905.25	905.25
	0.635	834.04	1008.66	1008.66

In Table 4.11, the minimum and maximum predictions of surface roughness are listed.

The mathematical surface roughness method computed a high surface roughness along

with an increase in axial depth-of-cut by considering tool vibrations generated by cutting forces. However, the mathematical prediction method is not suitable for estimating the surface roughness when a square insert uses in the milling experiment.

Geometrical surface roughness prediction for square insert

The results listed in Table 4.12 were computed by the geometrical surface roughness Eq.(2.49). The geometrical surface roughness values were considered the effect of the feed and tool geometry.

Table 4.12: Surface roughness estimation by geometrical surface roughness Eq (2.49).

Axial depth-of-cut (mm)	Feed (mm/tooth)	Minimum (μm)	Maximum (μm)	Mean (μm)
0.15	0.0254	0.048	0.049	0.048
	0.127	0.109	0.110	0.109
	0.203	0.134	0.136	0.135
	0.305	0.136	0.138	0.137
	0.406	0.183	0.184	0.183
	0.508	0.229	0.232	0.231
	0.559	0.253	0.256	0.254
	0.635	0.288	0.291	0.289
1	0.0254	0.047	0.051	0.049
	0.127	0.106	0.114	0.110
	0.203	0.131	0.141	0.136

Continued on next page

Table 4.12 – Continued from previous page

Axial depth-of-cut (mm)	Feed (mm/tooth)	Minimum (μm)	Maximum (μm)	Mean (μm)
1	0.305	0.133	0.143	0.138
	0.406	0.178	0.192	0.185
	0.508	0.224	0.241	0.232
	0.559	0.247	0.265	0.256
	0.635	0.281	0.302	0.292
5	0.0254	0.659	0.727	0.693
	0.127	1.092	1.323	1.207
	0.203	1.301	1.593	1.447
	0.305	1.287	1.588	1.437
	0.406	1.713	2.118	1.915
	0.508	2.144	2.653	2.399
	0.559	2.359	2.921	2.640
	0.635	2.680	3.321	3.000

As shown in Table 4.12, a range of surface roughness was predicted by incorporating the effect of tool displacement along the x and z directions. It shows that the geometrical prediction can estimate surface finish at various axial depth-of-cuts. In

the same way, the variation between the minimum and maximum values increased with increasing axial depth-of-cut.

Table 4.13: Surface roughness prediction comparison of geometrical surface roughness with the experimental result.

Axial depth of cut (mm)	Feed (mm/tooth)	Experimental result		Surface finish prediction	
		Minimum (μm)	Maximum (μm)	Minimum (μm)	Maximum (μm)
0.15	0.0254	0.051	0.078	0.048	0.049
	0.127	0.100	0.182	0.109	0.110
	0.203	0.086	0.243	0.134	0.136
	0.305	0.116	0.246	0.136	0.138
	0.406	0.130	0.290	0.183	0.184
	0.508	0.130	0.282	0.229	0.232
	0.559	0.163	0.350	0.253	0.256
	0.635	0.165	0.389	0.288	0.291
1	0.0254	0.049	0.196	0.047	0.051
	0.127	0.074	0.220	0.106	0.114
	0.203	0.071	0.224	0.131	0.141
	0.305	0.099	0.373	0.133	0.143

Continued on next page

Table 4.13 – Continued from previous page

Axial depth of cut (mm)	Feed (mm/tooth)	Experimental result		Surface finish prediction	
		Minimum (μm)	Maximum (μm)	Minimum (μm)	Maximum (μm)
1	0.406	0.094	0.269	0.178	0.192
	0.508	0.122	0.419	0.224	0.241
	0.559	0.147	0.442	0.247	0.265
	0.635	0.173	0.399	0.281	0.302
5	0.0254	0.064	0.189	0.659	0.727
	0.127	0.084	0.204	1.092	1.323
	0.203	0.107	0.337	1.301	1.593
	0.305	0.169	0.536	1.287	1.588
	0.406	0.118	0.461	1.713	2.118
	0.508	0.259	1.372	2.144	2.653
	0.559	0.318	1.929	2.359	2.921
	0.635	0.441	3.531	2.680	3.321

Table 4.13 compares the minimum and maximum values of the experimental results with the surface roughness predictions.

Table 4.14: Average surface roughness comparison of geometrical surface roughness with the experimental result.

Axial depth of cut (mm)	Feed (mm/tooth)	Experimental average (μm)	Geometrical prediction (μm)
0.15	0.0254	0.0613	0.048
	0.127	0.129	0.109
	0.203	0.153	0.135
	0.305	0.1655	0.137
	0.406	0.210	0.183
	0.508	0.225	0.231
	0.559	0.248	0.254
	0.635	0.244	0.289
1	0.0254	0.073	0.049
	0.127	0.116	0.110
	0.203	0.143	0.136
	0.305	0.161	0.138
	0.406	0.206	0.185
	0.508	0.242	0.232
	0.559	0.262	0.256

Continued on next page

Table 4.14 – Continued from previous page

1	0.635	0.285	0.292
	0.0254	0.089	0.693
	0.127	0.140	1.207
	0.203	0.210	1.447
	0.305	0.324	1.437
5	0.406	0.258	1.915
	0.508	0.864	2.399
	0.559	1.137	2.640
	0.635	1.43	3.000

The comparison between the experimental and geometrical surface finish comparison showed good correlation when axial depth-of-cuts were 0.15 mm and 1 mm. Although there were variations in the geometrical prediction compared to the experiment when the axial depth-of-cut was 5 mm, it was still better than the mathematical and theoretical surface roughness prediction methods. This is because the theoretical and mathematical surface roughness methods do not consider the wiper edge in a tool insert.

Chapter 5

Conclusions

From the machining simulation by using the numerical method, the following can be concluded:

1. Our proposed model can be used to estimate the cutting forces, vibrations, and tool trajectory in the milling process based on actual cutting parameters.
2. A higher axial depth of cut or feed will lead to generating a higher magnitude of vibrations, and that results in producing a rough surface quality.
3. During the milling simulation, it is observed that an increased cutting force results in an increased magnitude of vibration, and poor surface roughness will be obtained.
4. The presented prediction model for geometrical surface roughness shows a better correlation with experimental results than the theoretical surface roughness prediction model.
5. While the geometrical surface roughness model is only a function of tool nose radius and feed per tooth, the presented surface roughness model takes into account the impact of various machining parameters, including axial depth-of-cut, feed rate,

tool and workpiece properties, resulting in more accurate predictability.

6. This study will aid industries in predicting cutting forces, tool vibrations, and surface roughness at various axial depth-of-cuts by taking into account the magnitude of vibrations.

7. This model can also be used to optimize cutting force, minimize tool vibration, and obtain the desired surface roughness by aiding in the selection of machining parameters, such as spindle speed, feed per tooth, tool specs, etc.

Bibliography

- B. Barber G. Gu J. Schall J. D Wang, R. Wang. Models for prediction of surface roughness in a face milling process using triangular inserts. *Lubricants*, pages 1(1), 9, 2019.
- N. M Newmark. A method of computation for structural dynamics. *Journal of the Engineering Mechanics Division*, pages 85(3), 67–94, 1959.
- G. Bayly PV. Mann BP Insperger, T. Stepan. Multiple chatter frequencies in milling process. *Chin J Aeronaut*, pages 29(6), 1852–1858, 2016.
- Shi Z. Y. Liu, L. N. and Z. Q Liu. Finite element modal analysis for face-milling cutter. *Key Engineering Materials*, 589-590:19–22, 2013.
- T. Ng E. Elbestawi M. A Omar, O. E. E. K. El-Wardany. An improved cutting force and surface topography prediction model in end milling. *International Journal of Machine Tools and Manufacture*, pages 47(7–8), 1263–1275, 2007.
- K. S Schmitz, T. Smith. Machining dynamics: frequency response to improved productivity. *Springer*, page Whole book, 2019.

- MY Tsai, SY Chang, JP Hung, and CC Wang. Investigation of milling cutting forces and cutting coefficient for aluminum 6060-t6. *Computers & Electrical Engineering*, 51:320–330, 2016.
- Machining Data Handbook. Machining data handbook. *Machinability Data Center*, 3rd Edition:Whole book, 1980.
- Vosniakos G-C Benardos, PG. Predicting surface roughness in machining: a review. *International journal of machine tools and manufacture*, 43:833–844, 2003.
- J Raja, B Muralikrishnan, and Shengyu Fu. Recent advances in separation of roughness, waviness and form. *Precision Engineering*, 26:222–235, 2002.
- Jie Gu, Gary C Barber, Qinyu Jiang, and Simon Tung. Surface roughness model for worn inserts of face milling: Part i—factors that affect arithmetic surface roughness. *Tribology transactions*, 44(1):47–52, 2001.
- Urmaze Naterwalla. Machining solutions. *Wordzworth*, page Whole book, 2020.
- Patricia Munoz-Escalona and Paul G Maropoulos. A geometrical model for surface roughness prediction when face milling al 7075-t7351 with square insert tools. *Journal of Manufacturing Systems*, 36:216–223, 2015.
- A. J Qu, J. Shih. Analytical surface roughness parameters of a mathematical profile consisting of elliptical arcs. *Machining Science and Technology*, pages 7(2), 281–294, 2003.

- Y Altintas. Manufacturing automation: Metal cutting mechanics, machine tool vibrations, and cnc design. *Cambridge University Press*, page Whole book, 2012.
- Thomas J Drozda and Charles Wick. Tool and manufacturing engineers handbook, vol. 1. *Society of Manufacturing Engineers, Dearborn, MI*.
- K Kadrigama, MM Noor, MRM Rejab, MM Rahman, MSM Sani, and TT Mon. The effect of end milling parameters on surface roughness when machining corrosion resistance alloy. *In International Conference on Advance Mechanical Engineering (ICAME09)*, pages 22–25, 2009.
- Ataollah Javidi, Ulfried Rieger, and Wilfried Eichlseder. The effect of machining on the surface integrity and fatigue life. *International Journal of fatigue*, 30:2050–2055, 2008.
- Mohammed T Hayajneh, Montasser S Tahat, and Joachim Bluhm. A study of the effects of machining parameters on the surface roughness in the end-milling process. *Jordan Journal of Mechanical and Industrial Engineering*, 1:1, 2007.
- Sukhdev S Bhogal, Charanjeet Sindhu, Sukhdeep S Dhani, and BS Pabla. Minimization of surface roughness and tool vibration in cnc milling operation. *Journal of Optimization*, 2015, 2015.
- R. Dauksevicius R. Mikuckyte S Ostasevicius, V. Gaidys. Study of vibration milling

- for improving surface finish of difficult-to-cut materials. *Journal of Mechanical Engineering*, pages 57(06), 351–357, 2019.
- ES Gadelmawla, Monir M Koura, Talal MA Maksoud, Ibrahiem M Elewa, and HH Soliman. Roughness parameters. *Journal of materials processing Technology*, 123(1):133–145, 2002.
- RS Hahn. Metal-cutting chatter and its elimination. *Trans ASME J Eng Indus Ser B*, 74:1073–1080, 1952.
- Huamin Zhou. Dequn Li. Hongqi Liu. Haiyu Qiao. Xiaoqiang Wang Yang Fu., Yun Zhang. Timely online chatter detection in end milling process. *Mechanical Systems and Signal Processing*, 75:668–688, 2016.
- P. Pelic M. Maruda R. W. Barrans S. Krolczyk G. M Wojciechowski, S. Twardowski. Precision surface characterization for finish cylindrical milling with dynamic tool displacements model. *Precision Engineering*, pages 141, 30–35, 2019.
- M. Bachrathy D. Stepan G Denkena, B. Krüger. Model based reconstruction of milled surface topography from measured cutting forces. *International Journal of Machine Tools and Manufacture*, pages 141, 30–35, 2012.
- F. J. Fernández J. López de Lacalle L. N. Gil A. Bilbao E. Veiga F. Lamikiz A Arizmendi, M. Campa. Model for surface topography prediction in peripheral milling considering tool vibration. *CIRP Annals*, pages 58(1), 93–96, 2009.

- K. E Liu, K. J. Rouch. Optimal passive vibration control of cutting process stability in milling. *Journal of Materials Processing Technology*, pages 28(1–2), 285–294, 1991.
- T. Arnaud L. Dessein G. Peigné G Seguy, S. Insperger. On the stability of high-speed milling with spindle speed variation. *The International Journal of Advanced Manufacturing Technology*, pages 48(9–12), 883–895, 1991.
- H. N. Verlinden O Rivière-Lorphèvre, E. Huynh. Influence of the time step selection on dynamic simulation of milling operation. *The International Journal of Advanced Manufacturing Technology*, pages 95(9–12), 4497–4512, 2019.
- H. Jia Z. Feng Y. Liang S. Y Lu, X. Zhang. Floor surface roughness model considering tool vibration in the process of micro-milling. *The International Journal of Advanced Manufacturing Technology*, pages 94(9–12), 4415–4425, 2017.
- X. Meng G Jiang, H. Long. Study of the correlation between surface generation and cutting vibrations in peripheral milling. *Journal of Materials Processing Technology*, pages 208(1–3), 229–238, 2008.
- P Kalidass, S. Palanisamy. Effect of machining parameters on surface roughness in end milling of aisi 304 steel using uncoated solid carbide tools. *Australian Journal of Mechanical Engineering*, pages 12(2), 223–232, 2014.

- M. Faura F Franco, P. Estrems. Influence of radial and axial runouts on surface roughness in face milling with round insert cutting tools. *International Journal of Machine Tools and Manufacture*, pages 44(15), 1555–1565, 2004a.
- M. Faura F Franco, P. Estrems. Influence of radial and axial runouts on surface roughness in face milling with round insert cutting tools. *International Journal of Machine Tools and Manufacture*, pages 44(15), 1555–1565, 2004b.
- B. Kundrák J Felhő, C. Karpuschewski. Surface roughness modelling in face milling. *Procedia CIRP*, pages 31, 136–141, 2015.
- A. Wojciechowski S. Mia M. Magri A. Suyama D.I. Bustillo A. Krolczyk G. Gupta M.K Pimenov, D.Y. Hassui. Effect of the relative position of the face milling tool towards the workpiece on machined surface roughness and milling dynamics. *Appl. Sci*, pages 9, 842, 2019.
- M.; He N. Gupta M.K. Pimenov D.Y Lyu, Y. Jamil. Development and testing of a high-frequency dynamometer for high-speed milling process. *Machines*, pages 9, 11, 2021.
- K. V. Murthy P. B. G. S. N Vara Prasad, V. U. Rao. Mechanistic models for prediction of cutting forces and power consumption considering chip geometry. *Mechanistic models for prediction of cutting forces and power consumption considering chip geometry*, pages 235(2), 479–488, 2020.

- M. E. Sarhan A. A. El-Zahry R. M Maher, I. Eltaib. Cutting force-based adaptive neuro-fuzzy approach for accurate surface roughness prediction in end milling operation for intelligent machining. *The International Journal of Advanced Manufacturing Technology*, pages 76(5–8), 1459–1467, 2014.
- K. F Kim, H. S. Ehmman. A cutting force model for face milling operations. *International Journal of Machine Tools and Manufacture*, pages 33(5), 6651–673, 1993.
- Z. L. Niu J. B. Zhu L. M Chen, Z. Z. Li. Chatter detection in milling processes using frequency-domain rényi entropy. *The International Journal of Advanced Manufacturing Technology*, pages 106(3–4), 877–890, 2019.
- J. Kalveram M. Ste'pa'n G. Weinert K. Govekar E Insperger, T. Gradisek. Machine tool chatter and surface quality in milling processes. *Manufacturing Engineering and Materials Handling Engineering*, page Whole book, 2004.
- Srinivas J. Shaik, J. H. Analytical prediction of chatter stability of end milling process using three-dimensional cutting force model. *ournal of the Brazilian Society of Mechanical Sciences and Engineering*, 39(5):1633–1646, 2016a.
- Z. J. Chen C. Song Y. X. Zhang J. J. Du D. W Li, Y. Yang. An integral algorithm for instantaneous uncut chip thickness measuring in the milling process. *Advances in Production Engineering and Management*, pages 13(3), 297–306, 2018.

- Haibin Yu, Minli Zheng, Wei Zhang, Wenrui Lv, and Wanying Nie. Research on centroid distribution and dynamic characteristics of irregular tooth end milling cutters. *Applied Sciences*, 9(14):2775, 2019.
- Rao and Griffin. Mechanical vibrations. *6th ed.; Publisher: Pearson, USA*, page whole book, 2018.
- M. K. Huang, W. Jawed. Newmark-beta method in discrete elastic rods algorithm to avoid energy dissipation. *Journal of Applied Mechanics*, pages 86(8),, 2019.
- P Bo. Applying the newmark method to the discontinuous deformation analysis. *Virginia Tech*, Thesis, 2014.
- D. J Michel, Geradin . Rixen. Mechanical vibrations: theory and application to structural dynamics. *John Wiley*, page Whole book, 2015.
- N. Scippa A. Campatelli G Sallese, L. Grossi. Numerical investigation of chatter suppression in milling using active fixtures in open-loop control. *Journal of Vibration and Control*, pages 24(9), 1757–1773, 2016.
- Ozel T. Zeren E. Finite element method simulation of machining of aisi 1045 steel with a round edge cutting tool. *Proceedings of 8th CIRP international workshop on modeling of machining operations*, pages , 533–541, 2015.

- Movahheddy M. Simulation of the orthogonal metal cutting process using an arbitrary lagrangian-eulerian finite element method. *J Mat Proc Tech*, pages 103, 267–275, 2000.
- M. Lacomme JL Limido, J. Espinosa C. Salañun. Sph method applied to high speed cutting modelling. *Int J Mech Sci*, pages 49(7), 898–908, 2007.
- M. Dinghua Z Ming, L. Jiawei. Time-domain modeling of a cutter exiting a workpiece in the slot milling process. *Chin J Aeronaut*, pages 29(6), 1852–1858, 2016.
- G Peigne. A model of milled surface generation for time domain simulation of high-speed cutting. *Proc Inst Mech Eng Part B J Eng Manuf*, pages 217(7), 919–930, 2003.
- J Smith, S. Tlusty. Efficient simulation programs for chatter in milling. *CIRP Ann Manuf Technol*, pages 42, 463–466, 1993.
- P Avitabile. Modal testing: A practitioner's guide. *1st ed.; Publisher: Wiley, USA*,, pages 6–89, 2018.
- Y Montgomery, D. Altintas. Mechanism of cutting force and surface generation in dynamic milling. *Journal of Engineering for Industry*, pages 113(2), 160–168, 1991.
- Srinivas J. Shaik, J. H. Analytical prediction of chatter stability of end milling process using three-dimensional cutting force model. *Journal of the Brazilian Society of Mechanical Sciences and Engineering*, 39(5):1633–1646, 2016b.

Srinivas J. Shaik, J. H. Optimal design of spindle-tool system for improving the dynamic stability in end-milling process. *Indian Academy of Sciences*, 45(1):45–55, 2020.

Appendix A Chatter tendency according to workpiece materials

Table A.1: Appendix Chatter tendency for common work materials ([Handbook, 1980])

Material group	Hardness (Bhn or R_c)	Chatter tendency (Q)
Free machining carbon steels, wrought	100-150	0.9
	150-200	1.0
	200-275	1.2
	275-325	1.4
	325-375	1.6
	375-425	1.8
Carbon steels, wrought and cast	85-125	0.8
	125-175	0.8
	175-225	1.0
	225-275	1.2

Continued on next page

Table A.1 – Continued from previous page

Material group	Hardness (Bhn or R_c)	Chatter tendency (Q)
Carbon steels, wrought and cast	275-325	1.4
	325-375	1.6
Free machining alloy steels, wrought	150-200	1.1
	200-275	1.4
	275-325	1.6
	325-375	1.8
	375-425	2.0
	45-48 R_c	2.2
Nitriding steels, wrought	48-52 R_c	2.5
	200-250	1.4
	300-350	1.8
	200-250	1.6
Armor plate	250-300	1.8
	300-350	2.0
	350-400	2.3
	400-450	2.6

Continued on next page

Table A.1 – Continued from previous page

Material group	Hardness (Bhn or R_c)	Chatter tendency (Q)
Structural steels, wrought	100-150	1.0
	150-200	1.2
	200-250	1.4
	300-350	1.6
	350-400	1.8
	400-450	2.0
Free machining stainless steels (austenitic), wrought	135-185	1.5
	185-225	1.7
	225-275	1.9
	275-325	2.1
	325-375	2.3
Free machining stainless steels (ferritic and martensitic), wrought	135-185	1.5
	185-225	1.7
	225-275	1.9
	275-325	2.3
	325-375	2.7

Continued on next page

Table A.1 – Continued from previous page

Material group	Hardness (Bhn or R_c)	Chatter tendency (Q)
	135-185	1.8
	185-225	1.9
Stainless steels (austenitic), wrought and cast	225-275	2.1
	275-325	2.3
	325-375	2.6
	135-185	1.8
	185-225	1.9
	225-275	2.1
Stainless steels	275-325	2.3
(ferritic and martensitic), wrought and cast	325-375	2.6
	375-425	2.9
	42-45 R_c	3.2
	45-48 R_c	3.4
	48-52 R_c	4.0
Precipitation hardening stainless steels	150-200	2.4
wrought and cast	275-325	2.7

Continued on next page

Table A.1 – Continued from previous page

Material group	Hardness (Bhn or R_c)	Chatter tendency (Q)
Precipitation hardening stainless steels	325-375	3.0
wrought and cast	375-440	3.4
Gray cast iron	120-150	0.6
	150-200	0.8
	200-220	1.0
	220-260	1.2
Ductile cast iron	140-190	0.9
	190-225	1.1
	225-260	1.3
	260-300	1.5
Malleable cast iron	110-160	0.9
	160-200	1.1
	200-240	1.3
	240-280	1.5
	280-320	1.7
Aluminum alloys, wrought and cast	30-80	0.5

Continued on next page

Table A.1 – Continued from previous page

Material group	Hardness (Bhn or R_c)	Chatter tendency (Q)
Aluminum alloys, wrought and cast	80-125	0.6
Magnesium alloys, wrought and cast	50-90	0.4
Titanium alloys, wrought and cast	150-200	1.2
	200-250	1.4
	250-300	1.6
	300-350	1.8
	350-400	2.0
	400-450	2.2
Copper alloys, wrought	10-60 R_c	0.6-0.9
	60-100 R_c	1.0-1.2
Copper alloys, cast	40-100	0.6-0.8
	100-200	0.8-1.6
Nickel alloys, wrought and cast	80-150	1.5
	150-200	2.2
	200-250	2.8
	300-320	3.5

Continued on next page

Table A.1 – Continued from previous page

Material group	Hardness (Bhn or R_c)	Chatter tendency (Q)
High temperature alloys	200-300	2.0-3.0
	300-375	2.0-5.0
	375-425	3.0-6.0
Refractory alloys, wrought, cast, and P/ M	175-250	2.0-6.0
	250-300	3.0-7.0
	300-350	4.0-7.0
Zinc alloys, cast	80-100	0.5
Lead alloys and Tin alloys	5-30	0.3

Appendix B CNC milling operation G-code

O0000

G21

G0 G17 G40 G49 G80 G90

N10

T30 M6 (100 F/C)

(Z MAX : Z50.)

(Z MIN : Z-1.)

(XY LEAVE : 0. // Z LEAVE : 0.)

G0 G90 G54 X60. Y0. S300 M3

G43 H30 Z50. M8 T24

Z2.

G1 Z-1. F300.

X0. F7.6

X-100.

X-160.

G0 Z50.

M9

M5

G91 G28 Z0.

M01

N20

T24 M6 (6 CHA)

(Z MAX : Z50.)

(Z MIN : Z-2.3)

(XY LEAVE : 0. // Z LEAVE : 0.)

G0 G90 G17 G54 X.6 Y-53.7 S7000 M3

G43 H24 Z50. M8 T30

Z2.

G1 Z-2.3 F2000.

Y-51.6 F1500.

G3 X0. Y-51. I-.6 J0.

G1 X-100.

G2 X-101. Y-50. I0. J1.

G1 Y0.

G2 X-100. Y1. I1. J0.

G1 X0.

G2 X1. Y0. I0. J-1.

G1 Y-50.

G2 X0. Y-51. I-1. J0.

G3 X-.6 Y-51.6 I0. J-.6

G1 Y-53.7

G0 Z50.

M9

M5

G91 G28 Z0.

G28 Y0.

M30

Appendix C Machined surface roughness

Table C.1: Experiment surface roughness results (R_a) at axial depth-of-cut of 0.15 mm.

Feed (mm/tooth)	Measurement (μm)					κ (degree)
0.0254	0.074	0.059	0.054	0.059	0.051	0.166
	0.064	0.057	0.062	0.071	0.058	
	0.061	0.078	0.061	0.066	0.054	
	0.059	0.069	0.060	0.064	0.060	
	0.054	0.054	0.074	0.054	0.058	
	0.062	0.058				
0.127	0.142	0.123	0.130	0.110	0.134	0.055
	0.180	0.115	0.169	0.124	0.127	
	0.150	0.138	0.133	0.117	0.111	
	0.117	0.100	0.182	0.107	0.114	

Continued on next page

Table C.1 – Continued from previous page

Feed (mm/tooth)	Measurement (μm)					κ (degree)
0.127	0.115	0.137	0.134	0.127	0.122	0.055
	0.103	0.120				
0.203	0.197	0.105	0.130	0.243	0.124	0.041
	0.219	0.130	0.153	0.203	0.146	
	0.227	0.104	0.129	0.227	0.127	
	0.116	0.218	0.086	0.105	0.125	
	0.122	0.201	0.140	0.096	0.114	
	0.126	0.225				
0.305	0.185	0.154	0.123	0.192	0.123	0.027
	0.171	0.172	0.175	0.192	0.246	
	0.197	0.124	0.157	0.195	0.137	
	0.135	0.180	0.183	0.170	0.182	
	0.129	0.186	0.165	0.121	0.116	
	0.176	0.182				
0.406	0.273	0.214	0.193	0.277	0.189	0.027
	0.290	0.214	0.184	0.274	0.227	

Continued on next page

Table C.1 – Continued from previous page

Feed (mm/tooth)	Measurement (μm)					κ (degree)
0.406	0.278	0.206	0.157	0.243	0.195	0.027
	0.130	0.253	0.195	0.167	0.134	
	0.166	0.272	0.210	0.216	0.150	
	0.163	0.196				
0.508	0.267	0.278	0.165	0.266	0.215	0.027
	0.260	0.279	0.183	0.282	0.212	
	0.207	0.275	0.173	0.217	0.277	
	0.154	0.281	0.199	0.201	0.214	
	0.130	0.261	0.219	0.172	0.265	
	0.211	0.220				
0.559	0.350	0.209	0.207	0.345	0.240	0.027
	0.291	0.270	0.191	0.286	0.230	
	0.312	0.220	0.238	0.306	0.213	
	0.204	0.306	0.235	0.211	0.201	
	0.163	0.327	0.182	0.209	0.224	
	0.198	0.320				

Continued on next page

Table C.1 – Continued from previous page

Feed	Measurement					κ
(mm/tooth)	(μm)					(degree)
	0.351	0.211	0.234	0.267	0.252	
	0.297	0.183	0.184	0.339	0.195	
0.635	0.308	0.173	0.165	0.389	0.207	0.027
	0.204	0.304	0.189	0.218	0.269	
	0.245	0.324	0.202	0.214	0.168	
	0.217	0.274				

Table C.2: Experiment surface roughness results (R_a) at axial depth-of-cut of 1 mm.

Feed	Measurement					κ
(mm/tooth)	(μm)					(degree)
	0.065	0.054	0.098	0.060	0.094	
	0.059	0.070	0.196	0.049	0.058	
0.0254	0.059	0.072	0.074	0.118	0.056	0.166
	0.063	0.072	0.050	0.056	0.061	
	0.089	0.062	0.084	0.058	0.062	

Continued on next page

Table C.2 – Continued from previous page

Feed		Measurement				κ
(mm/tooth)		(μm)				(degree)
0.0254	0.07239	0.059				0.166
	0.107	0.186	0.091	0.098	0.142	
	0.105	0.123	0.105	0.105	0.140	
0.127	0.153	0.123	0.082	0.220	0.138	0.055
	0.081	0.115	0.133	0.074	0.092	
	0.101	0.134	0.078	0.090	0.091	
	0.135	0.091				
	0.105	0.156	0.216	0.137	0.106	
	0.210	0.101	0.125	0.197	0.112	
0.203	0.081	0.205	0.091	0.118	0.210	0.041
	0.097	0.140	0.190	0.110	0.080	
	0.210	0.096	0.144	0.210	0.071	
	0.1125	0.224				
	0.373	0.160	0.115	0.177	0.151	
0.305	0.101	0.179	0.184	0.112	0.175	0.027
	0.176	0.164	0.179	0.160	0.105	

Continued on next page

Table C.2 – Continued from previous page

Feed (mm/tooth)	Measurement (μm)					κ (degree)
	0.179	0.170	0.134	0.171	0.160	
0.305	0.099	0.174	0.167	0.103	0.165	0.027
	0.1849	0.125				
	0.268	0.256	0.139	0.264	0.223	
	0.120	0.245	0.227	0.094	0.269	
0.406	0.206	0.138	0.255	0.210	0.164	0.027
	0.269	0.210	0.164	0.247	0.208	
	0.179	0.259	0.231	0.131	0.258	
	0.225	0.109				
	0.214	0.419	0.186	0.259	0.332	
	0.173	0.283	0.350	0.263	0.170	
0.508	0.239	0.271	0.166	0.259	0.161	0.027
	0.260	0.310	0.256	0.202	0.271	
	0.215	0.248	0.280	0.197	0.122	
	0.265	0.174				
0.559	0.393	0.224	0.213	0.310	0.442	0.027

Continued on next page

Table C.2 – Continued from previous page

Feed (mm/tooth)	Measurement (μm)					κ (degree)
	0.182	0.351	0.182	0.224	0.355	
	0.163	0.187	0.327	0.218	0.239	
0.559	0.287	0.184	0.227	0.430	0.176	0.027
	0.242	0.271	0.203	0.147	0.338	
	0.335	0.240				
	0.360	0.367	0.173	0.339	0.221	
	0.399	0.323	0.274	0.209	0.343	
0.635	0.290	0.205	0.314	0.287	0.255	0.027
	0.291	0.291	0.198	0.367	0.247	
	0.179	0.362	0.264	0.234	0.354	
	0.323	0.227				

Table C.3: Experiment surface roughness results (R_a) at axial depth-of-cut of 5 mm.

Feed	Measurement					κ
(mm/tooth)	(μm)					(degree)
	0.101	0.076	0.068	0.083	0.081	
	0.154	0.085	0.080	0.075	0.189	
0.0254	0.071	0.073	0.074	0.084	0.110	0.166
	0.099	0.068	0.152	0.096	0.064	
	0.068	0.095	0.070	0.065	0.092	
	0.064	0.064				
	0.124	0.157	0.084	0.103	0.159	
	0.119	0.117	0.126	0.175	0.137	
0.127	0.182	0.134	0.130	0.204	0.185	0.055
	0.117	0.154	0.184	0.137	0.140	
	0.113	0.140	0.155	0.092	0.141	
	0.144	0.113				
	0.176	0.255	0.227	0.107	0.178	
0.203	0.310	0.153	0.126	0.187	0.199	0.041
	0.227	0.236	0.179	0.242	0.250	
	0.138	0.185	0.203	0.199	0.218	

Continued on next page

Table C.3 – Continued from previous page

Feed	Measurement					κ
(mm/tooth)	(μm)					(degree)
0.203	0.196	0.161	0.283	0.240	0.193	0.041
	0.264	0.337				
0.305	0.404	0.254	0.202	0.400	0.301	0.027
	0.169	0.411	0.364	0.203	0.278	
	0.301	0.345	0.422	0.393	0.217	
	0.536	0.387	0.171	0.479	0.302	
	0.198	0.394	0.415	0.184	0.517	
	0.299	0.204				
0.406	0.226	0.22098	0.187	0.244	0.313	0.027
	0.270	0.344	0.338	0.197	0.250	
	0.235	0.168	0.258	0.243	0.131	
	0.461	0.346	0.168	0.396	0.275	
	0.181	0.299	0.279	0.165	0.334	
	0.319	0.118				
0.508	1.164	0.972	0.506	1.046	1.345	0.027
	0.339	0.933	0.946	0.497	1.354	

Continued on next page

Table C.3 – Continued from previous page

Feed (mm/tooth)	Measurement (μm)					κ (degree)
0.508	1.098	0.339	1.137	1.372	0.259	0.027
	1.013	1.033	0.438	1.334	0.833	
	0.401	1.247	1.290	0.297	0.988	
	0.777	0.383				
0.559	1.671	0.875	1.162	1.650	1.638	0.027
	0.596	1.324	0.989	0.457	1.929	
	0.852	0.477	1.656	1.865	0.592	
	1.583	0.835	0.552	1.787	0.709	
	0.445	1.686	1.428	0.318	1.541	
	1.323	0.755				
0.635	0.851	1.714	2.535	0.472	1.950	0.027
	1.366	0.743	1.159	1.276	0.441	
	2.082	2.390	0.774	3.531	1.230	
	0.765	1.452	1.788	0.786	1.655	
	2.580	0.454	1.656	1.601	0.491	

Continued on next page

Table C.3 – Continued from previous page

Feed		Measurement		κ
(mm/tooth)		(μm)		(degree)
0.635	1.499	1.447		0.027

Appendix D Tooth passing frequency

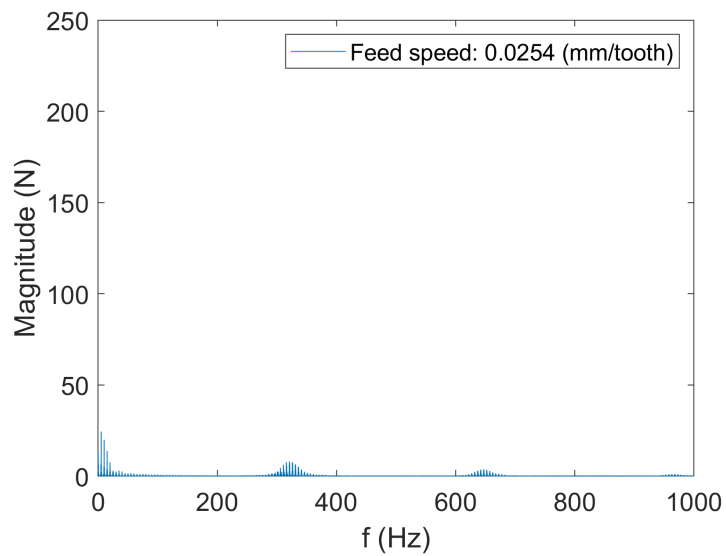


Figure D.1: Tooth passing frequency in the x -direction at feed: 0.0254 (mm/tooth) and axial depth-of-cut: 5 (mm).

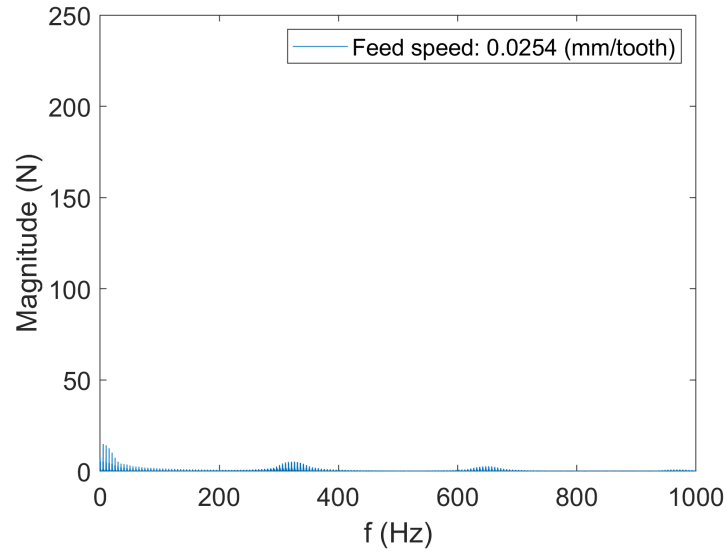


Figure D.2: Tooth passing frequency in the y -direction at feed: 0.0254 (mm/tooth) and axial depth-of-cut: 5 (mm).

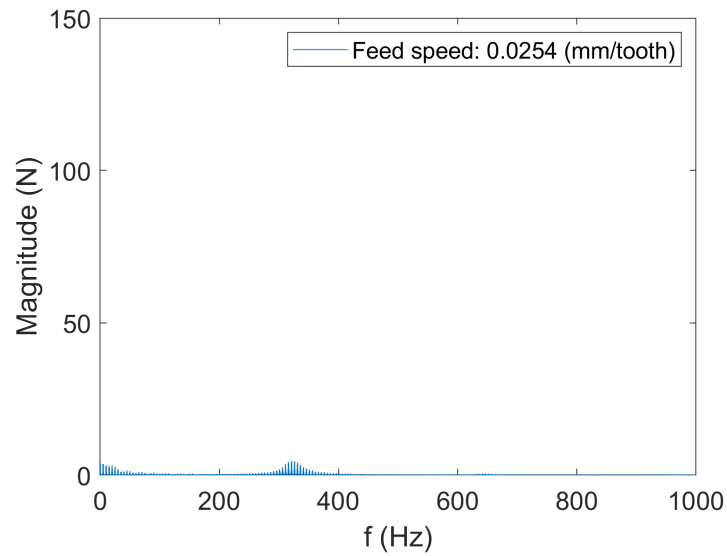


Figure D.3: Tooth passing frequency in the z -direction at feed: 0.0254 (mm/tooth) and axial depth-of-cut: 5 (mm).

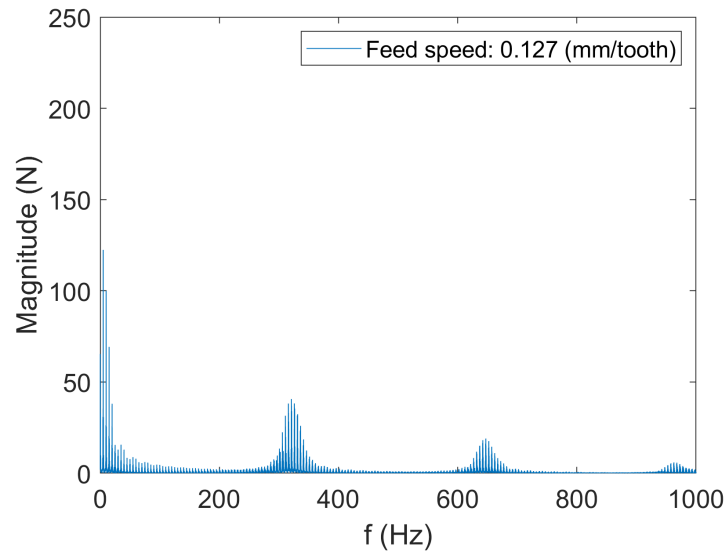


Figure D.4: Tooth passing frequency in the x -direction at feed: 0.127 (mm/tooth) and axial depth-of-cut: 5 (mm).

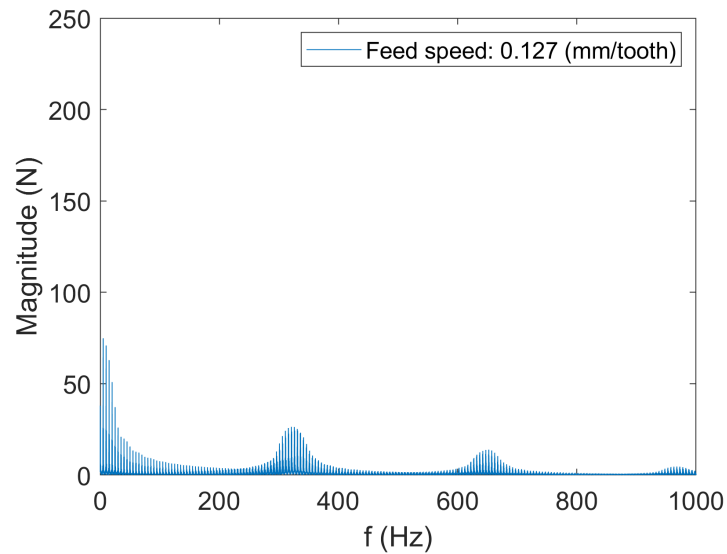


Figure D.5: Tooth passing frequency in the y -direction at feed: 0.127 (mm/tooth) and axial depth-of-cut: 5 (mm).

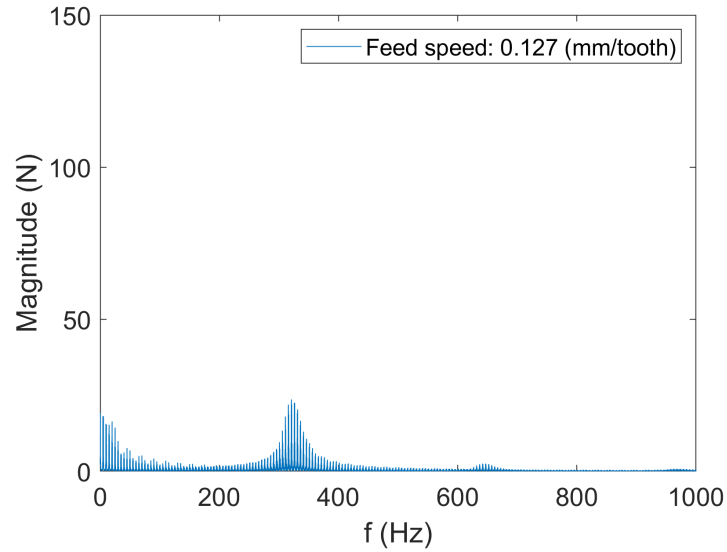


Figure D.6: Tooth passing frequency in the z -direction at feed: 0.127 (mm/tooth) and axial depth-of-cut: 5 (mm).

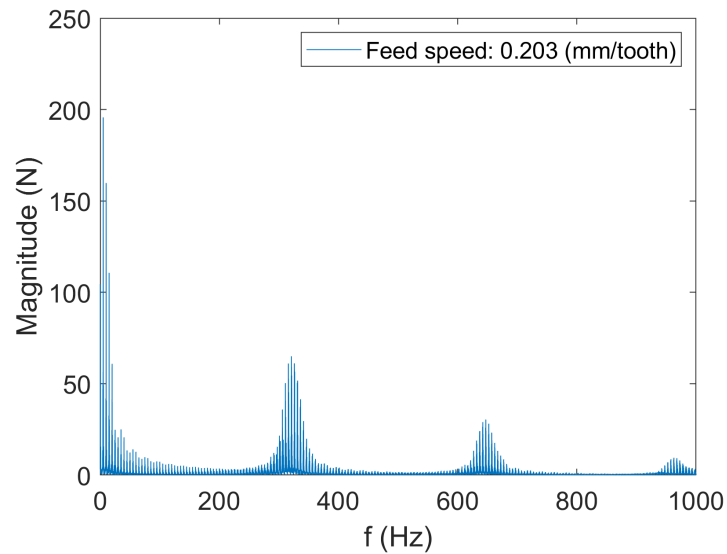


Figure D.7: Tooth passing frequency in the x -direction at feed: 0.203 (mm/tooth) and axial depth-of-cut: 5 (mm).

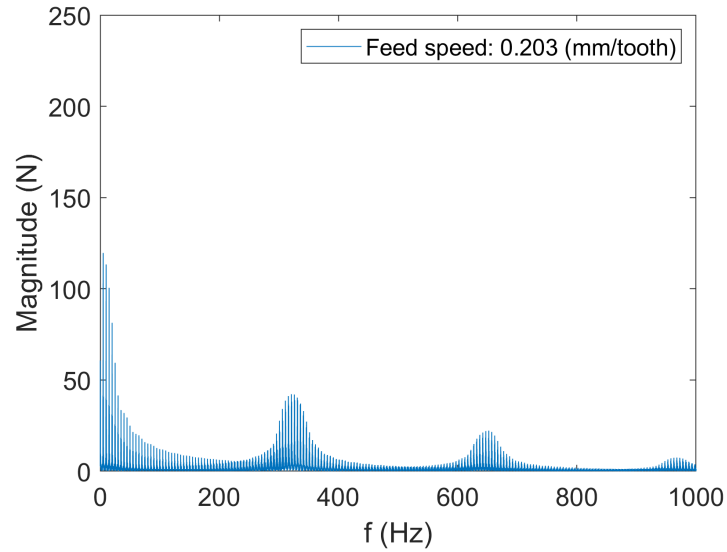


Figure D.8: Tooth passing frequency in the y -direction at feed: 0.203 (mm/tooth) and axial depth-of-cut: 5 (mm).

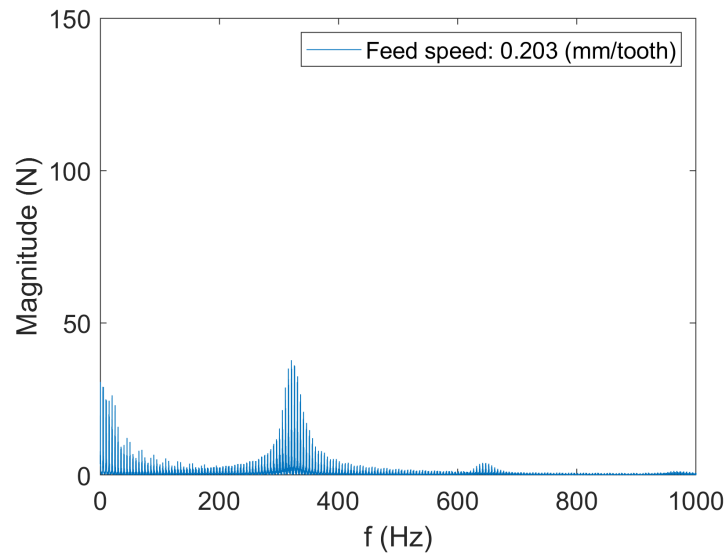


Figure D.9: Tooth passing frequency in the z -direction at feed: 0.203 (mm/tooth) and axial depth-of-cut: 5 (mm).

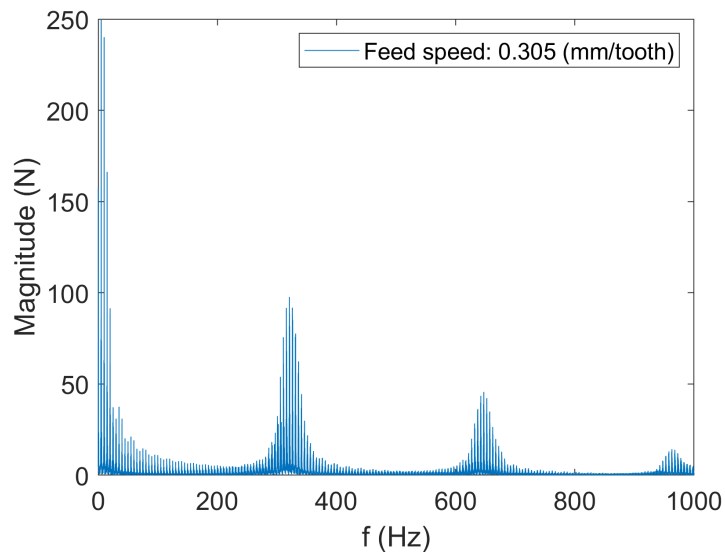


Figure D.10: Tooth passing frequency in the x -direction at feed: 0.305 (mm/tooth) and axial depth-of-cut: 5 (mm).

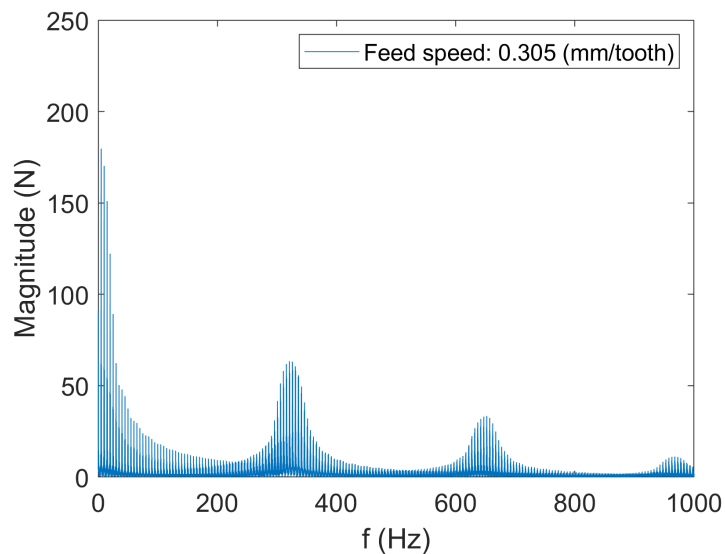


Figure D.11: Tooth passing frequency in the y -direction at feed: 0.305 (mm/tooth) and axial depth-of-cut: 5 (mm).

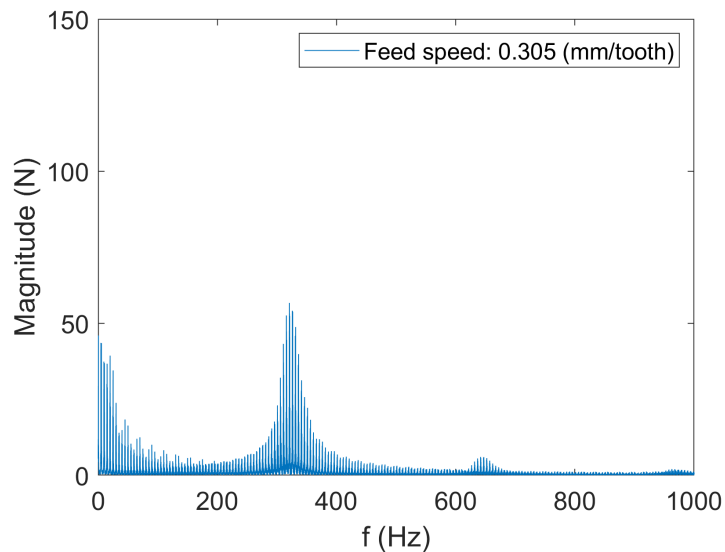


Figure D.12: Tooth passing frequency in the z -direction at feed: 0.305 (mm/tooth) and axial depth-of-cut: 5 (mm).

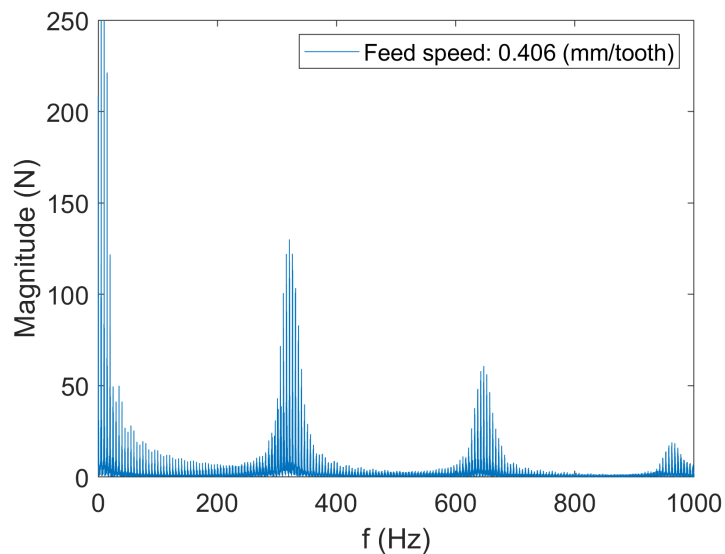


Figure D.13: Tooth passing frequency in the x -direction at feed: 0.406 (mm/tooth) and axial depth-of-cut: 5 (mm).

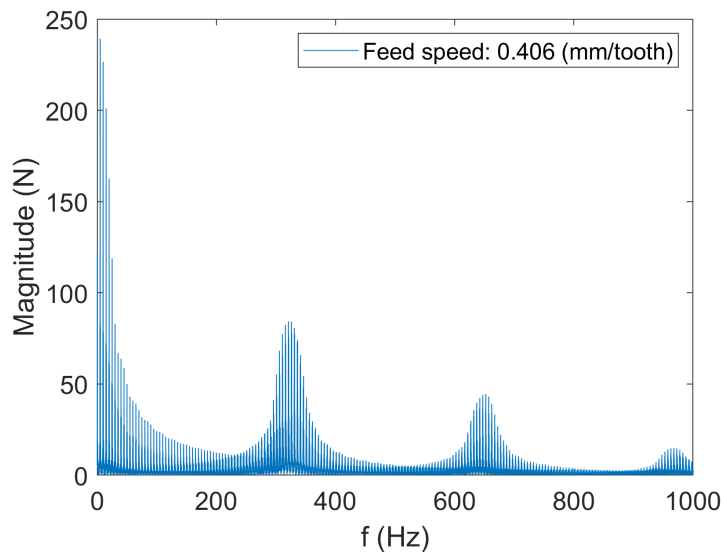


Figure D.14: Tooth passing frequency in the y -direction at feed: 0.406 (mm/tooth) and axial depth-of-cut: 5 (mm).

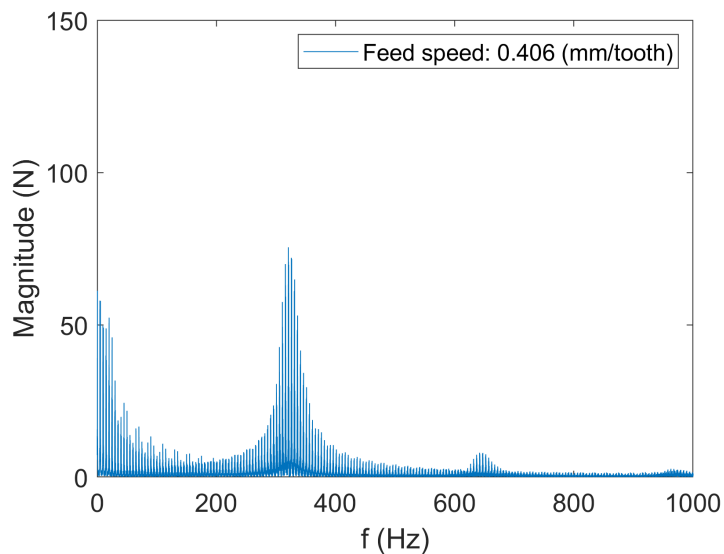


Figure D.15: Tooth passing frequency in the z -direction at feed: 0.406 (mm/tooth) and axial depth-of-cut: 5 (mm).

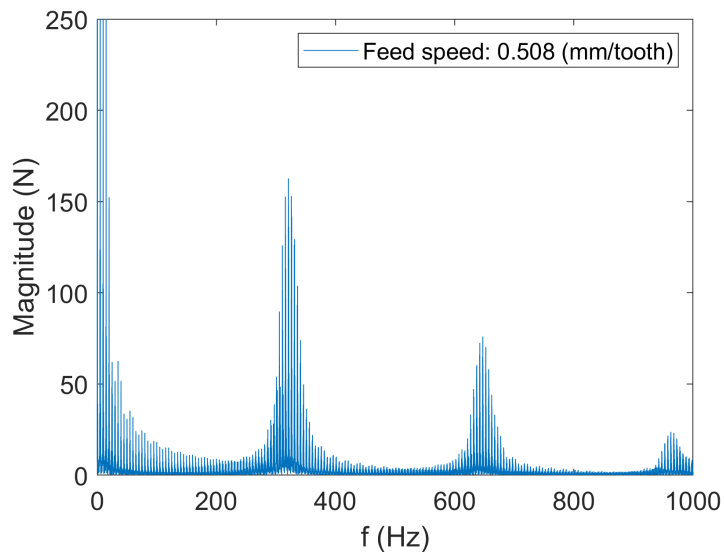


Figure D.16: Tooth passing frequency in the x -direction at feed: 0.508 (mm/tooth) and axial depth-of-cut: 5 (mm).

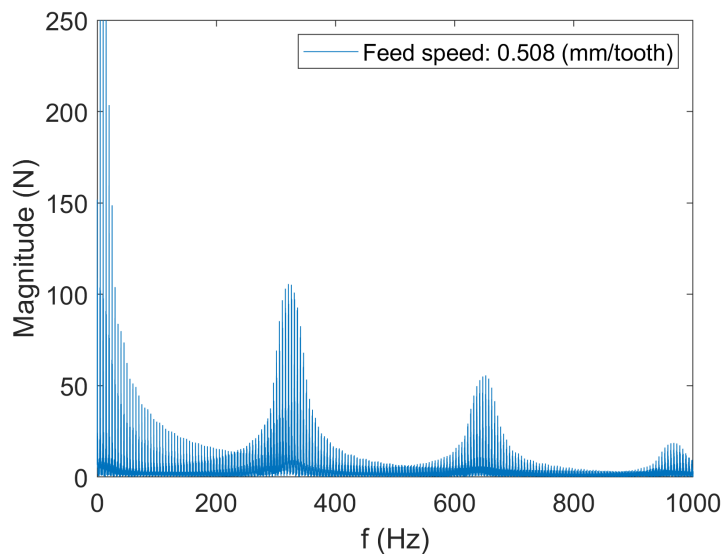


Figure D.17: Tooth passing frequency in the y -direction at feed: 0.508 (mm/tooth) and axial depth-of-cut: 5 (mm).

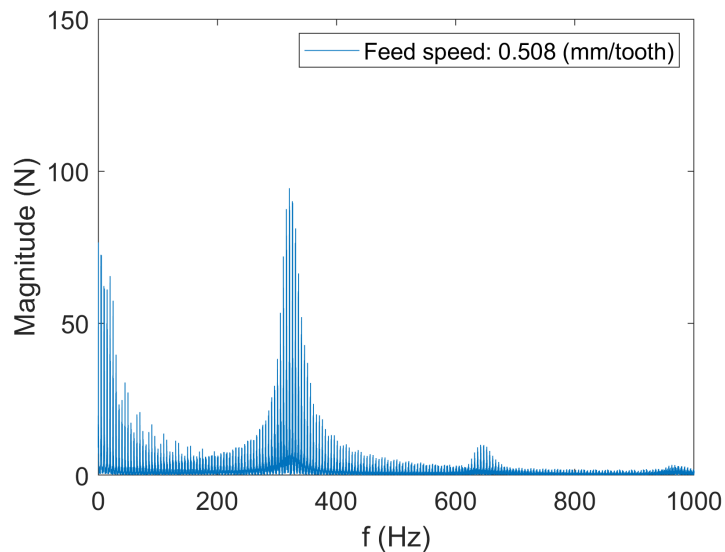


Figure D.18: Tooth passing frequency in the z -direction at feed: 0.508 (mm/tooth) and axial depth-of-cut: 5 (mm).

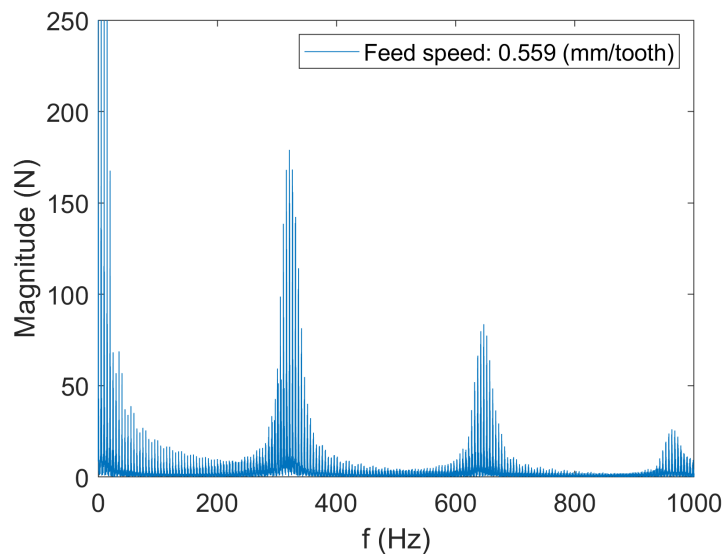


Figure D.19: Tooth passing frequency in the x -direction at feed: 0.559 (mm/tooth) and axial depth-of-cut: 5 (mm).

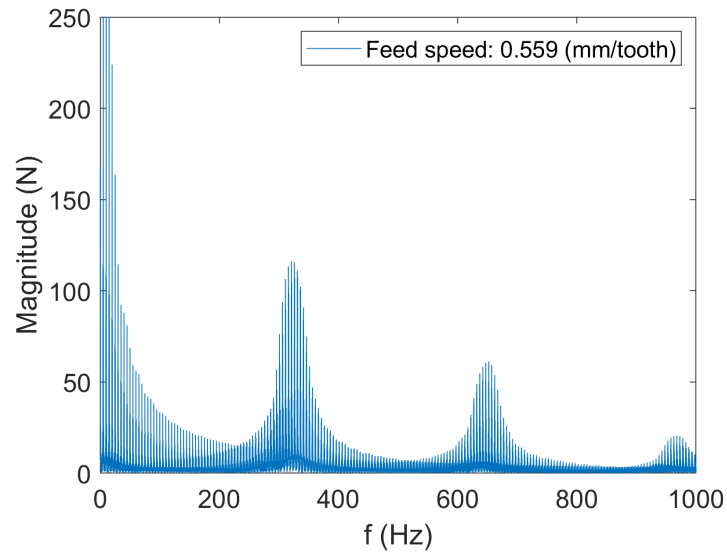


Figure D.20: Tooth passing frequency in the y -direction at feed: 0.559 (mm/tooth) and axial depth-of-cut: 5 (mm).

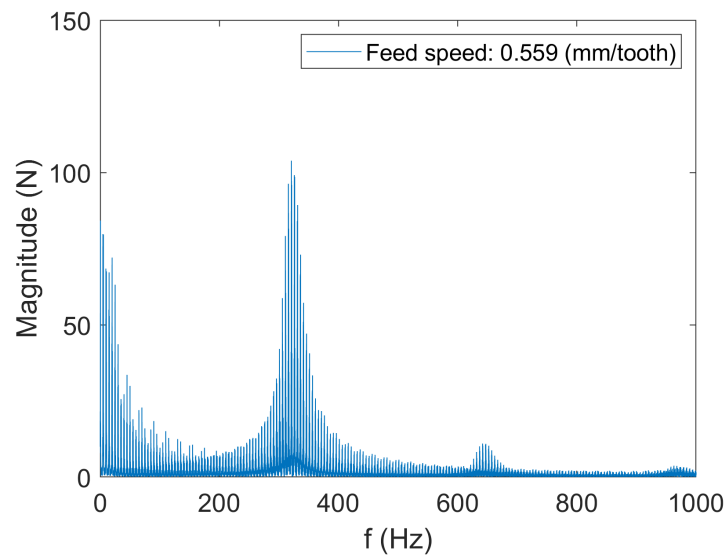


Figure D.21: Tooth passing frequency in the z -direction at feed: 0.559 (mm/tooth) and axial depth-of-cut: 5 (mm).

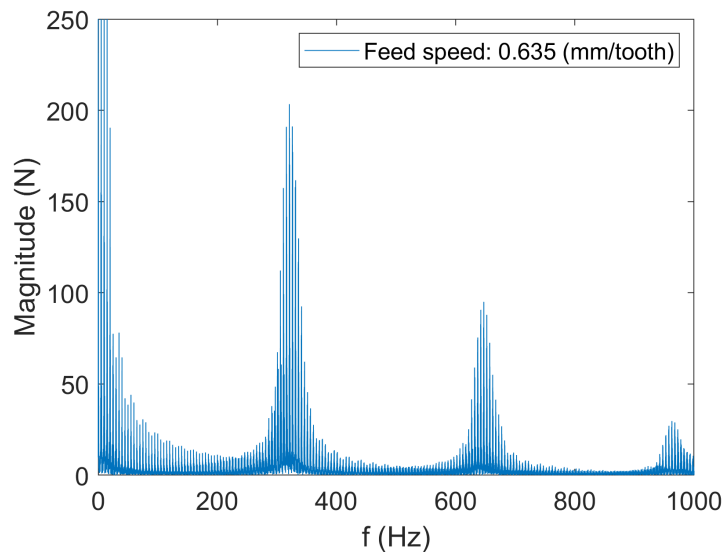


Figure D.22: Tooth passing frequency in the x -direction at feed: 0.635 (mm/tooth) and axial depth-of-cut: 5 (mm).

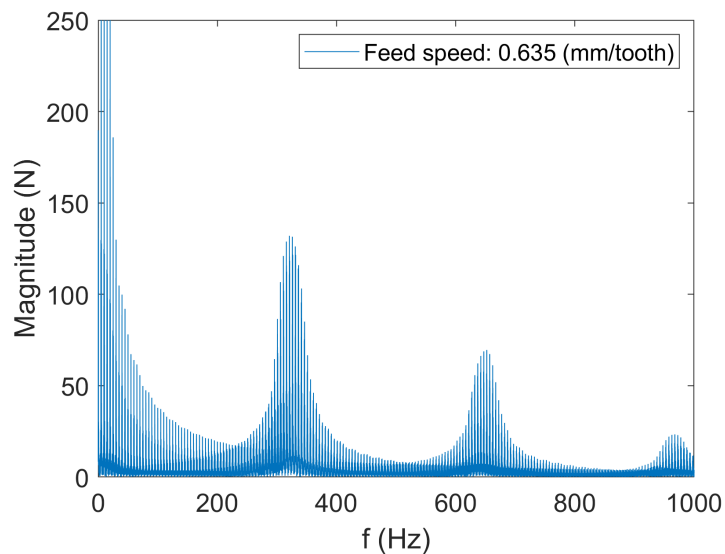


Figure D.23: Tooth passing frequency in the y -direction at feed: 0.635 (mm/tooth) and axial depth-of-cut: 5 (mm).

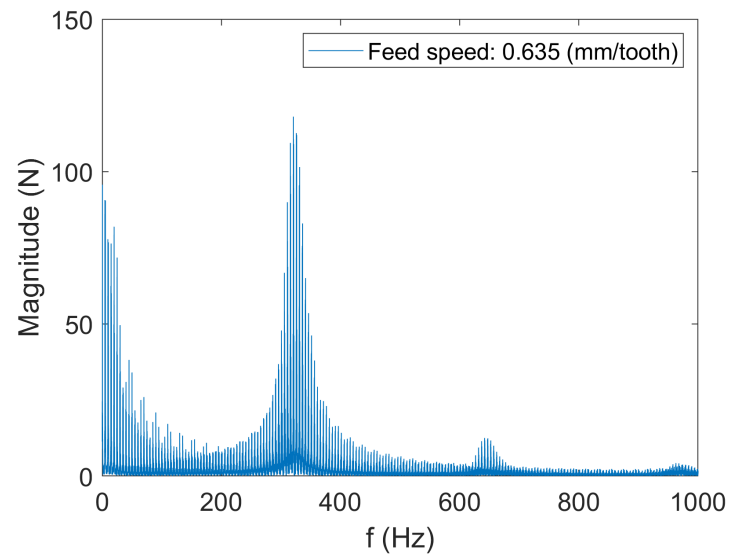


Figure D.24: Tooth passing frequency in the z -direction at feed: 0.635 (mm/tooth) and axial depth-of-cut: 5 (mm).